UNIVERSITY OF CALIFORNIA, MERCED

Role of nanostructured interfaces in photovoltaic and sensing applications

A dissertation submitted in partial satisfaction of the
requirements for the degree Doctor of Philosophy
in Physics

by

Katerina Nikolaidou

Committee in charge:
Professor Michael Scheibner, Chair
Professor Jennifer Lu
Professor Jin Zhang
Professor Sayantani Ghosh

2019

The dissertation of Katerina Nikolaidou is approved, and it is acceptable in quality and form for publication on microfilm and electronically:

_____
Jennifer Lu

_____
Jin Zhang

_____
Sayantani Ghosh

_____
Michael Scheibner, Committee Chair

University of California, Merced
2019

To my parents, who made my education possible through their support and encouragement all these years, and never made me think I should aim for anything less.

To my grandfather, a true feminist who believed in me and my dreams, and was sure I would get a doctorate one day; I wish you were here.

Contents

List of abbreviations

PVSK	Hybrid organic-inorganic Perovskite	NIR	Near infrared
LSCs	Luminescent solar concentrators	LSPR	Localized surface plasmon resonance
NPs	Nanoparticles	CCD	Charge coupled device
MA	Methylammonium	TCSPC	Time-correlated single photon counting
MAI	Methylammonium iodide	SPAD	Single photon avalanche diode
FA	Formamidinium	UV/Vis	Ultraviolet/Visible
PV	Photovoltaic	SEM	Scanning electron microscopy
PPVs	Perovskite photovoltaics	FE-SEM	Field effect SEM
QY	Quantum yield	MO	Magneto-optical
LEDs	Light emitting diodes	MOKE	Magneto-optical Kerr effect
HCP	Hexagonal close packed	LCP	Left circularly polarized
FCC	Face centered cubic	RCP	Right circularly polarized
ETL	Electron transport layer	MPR	Magnetic plasmon resonance
HTL	Hole transport layer	SPPs	Surface plasmon polaritons
PCE	Power conversion efficiency	ITO	Indium tin Oxide
PL	Photoluminescence	FTO	Fluorine-doped tin oxide
P4VP	Poly-4-vinyl-pyridine	FWHM	Full width at half maximum
HMTA	Hexamethylenetetramine	EQE	External quantum efficiency
SC-ZnO	Single crystal ZnO	SA	Self-absorption
MS-ZnO	Microstructured ZnO	NWs	Nanowires
NS-ZnO	Nanostructured ZnO	QDs	Quantum dots
α-Fe_2O_3	Hematite	$CH_3NH_3PbI_3$	Methylammonium lead triiodide
PEM	Photoeleastic modulator	$CH_3NH_3PbI_{3-x}Cl_x$	Mixed halide PVSK
ZnO	Zinc Oxide	PbI_2	Lead iodide
Au	Gold	$PbAc_2$	Lead acetate
Co	Cobalt	$PbCl_2$	Lead chloride
Ag	Silver	Fe	Iron
AgCl	Silver chloride	Fe_3O_4	Magnetite
N_2	Nitrogen	γ-Fe_2O_3	Maghemite

Al	Aluminum	SiO_2	Silicon oxide
ZnS	Zinc sulfide	CdSe	Cadmium selenide
CdTe	Cadmium telluride	Zr	Zirconium
PbS	Lead sulfide	Nb	Niobium
PbSe	Lead selenide	Mg	Magnesium
Cu	Copper	Ni	Nickel
Pt	Platinum	Si	Silicon
Ti	Titanium	Sn	Tin
Al_2O_3	Aluminum oxide	WO_3	Tungsten oxide
Cr	Chromium	AlAs	Aluminum arsenide
O	Oxygen	GaAs	Gallium arsenide
TiO_2	Titanium dioxide		

List of symbols

$\alpha(T)$, $c(T)$	Temperature dependent lattice constants	λ_S	Magnetostrictive constant
E_g	Band gap	$\boldsymbol{M_R}$	Remanence
T	Temperature	μ_0	Permeability of free space
$I(T)$	Luminescence intensity at temperature T	E_L	Amplitude of electric field of left circularly polarized light
I_0	Luminescence intensity at temperature 0 K	E_R	Amplitude of electric field of right circularly polarized light
E_a	Activation energy	E	Total amplitude of incident electric field
V_{oc}	Open circuit voltage	F_a	Attractive force between electron and positive center
E_B	Exciton binding energy	r	Radius of circular orbit of electron
μ	Reduced exciton mass	e	Charge of electron
x	Fraction of free charges	m	Electron mass
$1\text{-}x$	Fraction of excitons	ω	Angular frequency of incident wave
A	Bimolecular recombination coefficient	B	Monomolecular recombination coefficient
N_{tot}	Total charge carrier density	P	Excitation power
n	Total density of excitation	$\boldsymbol{p}$	Electric dipole moment
k_B	Boltzmann's constant	$\boldsymbol{D}$	Displacement field
h	Planck's constant	ε	Dielectric constant
n_{FC}	Density of free charge carriers	ε_0	Permittivity of free space
n_{exc}	Density of excitons	N	Number of dipoles
η_{opt}	Optical efficiency	n, n_L, n_R	Refractive index: total, LCP, and RCP
I_{LSC}	Current generated in PV with LSC	B	Applied magnetic field
I_{PV}	Current generated in PV without LSC	L	Distance light travels through material
A_{PV}	Area of PV cell	$\Delta\theta$	Phase difference of LCP and RCP components
A_{LSC}	Area of LSC	θ	Rotation of polarization direction of resultant wave

T_M	Morin transition temperature	$\boldsymbol{B_0}$	Magnetic induction in vacuum
$\boldsymbol{H}_{K_1}$	Magnetocrystalline anisotropy field	χ	Magnetic susceptibility
K_1	Anisotropy energy constant	$\boldsymbol{k}$	Vacuum wave vector
θ_1, θ_2	Angles of magnetization sub-lattices along the c-axis	$\boldsymbol{Q}$	Voight vector
$\boldsymbol{H}_{A,shape}$	Shape anisotropy field	ξ	Perturbation of refractive index
$\boldsymbol{M}$	Magnetization	ε_r	Relative permittivity
$\boldsymbol{M}_S$	Saturation magnetization	λ	Wavelength of incident light
$\Delta \boldsymbol{N}$	Demagnetization difference between the long and short axis of a nanowire	θ_k	Rotation angle of emerging light
$\boldsymbol{H}_Z$	Field of a nanowire at a distance x	ε_k	Ellipticity of emerging light
l	Distance between two magnetic charges	δ	Krönecker delta
m	Dipole moment	$\boldsymbol{H}$	Magnetizing field
V	Volume	$\boldsymbol{j}$	Current density
σ	External stress	σ	Conductivity tensor
$\boldsymbol{H}_{A,magnetoelastic}$	Magnetoelastic anisotropy field	ε'	Effective permittivity
r_{pp}, r_{ps}, r_{sp}, r_{ss}	Fresnel coefficients of reflected light for s- and p-polarizations	n_e	Free electron density
$E_{r,p}$, $E_{r,s}$	Reflected field p- and s-polarizations	m_e	Electron mass
$E_{i,s}$, $E_{i,p}$	Incident field s- and p-polarizations	ω_{P}	Plasma frequency of a metal
θ_{Kerr}	Kerr rotation	$\mathrm{G}(\omega)$	Net field gain
φ_{Kerr}	Kerr ellipticity	ε_1	Permittivity of surrounding medium
ϕ_{Kerr}	Complex Kerr rotation	r_m	Radius of nanoparticle
$\mathrm{A_{ext}}$	Extinction coefficient	$\mathrm{N_p}$	Number of nanoparticles
$Q_{SPR}(\omega)$	Quality factor for plasmonic nanoparticles	ε_{mo}	Magneto-optical constant
S	Device refractive index sensitivity	$I_{PL}(t)$	PL intensity as a function of time
Γ	SPP full width at half maximum	t	time
T	Transmittance	τ_1, τ_2	Recombination lifetimes

A	Absorbance	τ_{avg}	Average lifetime
I	Intensity of transmitted light	ω_{PEM}	Resonant frequency of PEM
I_0	Intensity of incident light	n_0	Unstrained refractive index of PEM
$\tilde{n}_+$	Complex refractive index for the LCP component of light	$n_x(t)$	Time-dependent refractive index of PEM in x-direction
$\tilde{n}_-$	Complex refractive index for the RCP component of light	Δn	Resultant difference in refractive index in PEM
k_+, k_-	Imaginary component of complex refractive index for LCP and RCP component respectively	$\delta(t)$	Periodical phase retardation of x-component of electric field
n_+, n_-	Real component of complex refractive index for LCP and RCP component respectively	β	Phase modulation amplitude
E_0	Component of incident electric field along y-axis of PEM	D	PEM crystal thickness
$\boldsymbol{E_1}$	Transmitted electric field along y-axis of PEM	ΔL	Optical path difference between two components of light
$\boldsymbol{E_2}$	Electric field transmitted through polarizer after PEM	$H_{applied}$	Magnetic field applied by electromagnet
I_2	Intensity of light reaching detector after polarizer and PEM	λ_P	Peak wavelength of PL map
J_n	n^{th} order Bessel functions	$\Delta\lambda_P$	Peak wavelength red-shift
μ_B	Bohr magneton	d	Separation of light excitation and collection points in PL measurements

List of figures

Acknowledgements

I would like to express to my gratitude to my Ph.D. advisors Sayantani Ghosh and Jennifer Q. Lu for their support and guidance on academic, professional, and personal issues throughout graduate school. They have been the best mentors I could have ever wished for and I cherish their mentorship.

I would like to thank my lab mates for their assistance and collaboration. In particular, Som Sarang for his invaluable help in preparing hybrid Perovskite thin films and developing the theory used in understanding the interaction between hybrid Perovskite thin films and ZnO substrates; Mark Bartolo for teaching and helping me with setting up and calibrating the magneto-optical Kerr effect (MOKE) spectroscopy setup. Special thanks are owed to Denzal Martin and Benaz Mendewala for their contribution to my work.

I would like to thank Prof. Boaz Ilan and his student Christine Hoffman for the Monte Carlo simulations performed on the hybrid Perovskite thin film luminescent solar concentrators, which greatly enhanced our understanding of the processes happening in the devices and improved the quality of our work.

I would like to thank Prof. Vincent C. Tung and Dr. Hidetaka Ishihara for their help in learning the methylammonium iodide purification procedure and preparation of hybrid Perovskite thin films. Their advice and assistance was vital in successfully completing a large portion of the work presented in this dissertation.

I would like to thank Jose Flores for teaching me how to prepare ZnO nanowires and helping me understand the ZnO electrodeposition process better in order to successfully complete my work.

I would also like to thank Prof. Yat Li and his student Bin Yao from UC Santa Cruz for providing hematite nanowire/Au nanoparticle samples which enabled the completion of a significant portion of work in this thesis. I would like to thank Prof. Art Ramirez from UC Santa Cruz for the MPMS data on the hematite samples.

I acknowledge the funding support I received during my studies, which includes support from the Merced nAnomaterials Center for Energy and Sensing (MACES), the Southern California Edison fellowship, the Dan David Solar fellowship, and UC Merced Physics Graduate Group summer fellowships. The funding from these sources has allowed me to concentrate on completing my work in a timely manner and produce quality results, and I am forever grateful.

Chapter 4 has been published under K. Nikolaidou, S. Sarang, C. Hoffman, B. Mendewala, H. Ishihara, J. Q. Lu, B. Ilan, V. Tung, S. Ghosh, Adv. Optical Mater. 2016, 4, 2126.[1] Copyright 2016 WILEY-VCH Verlag GmbH & Co. KGaA Weinheim. I would like to acknowledge my co-authors Som Sarang, Christine Hoffman, Benaz Mendewala, Hidetaka Ishihara, Jennifer Q. Lu, Boaz Ilan, Vincent Tung, and Sayantani Ghosh. The dissertation author is first author on the publication.

Chapter 5 has been published under K. Nikolaidou, S. Sarang, D. Martin, V. Tung, J. Q. Lu, S. Ghosh, Adv. Mater. Interfaces 2018, 5, 1800209.[2] Copyright 2018 WILEY-VCH Verlag GmbH & Co. KGaA Weinheim. I would like to acknowledge my co-authors Som Sarang, Denzal Martin, Vincent Tung, Jennifer Q. Lu, and Sayantani Ghosh. The dissertation author is first author on the publication.

Curriculum Vitae

Katerina Nikolaidou

Ph.D. Candidate, Physics
University of California, Merced, School of Natural Sciences
5200 N. Lake Rd. Merced, CA 95344
Advisors: Prof. Sayantani Ghosh, Prof. Jennifer Lu

Education

- University of California, Merced (Merced, CA) August 2014 – current

  Ph.D. in Physics (GPA=4.0/4.0; 4.0=A)

- Imperial College London (London, UK) September 2012 – September 2013

  MSc in Sustainable Energy Futures (Distinction)

- University of Bristol (Bristol, UK) October 2008 – July 2012

  MSci in Physics (First Class Honors)

Fellowships and Awards

- MACES Summer Fellowship award, Summer 2019

  Awarding institution: Merced Nanomaterials Center for Energy and Sensing, University of California, Merced

- Award for excellence in contribution to outreach activities in academic year 2017-2018

  Awarding institution: University of California, Merced

- Dan David Solar Fellowship award, Spring 2018

  Awarding institution: University of California, Merced

- Physics Graduate group and MACES summer fellowship award, Summer 2017

  Awarding institution: University of California, Merced

- Southern California Edison fellowship award, Spring 2017

  Awarding institution: University of California Merced
- Physics Graduate group summer fellowship award, Summer 2016

  Awarding institution: University of California, Merced

- Best academic performance in the first year in Physics, 2014-2015

  Awarding institution: University of California, Merced

- Academic scholarship, 2008-2012

  Awarding institution: State Scholarships Foundation of Cyprus

Experience

- Graduate Student Researcher, University of California, Merced, August 2014 – current:
  Project 1: Hybrid Perovskite luminescent solar concentrators.
  Project 2: ZnO structures as electron transport layer for Perovskite thin films.
  Project 3: Magneto-plasmonic heterostructures for sensing applications.

- Teaching Assistant, University of California, Merced, August 2014 – Spring 2019:
  Physics 160: Modern Physics Lab (Spring 2019)
  Physics 010: Modern Physics (Fall 2018)
  Physics 009: Physics II (Spring 2018)
  Physics 018: Physics I for Biologists (Fall 2014, Spring 2015)

- MACES outreach program, Buhach Colony High School, Summer 2016 – Spring 2017:
  Demonstrated and guided students on solar water splitting experimental modules.

- Leonardo Da Vinci Lifelong Learning Program Intern, Isotrol, Seville, Spain, January 2014 – April 2014:
  Assisted in finding appropriate equipment for PV plants according to EU regulations, and identified and prepared offers for prospective clients.

Publications

- Katerina Nikolaidou, Som Sarang, Christine Hoffman, Benaz Mendewala, Hidetaka Ishihara, Jennifer Q. Lu, Boaz Ilan, Vincent Tung, and Sayantani Ghosh, Hybrid perovskite thin films as highly efficient luminescent solar concentrators, *Advanced Optical Materials* **2016**, 4, 2126 – 2132 https://doi.org/10.1002/adom.201600634

- Katerina Nikolaidou, Som Sarang, Denzal Martin, Vincent Tung, Jennifer Q. Lu, Sayantani Ghosh, Tuning excitonic properties of pure and mixed halide perovskite thin films via interfacial engineering, *Advanced Materials Interfaces* **2018**, 5, 1800209 https://doi.org/10.1002/admi.201800209

- Katerina Nikolaidou, Som Sarang, Sayantani Ghosh, Nanostructured Photovoltaics, *Nano Futures*, **2019** https://doi.org/10.1088/2399-1984/ab02b5

- Benaz Mendewala, Katerina Nikolaidou, Som Sarang, Christine Hoffman, Vincent Tung, Boaz Ilan, Sayantani Ghosh, Exploring the roles of morphology and composition in hybrid perovskite luminescent solar concentrators, *Solar Energy* **2019**, 183, 392 https://doi.org/10.1016/j.solener.2019.03.042

Conferences and Workshops

- **Materials Research Society Meeting in Phoenix, Arizona, Spring 2016**, Poster presentation: 1D and 3D Zinc Oxide nanostructures for exciton binding energy tuning in hybrid Perovskite films.

- **American Physical Society March Meeting in New Orleans, Louisiana, Spring 2017**, Oral presentation: ZnO structures as electron extraction layers for Perovskite thin films.

- **American Physical Society Far West Meeting in Merced, California, Fall 2017**, Oral presentation: The effect of electron transport layers on the excitonic properties of hybrid perovskite thin films.

- **American Physical Society March Meeting in Los Angeles, California, Spring 2018**, Oral presentation: Using interface engineering to tune excitonic properties of halide and mix-halide perovskite thin films.

- **Materials Research Society Meeting in Boston, Massachusetts, Fall 2018**, Poster presentation: Modification of excitonic properties of halide and mix-halide hybrid Perovskite thin films using interface engineering.

- **Light/matter interactions at the Nano-bio interface**, University of Illinois at Urbana-Champaign, Fall 2016, Workshop.

- **Hands On Photovoltaic Experience, National Renewable Energy Laboratory, Summer 2017**, Workshop and Poster presentation: ZnO substrates as electron extraction layers for hybrid Perovskite thin films.

Society Memberships

- American Physical Society
- Materials Research Society

Abstract

Role of nanostructured interfaces in photovoltaic and sensing applications

by
Katerina Nikolaidou

Doctor of Philosophy in Physics

University of California, Merced

2019

Professor Michael Scheibner, Chair

Nanostructured materials are at the forefront of device and materials physics research due to their novel and favorable characteristics that offer the potential of surpassing previously achieved device efficiencies. This dissertation explores such materials, with specific focus on their interfacial properties, which could be implemented in semiconductor devices, including photovoltaics and highly responsive sensors. The first project in the dissertation focuses on an investigation of the potential of hybrid organic-inorganic Perovskite thin films as luminescent solar concentrators. Luminescent solar concentrators were first explored as an alternative to solar cells in the 1970s, and typically consist of high refractive index substrates doped with fluorescent materials, used to absorb incident sunlight and down-convert solar radiation which is subsequently collected by a solar cell attached to the edge of the luminescent solar concentrator. Commonly implemented materials have encompassed fluorescent dyes and quantum dots, but have not yet exceeded the device efficiencies of solar cells, and these fluorophores suffer from limited stability, narrow absorption spectra and low quantum yield. Therefore, hybrid Perovskite thin films possess a range of characteristics that render the material suitable for luminescent solar concentrators: it demonstrates a broad absorption spectrum, high refractive index of 2.5 which is significantly higher than typically used glass or polymer, and quantum yield reaching 80%, the combination of which is promising for efficient confinement of re-emitted light. In this work, hybrid Perovskite thin films are successfully implemented as luminescent solar concentrators, with optical efficiency reaching 29%, whereas the devices remain operational after 7 weeks of storage in ambient conditions underling the stability of optical properties of hybrid Perovskite thin films. Furthermore, the study extends to an investigation of different Perovskite compositions to identify the optimum precursor and thickness for high device performance, reaching optical efficiencies of 34.7% for 150-300 nm thick samples. 3D Monte Carlo simulations have demonstrated the scalability of these devices up to 100 cm in length, further establishing hybrid Perovskite thin films as successful candidates for optoelectronic devices.

The second project in the dissertation investigates the interaction of hybrid Perovskite thin films with ZnO substrates of varying degrees of surface roughness, as these are often used in Perovskite solar cells. The goal of this study is to complete a systematic investigation of the effects of the ZnO substrate on the excitonic properties of the hybrid Perovskite thin films, as most of the current research focuses on device studies and performance, whereas understanding of the fundamental processes occurring at the interface and how these can be tuned by tailoring the interface morphology is somewhat limited. The work performed here has produced some surprising results. While single crystalline ZnO substrates appear to perform best as electron extraction layers and are thus suited for implementation in a solar cell, substrates of higher surface roughness, such nanostructures and microstructures, have the opposite effect and result in confinement of electron-hole pairs within Perovskite grains. This conclusion is reached through electron microscopy studies correlated with charge transfer properties, probed via temperature, power, and time-resolved photoluminescence (PL). ZnO single crystal/hybrid Perovskite thin film interfaces show quenched PL intensity and reduced recombination lifetime as compared to a control sample of hybrid Perovskite thin film on glass, both indicative of efficient electron transfer between the two materials. On the other hand, microstructured ZnO/hybrid Perovskite thin film interfaces show a mild enhancement of the PL signal at room temperature, whereas nanostructured ZnO/hybrid Perovskite thin film interfaces demonstrate a 30 thousand-fold enhancement of the PL while significantly reducing the recombination lifetime. These results vary with temperature, indicate that with increasing substrate roughness, the Perovskite grain size is reduced and some grain separation is observed, further supporting the result that excitons are confined within individual grains which is deleterious to both electron transport and electron transfer. As a result, this work provides evidence of tuning of Perovskite excitonic properties using the substrate and can be leveraged for various types of applications depending on the end-goal.

The third project in this dissertation is a study of the enhancement of magneto-optical properties of hematite nanowires using excitation of localized surface plasmon resonance of Au nanoparticles (NPs). Magneto-plasmonics is a recent area of research which combines the properties of magnetism and plasmons to produce devices of superior performance. The basic premise is to leverage the increased local electric field of plasmonic NPs to enhance the magneto-optical response of ferromagnetic materials, or to use the magnetization of the ferromagnetic material to produce a narrower plasmon resonance that would be more sensitive to changes in the surrounding medium. While significant portion of magneto-plasmonic research has been focused on ferromagnetic metals, metal oxides offer some benefits over metals, such as superior stability and lower optical losses. Among iron oxides, hematite is the most abundant material and is low cost, while a breadth of techniques is available to fabricate various types of nanostructures. This enables the preparation of nanowires which offer the possibility of enhanced magneto-optical properties compared to a hematite film due to shape and magnetic anisotropy. As a result, this work shows that Kerr rotation can be observed using hematite nanowires, which was previously thought unlikely due to their weak ferromagnetism at room temperature, and decorating the nanowires with AuNPs results in enhanced Kerr rotation when the optical excitation is spectrally matched to the localized surface plasmon resonance (LSPR) of the AuNPs. Some dependence on the loading of AuNPs is observed, as lower loading of

AuNPs is beneficial for enhancing the real part of Kerr rotation – changing the angle of polarization the reflected light – whereas higher loading has a greater effect on the imaginary part of Kerr rotation – the ellipticity of reflected light. The outcomes of this work are important in demonstrating that hematite can be implemented in sensing applications when combined with plasmonic nanoparticles to improve performance.

Chapter 1

Motivation and overview

This dissertation is focused on using optical spectroscopy techniques to characterize the quality of nanomaterials and to understand the physical processes at their interfaces to improve the understanding and performance of novel photovoltaic and sensing devices. This chapter offers the motivation for the work described in this dissertation. The physics and scientific background behind the concepts discussed in this dissertation are explained in chapter 2, and chapter 3 discusses the experimental techniques that are used to obtain the results described in this dissertation. Chapters 4 through 6 describe the work performed and chapter 7 offers a summary and conclusion.

The first project discussed here is the study of hybrid Perovskite (PVSK) thin films as luminescent solar concentrators (LSCs). LSCs are typically high refractive index photoluminescent materials which absorb sunlight and re-emit at a lower energy, waveguiding the emitted light to the edge of the LSC, to which a solar cell is attached. Since the area of an LSC is larger than that of the solar cell, it results in a concentration effect. LSCs offer benefits of low cost due to the cheaper materials used, and the smaller sizes of solar cells implemented, whereas the emission of the LSC can be engineered to spectrally match the absorption of the solar cell. Furthermore, LSCs offer ease of fabrication compared to solar cells. However, the efficiency of LSCs has been limited, with maximum optical efficiency reaching 40 % using Lumogen F Red dye in polymer. Common materials for LSCs include dyes which suffer from photobleaching, and narrow absorption spectra, and quantum dots which have undergone extensive studies to eliminate toxicity, and photodegradation, but they still oxidize and suffer from low quantum yield which has prevented high efficiencies. Therefore, the need for new materials for LSCs is still present in order to generate efficient devices. PVSKs possess a few favorable properties that are desired in LSC materials; they have demonstrated impressive quantum yield, high refractive index, and broad absorption spectrum. Chapter 4 describes the results obtained from this project. PVSK LSCs achieved high optical efficiencies reaching up to 29 %, with devices remaining operational after 7 weeks of storage in ambient conditions.

The second project focused on a systematic study of the effect of surface roughness of ZnO substrates, typically implemented as electron transport layers in PVSK solar cells, on the excitonic properties of PVSK thin films. The motivation for this project was that despite the prominence of PVSK thin films in solar cell research and the study of the PVSK material itself, studies on the impact of the electron transport layer structure on the PVSK thin film have been limited. Therefore, a thorough investigation of the interaction between the two materials, both in terms of electron transfer or of the effect on the material itself would provide guidelines on optimum solar cell architecture to achieve high efficiency. The results are described in chapter 5, where three types of ZnO substrates, nanostructured,

microstructured, and single crystalline, were used as substrates for PVSK thin films and characterized using optical spectroscopy. Optimum substrates for different types of applications were identified, with the ZnO single crystal acting as an efficient electron extraction layer, and the ZnO nanostructure as an amplifier of the PVSK emission.

The third project studied the interaction of Au nanoparticles and hematite nanowires for the purpose of improving the magneto-optical properties of hematite nanowires, which could prove useful in a variety of applications, including data storage and optical sensors. Significant research effort has focused on improving the magneto-optical properties of various materials, which inclusion of plasmonic nanoparticles rising to prominence in recent years, as excitation of plasmon resonance and enhancement of the local field has shown to lead to improved magneto-optical properties. Materials that have been usually incorporated in such devices have included ferromagnetic metals for their magneto-optical properties, and Au thin films or nanoparticles for their superior stability and plasmonic properties. More recently, metal oxides which demonstrate magneto-optical properties have been identified as a better composite of such magneto-plasmonic heterostructures due to their stability and lower optical loss. Among metal oxides, hematite is a promising component due to its abundance and low cost. Nevertheless, its use in magneto-optical devices has so far been limited, due to limited understanding of its magneto-optical properties and low magnetization. Consequently, in this project we investigated the magneto-optical potential of hematite nanowires, and the effect of Au nanoparticles on the magneto-optical properties of hematite. Chapter 6 discusses the results obtained, which indicate strong coupling occurring between the two materials, with Au nanoparticles successfully enhancing the magneto-optical performance of hematite nanowires after excitation of the plasmon resonance.

Chapter 2

Review of materials: properties and characteristics

In this chapter, the properties and characteristics of the materials discussed in this dissertation are described, including hybrid organic-inorganic Perovskite (PVSK) thin films, zinc oxide (ZnO), hematite (α-Fe_2O_3), and gold nanoparticles (Au NPs). Furthermore, the physics and applications localized surface plasmon resonance (LSPR) seen in metallic nanoparticles are discussed, as well as the magneto-optical effects seen in ferromagnetic materials, and how the two phenomena can be combined to achieve magneto-plasmonic coupling. The chapter first presents the optical and electrical properties of PVSK thin films, followed by a discussion on the optical and electrical properties of zinc oxide, and how they can be modified in the case of nanostructures. This is followed by a brief explanation of the operation of PVSK photovoltaics and luminescent solar concentrators, as well as the concept of exciton binding energy and its implications on device operation. Similarly, the optical, electrical, and magnetic properties of hematite are presented both for bulk and nanowires, followed with a discussion on magneto-optical phenomena in ferromagnetic materials, with a focus on iron oxides. The optical properties of Au NPs are also discussed, followed by an analysis on LSPR seen in Au NPs. The chapter concludes with a discussion on the physics behind magneto-plasmonic coupling, which can be achieved via a combination of Au NPs and hematite nanowires.

2.1 Hybrid organic-inorganic Perovskite thin films

2.1.1 Crystal Structure

Hybrid metal halide PVSK materials are characterized by the structure ABX_3, where A is a monovalent organic cation, often methylammonium (MA) but more recently formamidinium (FA) and cesium have been used, B is a metal cation, usually lead, and X is a halide anion, such as iodide, chloride or bromide.[3] The crystal structure of PVSK changes with temperature. At low temperatures, it is characterized by orthorhombic structure, above ~140 K it has a tetragonal phase, and when heated over 330 K, it has a cubic structure. [3] The room temperature structure of MA-based PVSK is depicted in figure 1.

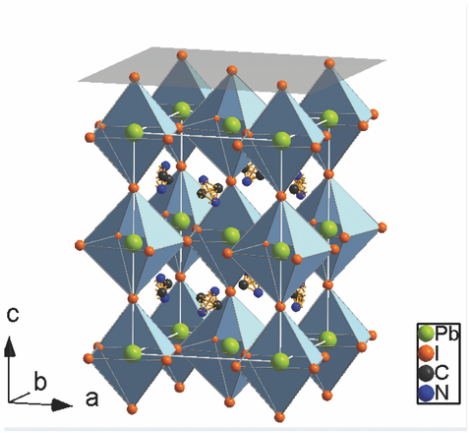

Figure 1. Room temperature crystal structure of $MAPbI_3$. Reproduced from reference [3] with permission. © 2015 WILEY-VCH Verlag GmbH & Co. KGaA, Weinheim.

The PVSK materials typically employed in applications are of the form $CH_3NH_3PbI_{3-x-y}Br_xCl_y$ and combine beneficial characteristics of the organic and inorganic components. Due to the former, highly crystalline PVSK films can be fabricated from solution processing at low temperatures and the bandgap of the resulting films can be altered by modifying the halide content of the precursor. Moreover, the material demonstrates high photoluminescence lifetimes and yields, and demonstrates high carrier mobility and long carrier lifetime, which allow for long carrier diffusion lengths.[3]

2.1.2 Electronic characteristics

The optical gap of $MAPbI_3$ has been estimated using optical absorption at room temperature to be ~1.6 eV,[4] which is smaller than the bandgap by an amount equal to the exciton binding energy. In all three phases $MAPbI_3$ is a direct-gap semiconductor.[5–7] This is beneficial for light absorption as it does not require any aid by phonons in the material and therefore, charge carrier generation is efficient.[8] The absorption coefficient has been estimated to be ~10^5 cm^{-1}, constituting $MAPbI_3$ as one of the most efficient photovoltaic (PV) materials in terms of light absorption.[8] The valence band of $MAPbI_3$ is mostly comprised of iodide p-states, whereas antibonding iodide p- and lead s-states contribute near the valence band maximum.[8] On the other hand, the conduction band mostly includes lead p-states, as expected by an ionic material.[8] Due to the presence of large atoms in $MAPbI_3$ strong spin-orbit coupling affects the band structure,[9] and reduces the band gap by ~1 eV, also reducing the effective masses.[9,10] The MA cation interacts non-covalently with the rest of the ions and fills the space between PbI_6 octahedra, allowing for PVSK structure to form at room temperature, which is not the case for all-inorganic PVSKs. Therefore, the organic molecule serves as a scaffold for the inorganic ions and produces optimal bond lengths that result in smaller bandgap and lower effective masses.[8]

Diffusion coefficients in $MAPbI_3$ have been found to be 0.05 – 0.2 cm^2s^{-1} and charge carrier mobility is in the range of 1 – 30 $cm^2V^{-1}s^{-1}$ for polycrystalline films.[8] Nevertheless, even though charge carrier mobility is moderate, the long charge carrier lifetime (up to >1 μs) ensures long diffusion lengths under illumination. The moderate mobility observed in $MAPbI_3$ has been attributed to lattice fluctuations which could act as a scattering mechanism.[8,11] Trap energies and densities in PVSK films have been estimated; shallow traps are present at ~0.2 eV from the band edge with density of 10^{16} cm^{-3} and deep traps of ~0.5 – 0.7 eV in the bandgap, with density of 10^{15} cm^{-3}, are present in $MAPbI_3$ films.[12–14] Grain boundaries have been found to reduce the photoluminescence efficiency of PVSK films and this reduction has been associated with deep trapping at the boundaries and significantly increased trap density at the grain boundaries compared to the bulk.[8,15] The transport properties of PVSK films are significantly influenced by the synthesis and processing techniques involved in their preparation. $MAPbI_3$ prepared based on lead acetate shows a lower defect density than $MAPbI_3$ prepared using lead iodide due to the reduced concentration of iodide which changes the chemical potential of iodide relative to lead, preventing the formation of deep traps.[16] Lead acetate as the lead source resulted in longer diffusion lengths than in films prepared with lead iodide, and in similar diffusion lengths as PVSKs prepared with lead chloride as the lead source.[16] Furthermore, the lead acetate-based Perovskite PVs demonstrated higher open circuit voltage than lead iodide-based devices, providing further proof of reduced density of deep traps.[17]

2.1.3 Optical characteristics

PVSK demonstrates favorable optical properties that make the material so suitable for PV applications. It has a broad absorption spectrum with absorption onset near 780 nm at room temperature, whereas the bandgap increases at low temperatures due to the change in phase of the material.[18,19] The bond lengths and angles are influenced by the phase and the distribution of MA in the crystal. Particularly, the Pb-I bond length and angle are determining factors for the bandgap of the material. When the ion positions rearrange as the material transitions from orthorhombic to tetragonal phase, the cell parameters are altered and the bandgap of the material changes accordingly.[19] The absorption spectra of PVSK at 300 K and 170 K are depicted in figure 2. PVSK photoluminescence is observed near the first excitonic peak of the absorption spectrum, indicating that most photophysical properties observed are excitonic processes.[18] The quantum yield (QY) of PVSK is impressively high, with films reaching QY values higher than 70 %,[18] and PVSK quantum dots reaching QY values of 93 %,[20] or near 100 % when cooled down.[21] Consequently, PVSK has been implemented in devices based on its emission properties, such as lasers [22] or LEDs [23].

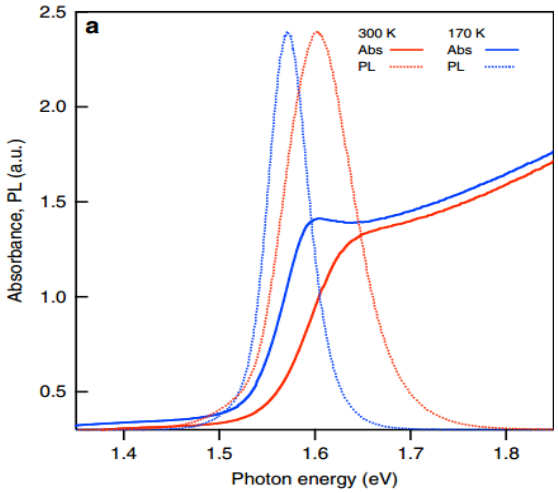

Figure 2. Absorption and emission spectra of $CH_3NH_3PbI_3$ film at 170 K and 300 K. Reproduced from reference [18] with permission. © 2014 Springer Nature.

2.2 Zinc Oxide

2.2.1 Crystal structure

ZnO is a II-VI compound semiconductor with ionicity at the borderline between covalent and ionic semiconductors. ZnO can demonstrate three different crystal structures: hexagonal wurtzite, which is the thermodynamically stable phase under ambient conditions, cubic zinc blende, which can be stabilized only by growth on cubic substrates, and cubic rocksalt, which can be obtained at relatively high pressures.[24] These crystal structures are depicted in figure 3 below.

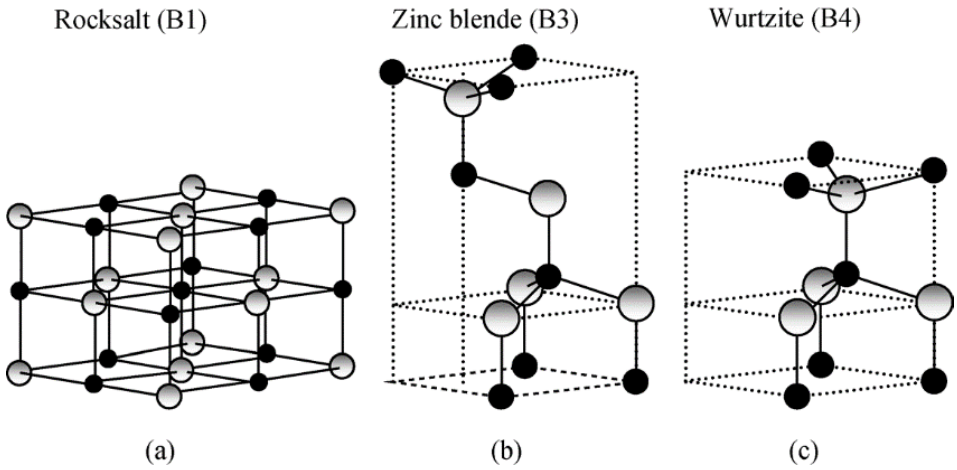

Figure 3. Crystal structures of ZnO. (a) cubic rocksalt, (b) cubic zinc blende and (c) hexagonal wurtzite. Gray is Zn atoms and black is Oxygen atoms. Reproduced from reference [24] with permission. © AIP Publishing.

The wurtzite structure consists of a hexagonal unit cell with two lattice parameters, α and c, that are related by: $\frac{c}{\alpha} = \sqrt{8/3}$. The structure is composed of two interpenetrating hexagonal close-packed (HCP) sub-lattices, each consisting of one type of atom and displaced relative to each other along the c-axis by 3/8.[24] Zinc blende ZnO is metastable and can be stabilized by heteroepitaxial growth on cubic substrates, such as ZnS.[25] It is composed of two interpenetrating Face Centered Cubic (FCC) sub-lattices shifted along the body diagonal by ¼ of the length of the diagonal. There are 4 atoms per unit cell and every atom of each type is tetrahedrally coordinated with four atoms of the other type and vice versa.[24] Wurtzite ZnO can be transformed to the rocksalt structure at relatively modest external hydrostatic pressures. The reduction of lattice dimensions causes the interionic Coulomb interaction to favor the ionicity more over the covalent nature.[24] The rocksalt structure cannot be stabilized by epitaxial growth. Pressure induced phase transition occurs in the range of 10 GPa, associated with a large decrease in volume of ~17 %.[26] This high-pressure cubic phase has been found to be metastable for long periods of time even at ambient pressure and above 100 °C.[26] Since none of the structures possess inversion symmetry, the crystal exhibits crystallographic polarity, which dictates the direction of the bonds. For the wurtzite structure, the primary polar direction is <0001>. Various properties of the material depend on this polarity, such as growth, etching, defect generation and piezoelectricity. Therefore, <0001> is the most common direction for growth.[24]

2.2.2 Band structure

The band structure of ZnO consists of three closely spaced valence bands, as shown in figure 4, close to the band center (Γ point). The A, B and C bands are the heavy-hole, light-hole and crystal field split-off bands, respectively, and are a consequence of spin-orbit coupling and crystal field splitting near the band center.[24] The splitting energies between the bands are indicated in figure 4. The electronic band structure varies with temperature and pressure as the lattice constants change. The temperature dependence of the lattice constants of ZnO has been expressed as second-order polynomials:[27]

$$\alpha(T) = 3.2468 + 0.623 \times 10^{-5}T + 12.94 \times 10^{-9}T^2 \quad (1)$$

$$c(T) = 6.2042 + 0.522 \times 10^{-5}T + 12.13 \times 10^{-9}T^2 \quad (2)$$

The band gap at the Γ point reduces with increasing temperature, with the dependence given empirically by the following expression:[28]

$$E_g(T) = E_g(T = 0) - \frac{\alpha \cdot T^2}{T + \beta} \quad (3)$$

where $\alpha = -5.5 \times 10^{-4}$ eV/K and $\beta = -900$ K for $T \leq 300$ K. The band gap is equal to 3.3 eV at 300 K.[29] On the other hand, the band gap of wurtzite ZnO demonstrates sub-linear increase with increasing hydrostatic pressure.[30]

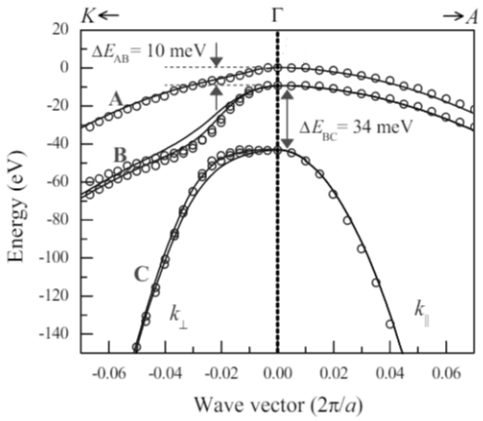

Figure 4. Splitting energies between the three valence bands in ZnO. Reproduced from reference [24] with permission. © AIP Publishing.

2.2.3 Electronic properties

ZnO is a direct and large band gap semiconductor, which offers multiple benefits in its use in electronic and optoelectronic devices. The large band gap allows for high temperature and high power applications, low noise generation and the ability to support large electric fields. At low electric field, the energy provided to the electrons by the applied field is smaller than the thermal energy of the electrons, thus leaving the electron energy distribution unaffected and the electron mobility independent of the applied field. Hence, Ohm's law is obeyed.[24] On the other hand, when the energy the electrons gain by the external field is substantial, the electron distribution varies from the equilibrium case. Therefore, hot electrons are created, with electron drift velocity higher than the steady-state value.[24]

The main scattering mechanisms that dominate electron transport processes in ZnO include: (a) ionized impurity scattering due to deflection of free carriers by the long-range Coulomb potentials of the charged centers formed by defects or intentionally doped impurities. (b) Optical phonon scattering caused by the interaction of a moving charge with an electric field induced by electric polarization associated with lattice vibration. (c) Acoustic phonon scattering through deformation potential due to strain caused by acoustic phonons that results in energy change of the band edges. (d) Piezoelectric scattering due to electric fields generated by the strain associated with phonons in a crystal without inversion symmetry. (e) When there is high density of dislocations and native defects in a semiconductor, dislocation scattering and scattering through defects is also likely. In the case of dislocation scattering, acceptor centers are introduced along the dislocation line and capture electrons from the conduction band of an n-type semiconductor. Dislocation lines become negatively charged and a space charge region is generated, scattering electrons traveling across the dislocations, eventually reducing electron mobility.[24] The highest room-temperature electron mobility reported so far for a single crystal of bulk ZnO is $205\ \mathrm{cm^2V^{-1}s^{-1}}$ with carrier concentration of $6.0 \times 10^{16}\ \mathrm{cm^{-3}}$.[31] However, the mobility value has been predicted to be $\sim\ 300\ \mathrm{cm^2V^{-1}s^{-1}}$ by Monte Carlo simulations.[32]

Wurtzite ZnO is naturally n-type due to intrinsic or extrinsic defects, which were usually attributed to Zn-on-O anti-site, Zn interstitial and O vacancy. Nevertheless, since none of the native defects demonstrate high-concentration shallow donor characteristics,[33] it is now suggested that the presence of hydrogen during ZnO preparation is responsible for the n-type conductivity.[34] Large amounts of hydrogen can easily diffuse into ZnO due to its high mobility and subsequently act as a source of conductivity and a shallow donor in ZnO.[34]

2.2.4 Optical properties

ZnO crystals demonstrate two luminescence bands; high energy band near the absorption edge, which is in the ultraviolet part of the spectrum, and a broad low energy band, which is usually green,[35] as depicted in figure 5. The UV band has a maximum of 3.35 eV, decay time of ~ 0.7 ns and is of excitonic nature: free excitons and bound excitons.[36] The luminescence intensity of the UV band increases with decreasing nanoparticle size, whereas the band half width reduces for increasing particle size.[37] Luminescence quenches with increasing temperature as described by:[35]

$$I(T) = \frac{I_0}{1+Ae^{-E_a/kT}} \quad (4)$$

where *I(T)* is the luminescence intensity at temperature *T*, I_0 is the intensity at 0 K, E_a is the activation energy and *A* is a constant. E_a has been estimated to be 59.0 meV for a ZnO crystal [37] and 59.7 meV for a ZnO thin film,[38] which agree with the estimated exciton binding energy of 60 meV. The position of the UV band changes with temperature, according to eq. 3, where $E_g(T=0)$ is 3.360 eV and α is 0.67 meV/K.[39] The concentration of free electrons was also found to influence the position of the maximum of the UV band: at concentration of 10^{13} cm^{-3} the maximum was located at 3.312 eV, but it shifted to 3.27 eV when the concentration increased to 10^{18} cm^{-3} and the change is attributed to a band gap width reduction.[40]

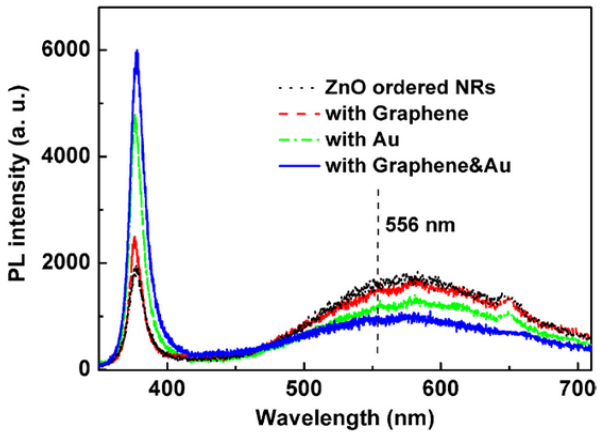

Figure 5. Typical photoluminescence spectrum of ZnO. Reproduced from reference [41] with permission. © 2014 IOP Publishing Ltd.

The origin of green luminescence in ZnO is controversial and has been associated with impurity copper ions, zinc vacancies, oxygen vacancies, interstitial zinc ions, oxygen anti-sites and transitions, or that various centers contribute to luminescence simultaneously.[35] Calculations have been used to demonstrate that green luminescence is produced by recombination of conduction electrons by zinc vacancy acceptor levels, with the ground level lying 0.8 eV higher than the valence band maximum.[33] Others have demonstrated that green luminescence is consequence of electronic transition between ground and excited states of a shallow donor to the deep acceptor (zinc vacancy).[42] Moreover, an oxygen vacancy origin of green luminescence has been suggested.[43] Experimental data places the energy level of oxygen vacancies 0.9 eV above the valence band maximum, allowing for green luminescence as shown in figure 6 below. Work based on annealing of samples and magnetic resonance has confirmed green luminescence from oxygen vacancies.[44]

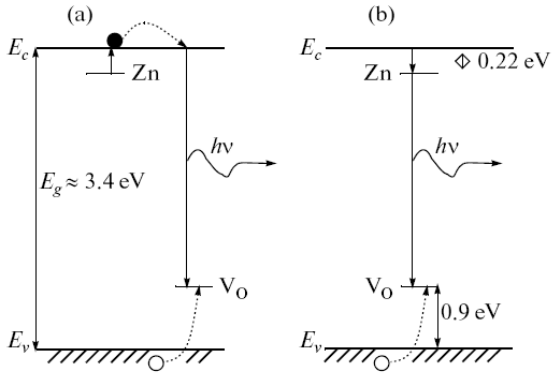

Figure 6. Recombination mechanism for oxygen vacancy model that results in green luminescence (a) at high temperature (~300 K) and (b) at low temperature (<50 K). Reproduced from reference [45] with permission. © AIP Publishing.

Temperature dependence measurements have shown that green luminescence at low temperatures occurs via recombination of electrons at interstitial zinc ion centers with holes at the oxygen vacancy level, whereas at high temperature conduction band electrons recombine with oxygen vacancy holes, since electrons from the interstitial zinc ion levels transfer to the conduction band at high temperatures.[45] Exciton transfer to oxygen and zinc vacancy levels is also found to occur.[35,44]

2.3 Perovskite photovoltaics

Perovskite photovoltaics (PPVs) have been suggested as a solution to multiple problems currently available PV technologies have to face, such as high financial and energy costs and low efficiency that cannot match that of fossil fuel technologies. Due to the ease of preparation of PPVs and aforementioned favorable electronic characteristics of PVSK films, PPVs have emerged as a possible low cost and efficient PV technology. The operating principle of PPVs is different from that of a typical p-n junction Silicon solar cell and is summarized in figure 7.[46] Incident solar light excites an electron in the PVSK

film, which serves as the light harvesting medium in these devices, to generate an electron-hole pair. Subsequently, the electrons and holes are separated by transfer to the electron transport layer (ETL) and hole transport layer (HTL) that are in contact with the PVSK film. ETL is a medium that shows good electron conductivity and blocks holes, whereas HTL shows good hole conductivity and blocks electrons from the PVSK layer. Therefore, once the electrons and holes reach the respective layers they can be efficiently transported to the contacts of the solar cell that are often a transparent conductive oxide on glass and a metal contact (Ag, Au, Al, etc.). The presence of ETL and HTL allows Fermi level equilibration, which creates a sufficient electric field to extract the charge carriers in the device.[46]

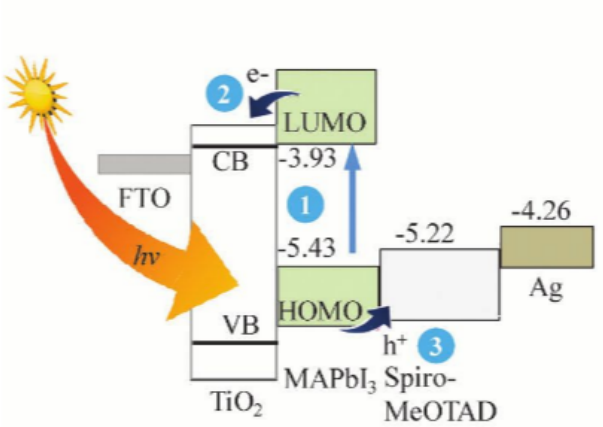

Figure 7. Operating principle of a PPV. (1) Excitons are generated in the PVSK film by incident illumination. (2) Electrons are transferred from the PVSK layer to the ETL. (3) Holes are transferred from the PVSK layer to the HTL. Reproduced from reference [46] with permission. © The Royal Society of Chemistry 2016.

Charge separation in the PVSK film can be initiated in two ways; electron injection to the ETL or hole injection to the HTL. However, this process is in kinetic competition with other processes occurring simultaneously that could reduce the device performance. Photo-generated excitons in the PVSK film could be recombined prior to charge separation, either radiatively or nonradiatively. Moreover, electrons and holes could recombine with holes in the HTL and electrons in the ETL respectively, when close to the interface between the PVSK film and the charge carrier transport layer.[46]

PPVs were first fabricated in 2009, using $MAPbI_3$ as the light harvester and TiO_2 as the ETL, reaching power conversion efficiency (PCE) of 3.81 %.[47] Soon after a device that employed $MAPbI_3$ as both the light harvesting medium and the HTL, based on TiO_2 as the ETL was fabricated, reaching PCE of 7.3 %.[48] The PVSK layer was used in solar cells with liquid electrolytes, but was observed to quickly dissolve, leading to the fabrication of solid state devices, and the emergence of spiro-OMeTAD as the HTL, enhancing the PCE to 9.7 %.[49] In 2012, research groups started reporting PPVs fabricated with mixed halide PVSK ($CH_3NH_3PbI_{3-x}Cl_x$) that offered greater device stability and enhanced charge carrier transport.[10,50] TiO_2 had originally been chosen as the ETL, not only because of its favorable electron conduction properties, but also due to its

mesoporous nature that allowed for higher surface area. Similarly, incorporation of insulating Al_2O_3 as scaffold for deposition of the PVSK layer has been investigated and was observed to boost the open circuit voltage (V_{oc}) of the device.[46] Both Al_2O_3 and TiO_2 were combined to enhance PCE, reaching 12.0 %.[51] Among the various HTL employed poly-triarylamine appeared to be one of the best choices.[46] Incorporation of bromide in the PVSK precursor was found to enhance the stability of PVSK films in moisture, which has been the most major bottleneck PPVs must overcome before they can be commercialized. This has been associated with transition of the crystal structure from tetragonal to pseudo-cubic due to the smaller ionic radius of bromide.[46,52] PCE of 16.2% was achieved by the combination of $CH_3NH_3PbI_{3-x}Br_x$ and poly-triarylamine as HTL and TiO_2 as ETL.[53] Yttrium-doped TiO_2 has been proven to enhance PCE due to its superior electron transport properties.[46]

Enhanced PCE was achieved when two-step deposition of $MAPbI_3$ was used instead of single step deposition, as this improved the morphology of the PVSK film.[54] On the other hand, combination of MA and FA in the PVSK layer, lead to efficiency of 20.1 %,[55,56] whereas mixing MA, FA and Cesium in the precursor has been observed to enhance device stability.[57]

Interface engineering is an area of major interest in prolonging device lifetime and efforts to enhance device stability have included incorporation of metal oxide layers as both the HTL and ETL in a device, using Nickel oxide and ZnO films respectively. Such devices were still operational 60 days after fabrication.[58] Nevertheless, ZnO-based PPVs, or when other metal oxides were used as ETL, have not reached the PCE values obtained with TiO_2-based PPVs, since most of the work done has been focused on using the latter as ETL. However, ZnO offers certain benefits over TiO_2: it can be fabricated at low temperatures, meaning that flexible PV is possible, whereas nanostructure fabrication is easier with ZnO, allowing for different types of device architectures. Therefore, it is imperative to study different possibilities for ETL and HTL in order to identify the best material for optimum performance and stability. For successful efforts in achieving this, understanding of the photo-physical processes occurring at the interface of PVSK film and ETL is crucial.

2.4 Exciton binding energy in PVSKs

Performance of solar cells is dominated by the optical properties of the light harvesting medium, especially absorption efficiency, which is dependent on the bandgap of the material used. The optical gap of a material can be estimated by the absorption onset, which indicates the minimum energy required to create an exciton. Electrons and holes experience electrostatic attraction after optical excitation forming bound excitons. Since these excitons are localized to the molecule, additional energy is required to form free charge carriers, which are responsible for electrical conductivity. This extra energy is the exciton binding energy (E_B) which is defined by the difference between the bandgap (transport gap) of the material and the optical gap.[8] E_B can also be considered as a measure of exciton stability against thermal dissociation. For efficient PV devices, E_B must be small as it is the determining factor for the amount of free charge carriers present. E_B values for $MAPbI_3$ in the tetragonal phase have been derived from various types of

experiments, with reported values reaching 55 meV.[18,59–62] Recent magneto-absorption measurements have yielded an E_B value of less than 5 meV at room temperature,[63] indicating that thermal energy at room temperature (~25 meV) might be sufficient to dissociate the $MAPbI_3$ excitons. Since E_B can be a determining factor in the performance of a device, systematically tuning the E_B would enable fabrication of improved devices. E_B has been previously altered in core-shell quantum dots, where increase in shell thickness reduced E_B further, due to greater separation between bound electrons in the conduction band of the shell and holes in valence band of the core.[64] Theoretical calculations have also confirmed this phenomenon, where increased separation of electrons and holes reduces the exciton binding energy in an AlAs/GaAs type-II heterojunction.[65]

E_B has been frequently estimated by fitting equation 4 to temperature dependent photoluminescence (PL) data; [66] in this case E_a is E_B, I_0 is the PL intensity at 0 K and A is a constant. Nevertheless, this approach does not take into account the varying contributions of bound excitons and free charge carriers in the material, thus giving inaccurate E_B values.[59] In order to extract more accurate E_B values, inclusion of the different contributions to PL must be considered. The fraction of free charges (x) to the total density of excitation for a 3D semiconductor is given by the Saha-Langmuir equation:[59,67]

$$\frac{x^2}{1-x} = \frac{1}{n}\left(\frac{2\pi\mu k_B T}{h^2}\right)^{3/2} e^{-E_B/k_B T} \quad (5)$$

where μ is the reduced exciton mass (~ $0.15m_e$ [60]) and n is the total density of excitation and can be expressed as $n = n_{FC} + n_{exc}$, where n_{FC} is the density of free charge carriers and n_{exc} is the density of excitons.[59] According to this expression, as T increases, more free charge carriers are present, rather than excitons. It has been estimated that for realistic excitation density at room temperature (less than 10^{15} cm^{-3}), free charge carriers dominate the PL signal. However, as temperature decreases, excitonic contributions dominate.[59] Based on this model, it is expected that PL intensity will follow a quadratic trend with increasing illumination power, due to the non-geminate recombination of free charge carriers to generate an emitted photon. On the other hand, emission from bound excitons is expected to increase linearly with increased excitation power.[18,68] This distinction between linear and quadratic dependence on excitation power can only be observed if the incident illumination is pulsed, since for continuous wave illumination charge carrier generation and recombination are in dynamic equilibrium, leading to a linear increase in PL with excitation power even for free charge carriers.[18,69,70]

2.5 Luminescent solar concentrators (LSCs)

LSCs are made of glass or plastic substrates doped with some luminescent species that absorb incident light and re-emit at a longer wavelength; due to the high refractive index of the substrate, the light is confined within the substrate and is transported to the edges by total internal reflection where PV cells are attached, as depicted in figure 8.[71–73] Due to the large ratio between the surface to edge areas of the LSC, there is a

concentration effect and the photon density reaching the PV cell is increased. Furthermore, by choosing suitable luminescent species, the emission can be matched to the bandgap of the PV cell, enhancing the photo-generated current.[74]

LSCs offer various benefits, such as low cost, due to the inexpensive substrates and small amount of PV material used at the edge.[75] Moreover, LSCs work under both direct and diffuse light, negating the need for tracking mechanisms.[71,75] Efficient LSC materials rely on high QY and good dispersion of the material over the substrate, among other properties. Therefore, the LSC potential of PVSK thin films can be used to assess the quality of the films fabricated, since grain boundaries result in non-radiative recombination that reduces QY. This can be achieved by estimating the optical efficiency of LSCs:[74]

$$\eta_{opt} = \frac{I_{LSC} \cdot A_{PV}}{I_{PV} \cdot A_{LSC}} \quad (6)$$

where I_{LSC} and I_{PV} represent the current generated in the PV cell with and without the LSC, and A_{PV} and A_{LSC} are the areas of the PV cell and LSC respectively. It is expected that the higher the optical efficiency, the higher the quality of the PVSK films.

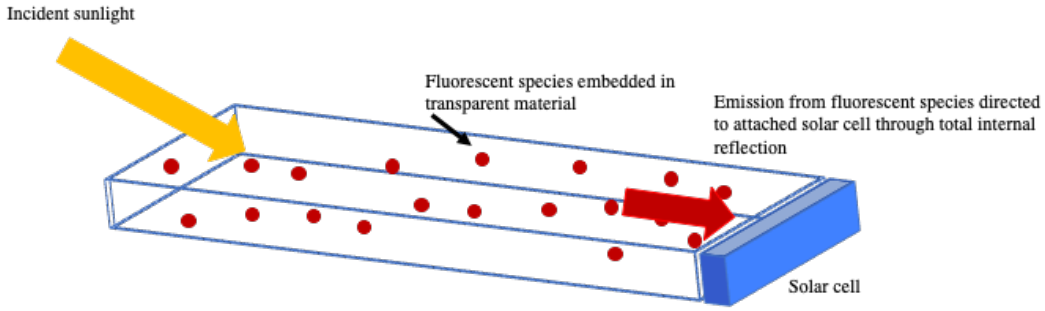

Figure 8. Operating principle of a LSC. Reproduced from reference [76] with permission. © 2019 IOP Publishing Ltd.

2.6 Hematite

Hematite is one of the most abundant materials on earth, making it readily available and low cost.[77] Furthermore, it is non-toxic and possesses extraordinary environmental stability.[77–80] Due to its favorable optical band gap (reported values range from ~1.8 eV to 2.2 eV), hematite has attracted much scientific interest recently for implementation in photoelectrochemical water splitting devices.[77–80] However, since it also possesses interesting magnetic properties, work has also been done to better understand its magnetic behavior and how it can be leveraged for various applications, although work in this area is more limited than work including other types of iron oxides, such as maghemite or magnetite, as they exhibit stronger magnetization.[81,82]

2.6.1 Crystal structure

The most thermodynamically stable form of iron oxide under ambient conditions is hematite, and therefore it is very abundant and low-cost. Hematite crystallizes in the corundum structure, shown in figure 9 below.[77,81,83] The corundum structure is trigonal-hexagonal scalenohedral, with lattice parameters $a = 5.0356$ Å and $c = 13.7489$ Å, and has six formula units per unit cell.[77,84] The O^{2-} anions are arranged in a hexagonal closed-packed lattice in the [001] direction, whereas the Fe^{3+} cations occupy two thirds of the octahedral interstitial sites in the (001) basal planes, with the tetrahedral sites remaining vacant. This arrangement results in formation of FeO_6 octahedra with common edges with three neighboring octrahedra and a common face with one octahedron, which results in trigonal distortion. This is due to repulsion between iron atoms to optimize the Madelung energy of the crystal, and as a result there are two different Fe-O bond lengths.[77,84]

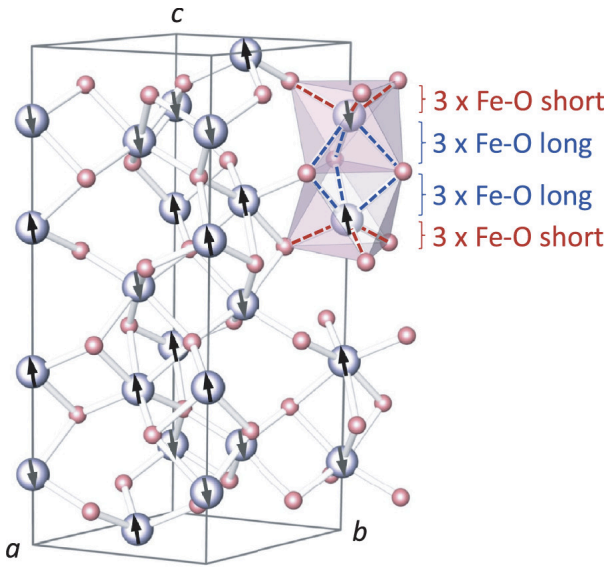

Figure 9. The unit cell of hematite. Electrostatic repulsion between Fe^{3+} cations results in long and short Fe-O bonds. Reproduced from reference [85] with permission. © AIP Publishing.

2.6.2 Optical properties

The hematite bandgap values vary from 1.9 eV to 2.2 eV depending on the fabrication method used.[77] Tauc analysis has shown that hematite exhibits indirect bandgap transition, although more recent work has demonstrated direct bandgap due to quantum size-effects.[77,86–90] The absorption spectrum of hematite starts from the near-infrared region of the spectrum, with a smaller absorption coefficient, extending to the visible and ultraviolet region, with much higher absorption coefficient at energies higher than the bandgap energy.[77,91] The variation in absorption coefficient values with wavelength is shown in figure 10.

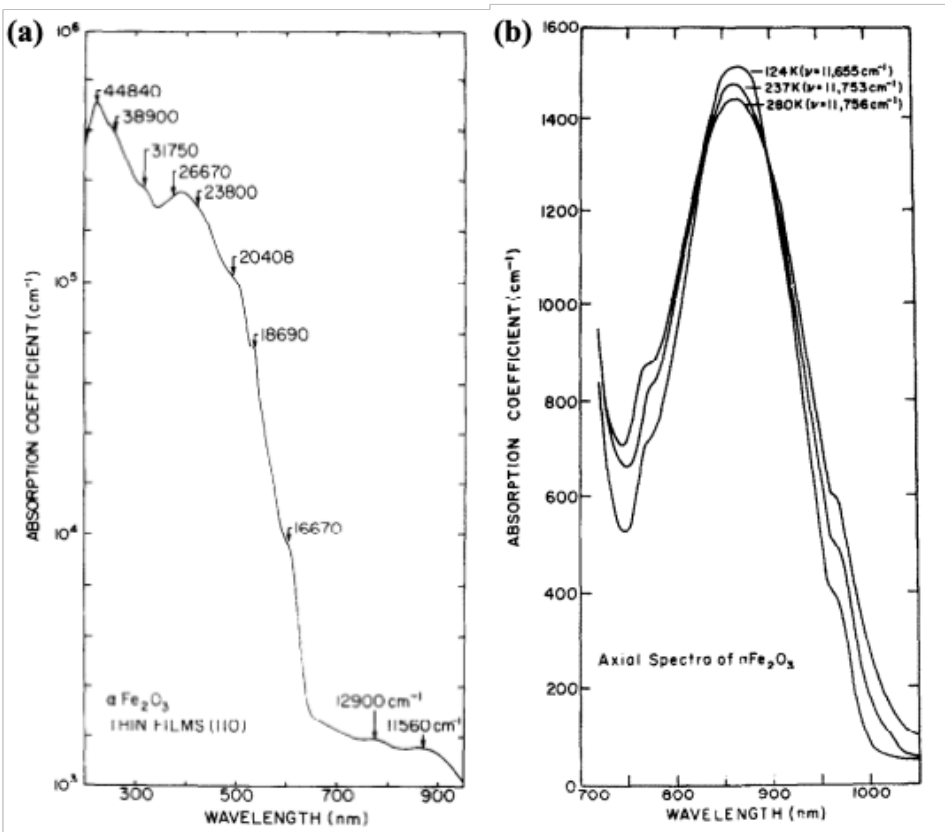

Figure 10. (a) Absorption coefficient of α-Fe_2O_3 as a function of wavelengths between 200 nm – 950 nm at 298 K, (b) absorption coefficient of a single crystal of α-Fe_2O_3 as a function of wavelengths between 700 nm – 1100 nm at various temperatures. Reproduced from reference [89] with permission. © 1980 Published by Elsevier Ltd.

Optical absorption of hematite nanoparticles demonstrates a blue-shift in absorption along with reduced intensity as the nanoparticle size decreases.[92–95] Blue-shift in absorption was also seen in hematite nanotubes, with the absorption blue-shifting as the length of the nanotubes reduced, whereas variations in the absorption spectrum of hematite were also seen with shape changes.[92,96,97] Optical absorption of hematite was enhanced by doping with Sn, which distorted the hematite lattice and led to a 2-fold improvement of the optical absorption coefficient.[83]

However, bulk hematite PL has proven challenging due to the forbidden d-d transition, lattice and magnetic relaxations, as well as resonant energy transfer between cations.[92,98] PL has been observed due to trap states in nanostructures, as the forbidden d-d transitioning rule is relaxed due to quantum confinement effects, along with weaker magnetic relaxations that result in long-lived excited states.[92,99,100] Hematite nanoparticles have demonstrated fluorescence quantum yield of 10^{-5}, a value indicative of fast nonradiative recombination processes, which limit excited state lifetime.[77,94,101] Further studies have shown that nanoparticles exhibit very short excited state lifetimes (100 ps) with the electron relaxation attributed to capture of electrons in oxygen-deficient Fe^{3+} centers.[92,94] Overall, variations in size of nanoparticles showed longer time constants for smaller nanoparticles due to size-dependence of steady state absorption of carriers in

the extended band that contains Fe 4sp and O 2p orbitals.[92,102] However, changes of the shape of nanoparticles did not result in changes of the lifetime.[92,96] Thin films, which were about 100 nm thick and eliminated surface states that are present in the case of nanoparticles, showed hot electron relaxation in 300 fs and subsequent recombination with holes or trap states in 3 ps, with the trap states lasting for hundreds of picoseconds before relaxation to the ground state.[77,101] Furthermore, single-crystalline hematite exhibited shorter excited state lifetime compared to polycrystalline hematite, which was attributed to the defect states in the single crystal being of different nature and absorbing more in long wavelengths, dominating the transient response.[92,101]

Doping of hematite with Zn, Co, Cr, and Cu did not enhance the excited state lifetime.[92,94] While doping with Ti and Sn did not modify the lifetime values, the former resulted in higher absorption decay amplitude,[92,103] which was linked to lower electron-hole recombination, whereas the latter resulted in morphological changes that also did not modify charge carrier dynamics.[78,92] Combination of hematite with other metal oxides has also been investigated. Combination with WO_3 has shown shorter lifetimes due to enhanced electron trapping for certain wavelengths, which however the absorption signal increased as the probe wavelength approached bandgap values, as it is believed that the extraction of surface-trapped holes was promoted.[92,104] Similar results were observed for Ti_xO_y-doped hematite.[92,105]

2.6.3 Electronic properties

Early work has shown that hematite possesses low electrical conductivity (10^{-14} $\Omega^{-1}cm^{-1}$), conduction electron concentration of 10^{18} cm^{-3} at 1000 K, and electron mobility of 10^{-2} $cm^2V^{-1}s^{-1}$.[77,106,107] Its conduction is characterized by polaron hopping, meaning that mobility increases with temperature.[77,108–110] Hematite single crystals also have low electrical conductivity (10^{-4} $\Omega^{-1}cm^{-1}$) and showed anisotropic electron transport, as conduction along the iron bilayer basal plane is up to ten thousand-fold times larger than perpendicular directions.[77,111–113] This is attributed to the magnetic structure of hematite which results in ferromagnetic coupling of spins in the basal planes and antiferromagnetic coupling in the perpendicular direction, forbidding electrons to hop across oxygen planes. Consequently, conduction in the [001] direction is only achieved through movement of holes (Fe^{3+}-Fe^{4+} electron transfer) which is significantly slower.[77,110] As a result, research has focused on incorporating dopants to enhance hematite conductivity. This allows for preparation of p-type hematite with inclusion of Mg^{2+} and Cu^{2+} impurities, and n-type hematite, by incorporating Ti^{4+}, Sn^{4+}, Zr^{4+}, Nb^{5+}.[77,110] Inclusion of Zr^{4+} has led to conductivity of 0.1 $\Omega^{-1}cm^{-1}$ and electron mobility of 0.1 $cm^2V^{-1}s^{-1}$.[111] Another example is the inclusion of Ti^{4+}, which improved conductivity through polaron hopping by substituting Fe^{3+} and reducing Fe^{3+} to Fe^{2+}.[78,114–117] It has been deduced that while some dopants introduce inter-bandgap energy levels, some have no discernible effect on the bandgap or absorption coefficient.[77,110,118] On the other hand, doping with Si led to formation of hematite dendrites which increased surface area and reduced the hole diffusion length, suppressing electron-hole recombination.[78]

2.6.4 Magnetic properties

The orientation of the spin magnetic moment of the iron atoms is influenced by the arrangement of the oxygen anions and high-spin cations.[77] Bulk hematite is antiferromagnetic below its Néel temperature of 955 K, and has a Morin transition at 260 K below which the two magnetic sub-lattices are antiparallel and oriented along the rhombohedral [111] axis (c-axis).[81,119,120] Above the Morin transition temperature (T_M), due to distortion of the FeO_6 octahedra which destabilizes the anti-parallel spin arrangement, it results in slightly canted arrangement of the moments in the basal (111) plane leading to a net magnetization.[77,81] Therefore, hematite is weakly ferromagnetic at room temperature.[77,117,121] T_M varies with the shape, size, crystallinity, and surface of particles.[120] In particular, T_M decreases with smaller particle size, dropping below 4 K for sizes below 8-20 nm, due to lattice expansion, as well as effects of strain and defects.[81,119,120] It has been found that addition of impurities and vacancies also reduce T_M.[120] Similarly, hematite nanorods and nanowires also show a lower T_M value than bulk, with previously reported values ranging from 4 K to 170 K for nanowire diameters from 20 nm to 120 nm.[119,122,123] An investigation of hematite particles with various morphologies has demonstrated that weakly ferromagnetic and anti-ferromagnetic phases coexist below T_M, with the population of weakly ferromagnetic depending on the morphology; needle-like particles showed the highest population of weakly ferromagnetic phases, with more than 50 % below 150 K.[120,124] In addition, the Morin transition disappeared entirely in mesoporous hematite and hematite nanotubes and this result was attributed to long-range magnetic ordering.[120,125,126] It is worth noting that in cases of different materials where the Morin transition was not observed, a magnetic phase transformation was seen in nanocrystals at low temperatures, which was attributed to surface spin disorder. Disordered spins could be the result of adatoms adsorbed on the particle. However, at low temperatures, the exchange interaction dominates and spins become ordered leading to higher magnetization.[120,127–129]

2.6.5 Magnetic anisotropy and shape anisotropy in hematite nanorods and nanowires

Magnetic anisotropy defines the properties of magnetic nanowires and nanorods. Magnetization along a crystal orientation is favored by magnetocrystalline anisotropy, which often competes with shape anisotropy for textured nanowires. In the case of bulk hematite, the magnetocrystalline anisotropy field is given by:[120,130]

$$\boldsymbol{H}_{K_1} = -K_1(cos^2\theta_1 + cos^2\theta_2)/2 \quad (7)$$

where K_1 is the anisotropy energy constant, θ_1 and θ_2 are the angles of the magnetization sub-lattices along the c-axis. The Morin transition is reflected in the sign of K_1: for $K_1<0$, $T>T_M$: atomic moments lie in the basal plane to minimize magnetocrystalline anisotropy energy, whereas for $K_1>0$, $T<T_M$: atomic moments lie along the c-axis.

The shape anisotropy field for a single nanowire is given by:[131]

$$\boldsymbol{H}_{A,shape} = \boldsymbol{M}_S \times \Delta \boldsymbol{N} \tag{8}$$

where $\Delta \boldsymbol{N}$ is the demagnetization difference between the long and short axis of a nanowire, which increases with aspect ratio. Shape anisotropy favors the long axis of a nanowire and it competes with magnetocrystalline anisotropy, with the resultant direction minimizing the total energy.[120] Magnetization lies along the long axis of a nanowire if the magnetocrystalline direction is along the long axis of the nanowire or if the shape anisotropy energy exceeds the magnetocrystalline anisotropy energy significantly.[120]

For an array or nanowires, magnetostatic interactions must be considered. The field $\boldsymbol{H}_Z$ of one nanowire at a distance x, assuming that the nanowire consists of two magnetic charges a distance l from each other, and a dipole moment (m) of $\boldsymbol{M}_sV$ is given by:[131]

$$\boldsymbol{H}_Z = \frac{m}{(x^2+\frac{l^2}{4})^{3/2}} \tag{9}$$

This expression indicates that the interaction of densely packed nanowires would reduce coercivity compared to a single nanowire.[131,132]

In the case of an external stress σ, a magnetoelastic anisotropy field is present and is given by:[131]

$$\boldsymbol{H}_{A,magnetoelastic} = \frac{3\lambda_S \sigma}{\mu_0 \boldsymbol{M}_S} \tag{10}$$

where λ_S is the magnetostrictive constant. Therefore, these four different contributions combine to control the coercivity of the nanowires.

Effects of shape anisotropy have been previously observed in hematite nanowires and nanorods. Typically, bulk materials show a change from multi-domain type to single-domain type with decreasing grain size. In the case of hematite, the critical size for this change is larger than 15 μm as the saturation magnetization ($\boldsymbol{M_S}$) is low, as single-domain particles are characterized by a $\boldsymbol{M_R/M_S}$ value of 0.5, where is $\boldsymbol{M_R}$ remanence, pseudo-single-domain particles have a ratio value of 0.1 – 0.5, and for multi-domain particles $\boldsymbol{M_R/M_S}$ is lower than 0.1.[120,133,134] It was observed that hematite nanorods of diameters ranging from 20 – 100 nm and length below 2 μm, showed multi-domain behavior, with pseudo-single-domain behavior in nanorods shorter than 500 nm.[120] This deviation from conventional behavior is attributed to competition of magnetocrystalline anisotropy and shape anisotropy in the nanorods. Additionally, differences in the magnetic behavior of hematite nanowires and nanotubes were observed; nanowires showed T_M of 166 K, whereas nanotubes showed long-range magnetic ordering which suppressed the Morin transition. This difference was attributed to the defects in the nanotubes due to the curl.[126]

2.7 Magneto-optical Kerr effect

Magneto-optical (MO) effects refer to the interactions between a magnetic material and incident light, and have been crucial in the early development of electromagnetism and quantum theory of matter.[135,136] One of the first detections of MO effects was the Faraday effect, which refers to changes in the polarization state of incident linearly polarized light after propagation through a magnetic material in a magnetic field parallel to the propagation direction, and it was first detected in 1845.[135,137,138] Since this discovery sparked research on materials showing MO effects, the magneto-optical Kerr effect (MOKE) was detected in 1877, and it refers to the changes in polarization state of incident light upon reflection from a magnetic material.[135,139,140] MOKE has been utilized to investigate surface magnetization of thin films, whereas materials that demonstrate MO effects have been implemented in optical devices for mode-conversion waveguiding and data storage, among others.[135,140] Ferromagnetic materials, such as cobalt, iron, and nickel have been particularly popular for MOKE as they provide useful results for practical applications.[136] The domains of these materials are aligned under an applied magnetic field, and the magnetization of the material results in a small rotation of the plane of polarization of incident light. Furthermore, incident p-polarized light becomes elliptically polarized after reflection. The origin of this effect will be explained in more detail below.

Linearly polarized electromagnetic wave can be considered as a superposition of two circularly polarized waves: left-circularly polarized (LCP) and right-circularly polarized (RCP), each with amplitude $E_L = E_R = E/2$.[135] On the other hand, an elliptically polarized wave is the superposition of two linearly polarized waves whose amplitudes and phase differ. When linearly polarized light travels through a material with free electrons fixed about positive centers, the electric field of LCP and RCP force the electrons into left and right circular motion respectively, as shown in figure 11 below.

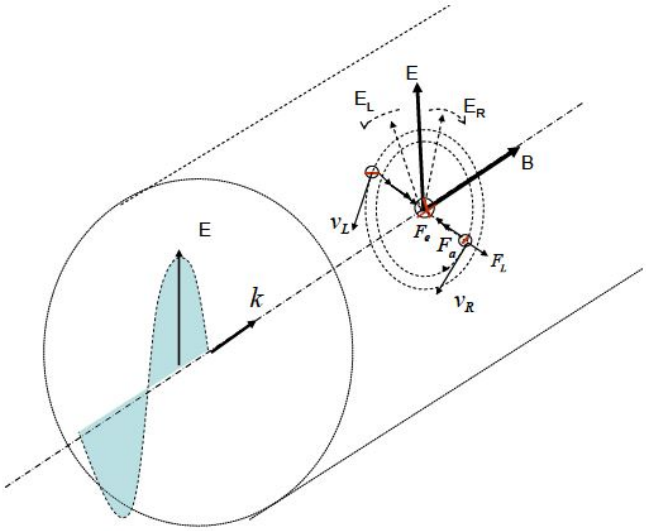

Figure 11. Motion of free electrons in the case of MO effects. Reproduced from reference [135] with permission. © 2017 Scientific & Academic Publishing.

Figure 11 shows a force $F_a = -kr$ which is a result of the attractive force between the electron and the positive center, where r is the radius of the circular orbit of the electron. If there is no applied magnetic field, the left and right circular orbits are equal, given by:[135]

$$eE_{L,R} + kr_{L.R} = m\omega^2 r_{L,R} \Rightarrow r_{L,R} = \frac{eE/2m}{(\omega^2 - {\omega_0}^2)} \tag{11}$$

where ω is the angular frequency of the incident wave, m is the electron mass, ${\omega_0}^2 = k/m$ depends on the material, and E is the amplitude of the incident electric field. Considering the electric dipole moment $\boldsymbol{p}$ and $\boldsymbol{D} = \varepsilon \boldsymbol{E} = \varepsilon_0 \boldsymbol{E} + \boldsymbol{P}$, where $\boldsymbol{P} = N\boldsymbol{p}$, the dielectric constant is:[135]

$$\varepsilon = \varepsilon_0 \left(1 + \frac{\frac{Ne^2}{2m\varepsilon_0}}{\omega^2 - {\omega_0}^2}\right) \tag{12}$$

Since $n^2 = \varepsilon_r = \varepsilon/\varepsilon_0$, the RCP and LCP components experience the same refractive index and dielectric constant while traveling through the material.

In the case where there is an applied magnetic field along the direction of propagation, the electrons also experience Lorentz forces, as shown in figure 11. Therefore, the right-circular and left-circular radii are different:[135]

$$eE_{L,R} + kr_{L,R} \pm e\omega r_{L,R} B = m\omega^2 r_{L,R} \Rightarrow r_{L,R} = \frac{eE/2m}{(\omega^2 - {\omega_0}^2 \mp \frac{\omega Be}{m})} \tag{13}$$

Consequently, the refractive indices experienced by RCP and LCP components are different, resulting in a discrepancy in propagation velocities, and after traversing a distance L through the material, the two components have a phase difference of $\Delta\theta = (\frac{\omega L}{c})(n_L - n_R)$. Once the two components combine upon exit from the material, the resultant wave is linearly polarized with polarization direction rotated by $\theta = \Delta\theta/2$ with respect to the initial direction.[135] The different refractive indices can be used to obtain an expression for the rotation angle:

$${n_{L,R}}^2 = 1 + \frac{Ne^2/2m\varepsilon_0}{\omega^2 - {\omega_0}^2 \mp \omega Be/m} \cong n^2(1 \pm \xi) \tag{14}$$

$$n^2 = 1 + \frac{Ne^2/2m\varepsilon_0}{\omega^2 - {\omega_0}^2} \tag{15}$$

$$\xi = (\frac{\omega B}{m})(\frac{1}{\omega^2 - {\omega_0}^2}) \tag{16}$$

$$n_{L,R} \cong n(1 \pm \tfrac{1}{2})\xi \tag{17}$$

$$\theta = \frac{\omega L}{2c}(n_L - n_R) \cong \frac{\omega L n \xi}{2c} \cong \frac{ne}{2mc}\frac{\omega^2}{\omega^2 - {\omega_0}^2} LB \cong K(\omega)LB \tag{18}$$

Equation 18 shows that the rotation angle of the polarization after reflection is proportional to the applied magnetic field, and the distance L, with the proportionality constant being dependent on the wavelength of the incident light.[135]

For ferromagnetic materials, the magnetic field in equation 18 is given by $\boldsymbol{B} = \boldsymbol{B_0}(1 + \chi)$, where $\boldsymbol{B_0} = \mu_0 \boldsymbol{H}$ is the magnetic induction in vacuum and $\chi = \mu_0 \boldsymbol{M}/\boldsymbol{B_0}$ is the magnetic susceptibility. However, for ferromagnetic materials $\chi \gg 1 \Rightarrow \boldsymbol{B} = \boldsymbol{B_0}\chi = \mu_0 \boldsymbol{M}$, in which case the angle θ is proportional to the magnetization of the material and the distance L.[135] Nevertheless, the light traveling through a magnetized material does not only experience phase shift; the LCP and RCP components experience different absorption coefficients, and as a result the amplitudes of the electric fields are different, leading to ellipticity of the emergent light.[135] Consequently, the refractive index must be expressed in terms of complex parameters, in which the real part corresponds to the refractive index, and the imaginary part is the absorption coefficient. The perturbation of refractive index ξ in equation 17 is expressed as $\xi = \boldsymbol{Q} \cdot \boldsymbol{u_k}$, where $\boldsymbol{u_k} = \boldsymbol{k}/k$ and $\boldsymbol{k}$ is the vacuum wave vector, and $\boldsymbol{Q}$ is the Voight vector which is proportional to the magnetization.[135,141] Hence, the complex refractive index and complex polarization rotation are given by:

$$n_{L,R} \cong n\left(1 \pm \frac{1}{2}\right)\boldsymbol{Q} \cdot \boldsymbol{u_k} \tag{19}$$

$$\theta = \frac{\pi L n}{\lambda}\boldsymbol{Q} \cdot \boldsymbol{u_k} = \theta_k + i\varepsilon_k \tag{20}$$

where θ_k is the rotation angle and ε_k is the ellipticity of the exiting light.

MOKE has three different configurations, defined by the direction of M: polar, transverse, and longitudinal, as shown in figure 12.

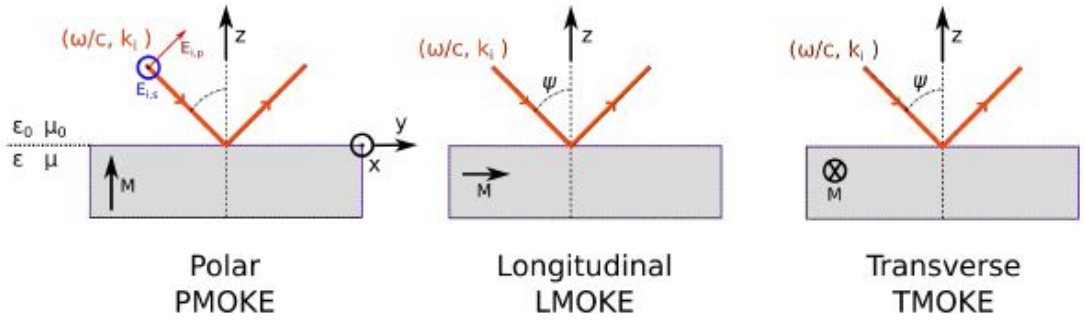

Figure 12. The different configurations of MOKE. Reproduced from reference [135] with permission. © 2017 Scientific & Academic Publishing.

For a linearly polarized wave with wavelength in the visible part of the spectrum that is incident perpendicularly on a ferromagnetic sample in air, with electric field $\boldsymbol{E}(t,z) \propto e^{-i(\omega t - kz)}$, the electric displacement $\boldsymbol{D}$ and magnetic induction $\boldsymbol{B}$ are given by:[135]

$$\forall\, i,j \in \{1,2,3\} \qquad \boldsymbol{D} = \varepsilon \boldsymbol{E} = \varepsilon_0 \varepsilon_r \boldsymbol{E} \Leftrightarrow D_i = \varepsilon_{ij}(\omega) E_j \tag{21}$$

$$\boldsymbol{B} = \mu \boldsymbol{H} = \mu_0 (\boldsymbol{H} + \boldsymbol{M}) \Leftrightarrow B_i = \mu_{ij}(\omega) H_j \tag{22}$$

where ε is the tensorial permittivity, ε_r is the relative permittivity, and μ is the permeability, which is close to μ_0, meaning that it can be expressed as $\mu_{ij} = \mu_0 \delta$, where δ is the Krönecker symbol. If the material is electrically neutral, we can assume:

$$\nabla \cdot \boldsymbol{D} = 0, \nabla \times \boldsymbol{E} = -\partial_t \boldsymbol{B}, \nabla \times \boldsymbol{H} = \boldsymbol{j} + \partial_t \boldsymbol{D} \tag{23}$$

where $\boldsymbol{j} = \sigma \boldsymbol{E}$, σ being the conductivity tensor. With effective permittivity expressed as $\varepsilon' = \varepsilon + i\frac{\sigma}{\omega}$, equation 23 can be written as:[135]

$$\frac{1}{\mu_0} \nabla \times \partial_t \boldsymbol{B} = \partial_t \boldsymbol{j} + {\partial_t}^2 \boldsymbol{D} \Leftrightarrow -\nabla \times \nabla \times \boldsymbol{E} = \omega^2 \mu_0 \left(i\frac{\sigma}{\omega} + \varepsilon \right) \boldsymbol{E} \tag{24}$$

$$k^2 \boldsymbol{E} - (k \cdot \boldsymbol{E}) = \frac{\omega^2}{c^2} \varepsilon' \boldsymbol{E} \tag{25}$$

Equation 25 can be expressed as:

$$(n^2 \delta_{ij} - n_i n_j - {\varepsilon'}_{ij}) E_i = 0 \tag{26}$$

using the complex refractive index $n_i = \frac{c}{\omega} k_i$. The non-zero solution of equation 26 leads to the Fresnel formula for normal modes of propagation. The off-diagonal terms are responsible for the MO effects and are functions of $\boldsymbol{M}$, whereas the dielectric tensor obeys magnetization reversal ${\varepsilon'}_{ij}(\boldsymbol{M}) = {\varepsilon'}_{ji}(-\boldsymbol{M})$. In the case of polar MOKE where $\boldsymbol{M}$ is along the z-axis, the permittivity tensor is given by:[135,136]

$$\varepsilon' = \begin{pmatrix} {\varepsilon'}_{xx} & {\varepsilon'}_{xy} & 0 \\ -{\varepsilon'}_{xy} & {\varepsilon'}_{xx} & 0 \\ 0 & 0 & {\varepsilon'}_{zz} \end{pmatrix}, {\varepsilon'}_{xy} \in i\mathbb{R} \tag{27}$$

For this case, the Fresnel equation yields zero for $n_{\pm}^2 = {\varepsilon'}_{xx} \pm i{\varepsilon'}_{xy}$, which can be substituted in equation 26 to obtain $E_x = \pm i E_y = e^{\pm i\pi/2} E_y$. This indicates two circularly polarized waves (LCP and RCP) propagating with refractive index n_+ and n_-. The induction can be expressed as:[135]

$$D_+ = n_+^2 \left(E_x + iE_y\right), D_- = n_-^2 (E_x - iE_y) \tag{28}$$

This shows that the incident light becomes elliptical after it is reflected from the magnetic material. The Fresnel coefficients for s- and p- polarizations of the reflected field E_r are estimated using the incident field E_i and the boundary conditions at the interface:

$$\begin{pmatrix} E_{r,p} \\ E_{r,s} \end{pmatrix} = \begin{pmatrix} r_{pp} & r_{ps} \\ r_{sp} & r_{ss} \end{pmatrix} \begin{pmatrix} E_{i,p} \\ E_{i,s} \end{pmatrix} \quad (29)$$

Therefore, the Kerr rotation (θ_{Kerr}) and Kerr ellipticity (φ_{Kerr}) can be extracted:[135,136]

$$\theta_{Kerr,s} = Re\left(\frac{r_{ss}}{r_{sp}}\right), \varphi_{Kerr,s} = Im\left(\frac{r_{ss}}{r_{sp}}\right) \quad (30)$$

$$\theta_{Kerr,p} = Re\left(\frac{r_{ps}}{r_{pp}}\right), \varphi_{Kerr,p} = Im\left(\frac{r_{ps}}{r_{pp}}\right) \quad (31)$$

The complex Kerr rotation in the polar configuration, where $r_{pp} = r_{ss}, r_{sp} = -r_{ps}$, can then be expressed as:[142,143]

$$\phi_{Kerr} = \theta_{Kerr} + i\varphi_{Kerr} = r_{ps}/r_{pp} \quad (32)$$

where r_{ps} is the pure MO contribution and r_{pp} is the pure optical contribution.

While little work has been done on observing MOKE on hematite as it was believed that the low $\boldsymbol{M_s}$ value would prevent domain observations due to low contrast, some early work using Faraday and Kerr effects demonstrated good contrast, and in the case of MOKE, the contrasts were more distinct than in the magnetite sample.[82,144] The success of the technique was attributed to the Kerr rotation depending on sub-lattice magnetization instead of the resultant spin-canting moment.

2.8 Localized surface plasmon resonance

Plasmonic nanoparticles have been particularly popular in applications that require enhancement in light absorption and scattering. They have been combined with metal oxide nanostructures and implemented in PV devices, solar water splitting, and solar fuel electrodes, among others.[145–147] Metallic NPs exhibit localized surface plasmon resonance (LSPR) when certain conditions are met: the electric permittivity of the NPs is negative and the wavelength of the incident light is much larger than the dimensions of the NP.[148] When light is incident on the NPs, conduction electrons are pinned by the incident electromagnetic wave to oscillate around their equilibrium positions, as depicted in figure 13.

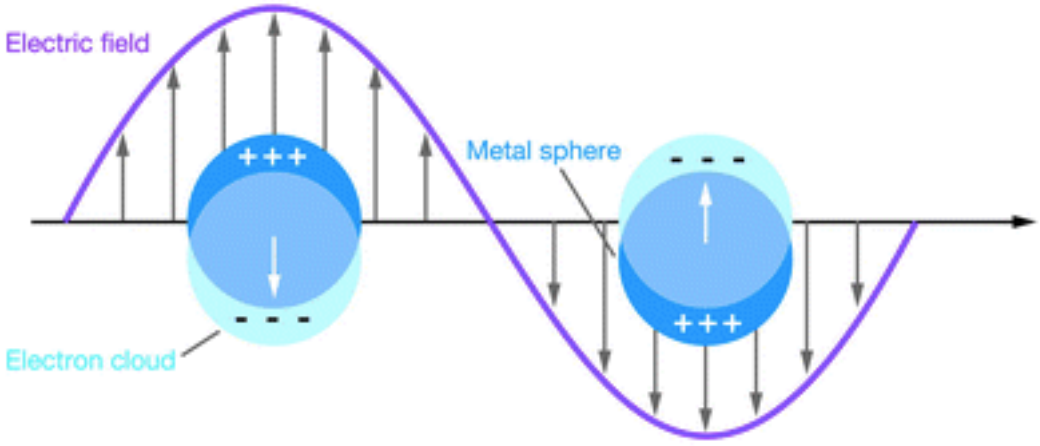

Figure 13. LSPR for a spherical gold NP. Reproduced from reference [149] with permission. © Annual Reviews.

This occurs only when the incident light frequency (ω) is close to the plasma frequency of the metal, which is in the visible frequency range for good conductors like gold and silver, and is defined as:[150]

$$\omega_P = \sqrt{\frac{4\pi n_e e^2}{m_e}} \tag{33}$$

where n_e is the free electron density and m_e is the mass of an electron. Therefore, the complex dielectric constant of the metal nanoparticle is given by:[150]

$$\varepsilon(\omega) = 1 - \frac{\omega_P^2}{\omega(\omega + i\gamma)} \tag{34}$$

Since for a metal, free electron density is very high, $\omega < \omega_P$, and thus the real part of $\varepsilon(\omega) < 0$. Negative permittivity is necessary for electric field enhancement by the LSPR. When a spherical NP is exposed to a uniform external field, which is the case for most NPs since the diameter is a few orders of magnitude smaller than the incident wavelength, a polarization vector is generated in the opposite direction of the incident field for negative ε, which induces a dipole field in the NP, with the same direction as incident field.[148,150] As a result, the two electric fields superimpose to enhance the external electric field. On the other hand, if the dielectric constant was positive, the incident field and induced dipole field would have opposite directions, resulting in attenuation of the external field. The net field gain can be expressed as:[150]

$$G(\omega) = \frac{E_{TOT}(\omega)}{E_0(\omega)} \approx 1 + \frac{\varepsilon(\omega) - \varepsilon_1}{\varepsilon(\omega) + 2\varepsilon_1} \cdot \left(\frac{r_m}{r + r_m}\right)^3 \tag{35}$$

where ε_1 is the permittivity of the surrounding medium and r_m is the radius of the NP. Based on this expression, LSPR can be achieved when $Re(\varepsilon) = -2\varepsilon_1$. Light extinction (absorption and scattering) are dependent on the dielectric constant of the NP, its size and geometry,

as well as the dielectric constant of the surrounding medium. Mie theory provides the expression for the extinction coefficient:[150]

$$A_{ext} = \frac{18\pi \cdot N_p \cdot V \cdot \varepsilon_1^{3/2}}{\lambda} \cdot \frac{Im(\varepsilon)}{[Re(\varepsilon)+2\varepsilon_1]^2+[Im(\varepsilon)]^2} \quad (36)$$

where N_p is the number of NPs of volume V. Similarly to the field gain, extinction is maximized when $Re(\varepsilon) = -2\varepsilon_1$. While $Re(\varepsilon)$ is associated with the resonance frequency of the plasmonic material, $Im(\varepsilon)$ is associated with the losses, which include Landau or radiative damping, metal heating, electron-electron scattering, as shown in figure 14, as well as structural imperfections, and intraband transitions, which is one of the dominant losses.[151–153] This leads to the definition of a quality factor for plasmonic nanoparticles:[151]

$$Q_{SPR}(\omega) = -\frac{Re(\varepsilon)}{Im(\varepsilon)} \quad (37)$$

Equation 37 shows that the quality factor depends solely on the complex dielectric function of the material and the higher the quality factor, the sharper the LSPR spectrum, which leads to stronger local field enhancement and higher optical extinction.[151]

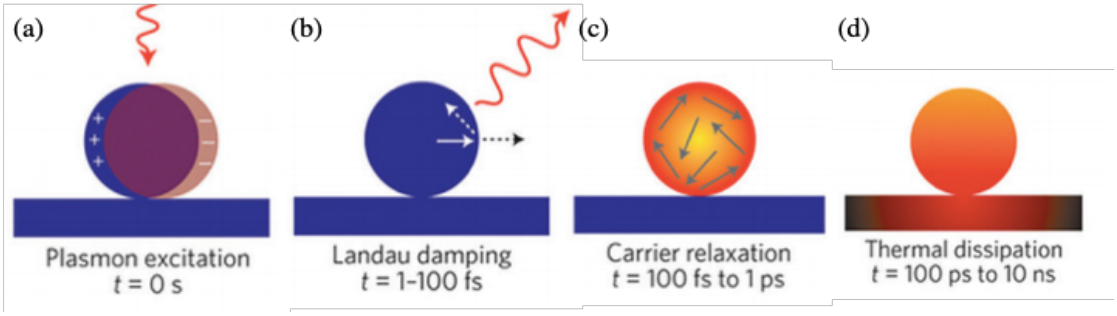

Figure 14. (a) Electron-hole pairs are formed after excitation of LSPR. (b) After 1-100 fs electron-hole pairs decay either via photon emission or via Landau damping and hot electron-hole formation. (c) At 100 fs – 1 ps, hot carriers undergo electron-electron scattering which results in energy loss. (d) In several ps to ns, electron-phonon scattering results in heat transfer from the NP to the surrounding environment. Reproduced from reference [154] with permission. © 2015, Springer Nature.

2.9 Au nanoparticles

A major benefit of plasmonic nanoparticles is the ease at which one can tune their properties through modifications of the material, morphology, and physical arrangement of the metallic NPs, which allows absorption and/or scattering of a broad range of wavelengths.[155] Among the various materials that have been exploited for their plasmonic properties, Au has been the most popular choice, and its plasmonic properties have been leveraged for many centuries as shown in figure 15.

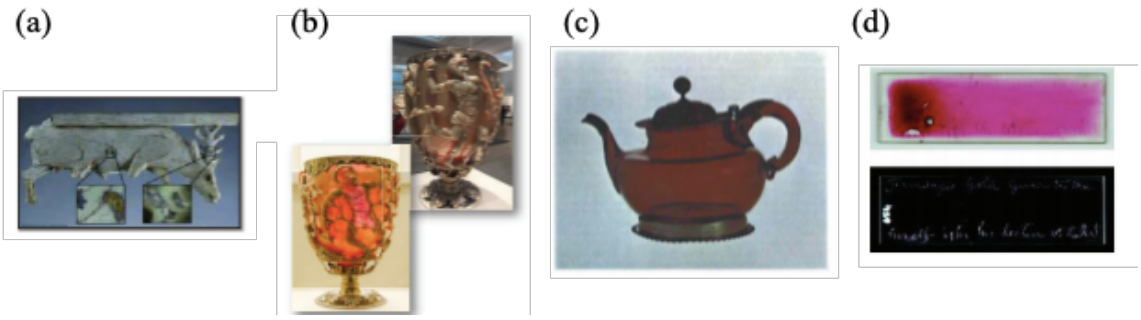

Figure 15. Examples of Au NPs used in products over the centuries. (a) Gold-plated Egyptian ivory from the 8th century BC, (b) the Lycurgus cup from the 4th century, (c) a teapot from 1680 colored using the Purple of Cassius method, and (d) Michael Faraday's gold colloid samples, which led to the first correlation between the optical properties and size of Au NPs. Reproduced from reference [151] with permission. © 2017 IOP Publishing Ltd.

Au has been successful as a plasmonic material due to its superior chemical and physical stability, which allows its implementation in various types of devices, the ability to modify its optical properties easily through variations of shape and size, as well as the ability to easily functionalize its surface with organic molecules.[151,156–158] Furthermore, Au NPs have demonstrated extraordinary light-to-heat conversion efficiency, high photostability, electromagnetic field amplification, and larger extinction cross-section than other chromophores, all characteristics that make them desirable for a large variety of applications.[151]

2.9.1 Morphological effects

The size of Au NPs dictates whether the NP acts as a scattering or absorbing material: if the diameter is much smaller than the wavelength of the incident radiation, absorption is the dominant effect.[151,159,160] On the other hand, as the NPs increase in size scattering becomes more important, becoming comparable with absorption for 50 nm Au NPs, and dominating for NPs larger than 70-100 nm.[151,161] This distinction is important when it comes to integration with applications as it is the determining factor on the choice of Au NP size. Larger NPs are preferred for biolabeling, single-particle sensors, and nanolensing, whereas smaller NPs are preferred in heating applications.[151,162–165] Au NPs that are small compared to the wavelength (25 nm or smaller), experience a uniform electric field distribution and coherent electron cloud polarization, leading to excitation of dipolar plasmon oscillations.[159,160] However, Au NPs with diameters comparable or larger than the incident wavelength (larger than 60 nm), the electric field is non-uniform and the electron cloud polarization is not coherent, resulting in multipolar plasmon oscillations. This effect manifests as broadening and red-shift of the LSPR spectrum for larger Au NPs and allows tuning of the LSPR over 60 nm by altering the diameter from 10 nm to 100 nm.[159–161] Reduction in Au NP size below 30 nm also has some intrinsic effects as electron scattering at the NP surface is a significant contribution to the electron relaxation rate as the NP size approaches the electron mean free path, which

is approximately 30 nm for Au.[160] Consequently, non-radiative losses increase, leading to almost complete LSPR quenching for Au NPs smaller than 2 nm.[166] For Au NPs with diameters 2 – 10 nm, quantum effects become important, as the lattice of the NP contracts, leading to an increase in electron density, and subsequently, higher frequency LSPR.[166][167]

Changes in the number, position, and width of the LSPR peak can be achieved via modifications in the shape of the Au NPs, such as fabrication of nanoshells, nanowires, nanocubes, among others.[168–176] Spherical Au NPs of diameters from 2 nm to 50 nm possess only one LSPR peak, which is centered at approximately 520 nm. However, for cylindrical Au NPs of the same size, two LSPR peaks appear, a blue-shifted one associated with the minor axis of the cylinder, and a red-shifted one associated with the major axis of the NP, which is more intense due to increase of the quality factor with wavelength.[177–179] The position of the latter can be readily tuned from the visible to the near-infrared part of the spectrum by increasing the aspect ratio of the nanoparticle.

2.9.2 Composition effects

As the properties of Au NPs depend on their complex dielectric constant, any changes in their composition results in alteration of ε and the LSPR spectrum.[152] This provides the means to control the optical properties of Au NPs via alloying or doping.[152,165,180] Nevertheless, this route is not commonly pursued as it involves more complicated synthesis, as well as the potential of other metals being inferior to Au in terms of plasmonic properties and stability, among others.[151–153,165] The inferior plasmonic performance could be a consequence of partially occupied d-states that increase the probability of inter-band transitions, which enhance LSPR relaxation and lead to lower quality factor.[151–153] Moreover, doped crystals or alloys have higher probability of electron-electron or electron-defect scattering.[152,153,180–182]

One successful combination is Au-Ag alloys, as Ag exhibits superior plasmonic characteristics and can be easily fabricated.[183–185] Indeed, Au-Ag alloys have demonstrated higher quality factor, and the LSPR frequency and width showed an almost linear dependence on the Ag:Au stoichiometric ratio.[151,152,183–187] On the other hand, alloys of Au with Cu, Pt, Pd, Co, and Ni have all been unsuccessful due to reduced quality factor, which was attributed to inter-band transitions in the visible range or reduced LSPR intensity.[151,152,187–191] Furthermore, reduced quality factor has been estimated for Au alloys with Si, Al, and Sn.[152,187,192] Fe-Au alloys have exhibited damped LSPR and reduced local field enhancement, whereas absorption is enhanced in the red and NIR part of the spectrum due to introduction of new electron transitions, which could be leveraged for photothermal applications.[151,165,180,181,193–195] Therefore, these results show that alloyed nanoparticles could result in enhanced properties that would be useful for various applications.

2.9.3 Tunability range and limitations of Au NPs

Au NPs exhibit strong light absorption in the visible and near-infrared part of the spectrum, which allows their implementation in various types of devices.[151,196] The LSPR peak of Au NPs can be tuned down to 520 nm for the smallest NPs, whereas at shorter wavelengths issues arise that prevent resonance excitation. Interband transitions in Au NPs provide a dissipation channel for the LSPR and the small size of nanoparticles results in large damping of the resonance due to electron-surface collisions.[151,197,198]

Alternative materials for visible light absorption include Ag NPs and Al NPs. Ag NPs have been more extensively investigated and have shown impressive results, with their LSPR tunability reaching 350 nm, enabling their use in applications that require harvesting of shorter visible wavelengths.[166,197] However, Ag NPs suffer from rapid oxidation in oxygen rich environments that is deleterious to their plasmonic properties and thus, severely limits their applicability. As a result, research into the potential of Al NPs as plasmonic materials has emerged, with encouraging outcomes.[197,199] The LSPR peak can be tuned to reach 200 nm, enabling fabrication of devices operating in the UV part of the spectrum, whereas Al is a low cost and abundant material.[197,200] While Al NPs exhibit lower oxidation than Ag NPs, their plasmonic properties are not as well established and understood yet, imparting some uncertainty in their implementation.[201,202]

2.9.4 Plasmonic properties of Au NPs in a magnetic field

Magnetic plasmonic resonances (MPR) refer to excitation of LSPR in Au NPs due to the magnetic component of light, and are correlated with a circulating displacement current, leading to the NPs behaving as a magnetic dipole.[151,203–205] While these resonances are typically very weak or not in the visible part of the spectrum for an isolated NP, they appear intense in NP assemblies, especially rings or shells.[204–206] MPRs have demonstrated enhancement of the oscillating magnetic field, analogous to local electric field enhancement after LSPR excitation.[151,204,206]

In addition, magneto-plasmonic modes on colloidal Au NPs have been observed via magnetic circular dichroism studies, in which the circular plasmonic modes in the Au NPs coupled with the external magnetic field.[207] This result encourages the implementation of magnetic field or light modulation to increase the sensitivity of LSPR to changes in the refractive index of the surrounding medium.

2.10 Magneto-plasmonic coupling

While initial interest on magneto-plasmons and the effects of magnetic field on the dispersion relation of surface plasma and couple surface plasma-phonon waves started in the early 70s, investigation of the interaction of MO properties and surface plasmons could be better achieved with the advent of nanotechnology in recent years.[142,208–210] MO effects are actively studied by theoretical and experimental groups, whereas the recent prominence of plasmonics has led to a surge of research studies on the enhancement of MO effects using plasmon resonances, as well as on the modification of the plasmonic

properties via application of magnetic fields. The combination of these effects is collectively known as magneto-plasmonics and they could be implemented in sensing or telecommunications applications.[142,211–215] The MO constants of ferromagnetic materials are much larger than paramagnetic or diamagnetic materials, while their plasmon resonances are very broad and suffer from significant losses, whereas noble metals show good plasmonic response but are characterized by very small MO constants.[142,216–224] Therefore, magneto-plasmonic heterostructures are typically prepared through combinations of a ferromagnetic material which is responsible for the MO contribution, and a plasmonic material, with Au NPs or thin films being the most prominent choice, in order to leverage the favorable properties of each material.[142]

2.10.1 Modification of MO properties through plasmon resonance

MO effects could be significantly enhanced through excitation of plasmon resonance due to the accompanying local field enhancement in the ferromagnetic component of the heterostructure.[225] As shown in equation 32, the complex Kerr angle can be modified via changes in the pure MO or pure optical contributions to reflectivity. These can be easily altered through excitation of LSPR leading to changes in the MO properties of a heterostructure. For a thin layer of MO material, the pure MO contribution is given by:[142,226–230]

$$|r_{ps}| \propto \langle E_p E_s \rangle d |\varepsilon_{mo}| \tag{38}$$

where $\langle E_p E_s \rangle$ is the mean value of the product of the two components of electric field inside the MO material, d is the thickness of the material, and ε_{mo} is the MO constant. As shown here the value of r_{ps} is proportional to the electric field inside the MO material, and an enhancement of the field due to plasmon resonance excitation would result in a larger complex Kerr rotation.[142] A minimum of pure optical contribution (r_{pp}) to reflectivity can also be achieved through excitation of plasmon resonances, similarly leading to an increase in the complex Kerr rotation.[142] Thus, through either or both of these effects, plasmon resonances have the potential to enhance MO effects.

The studies on the effect of LSPR on MO properties have encompassed various kinds of systems. Initial efforts included ferromagnetic metal NPs, using materials such as Co, Co-Fe, and Ni.[231–236] However, due to aforementioned reasons, combinations of noble metals and ferromagnetic materials have become more popular in recent years. A lot of focus has been on investigations of nanoparticles combining both materials, such as Au/Co/Au nanosandwiches which demonstrated direct correlation between the shift in LSPR peak and complex Kerr rotation values, underlining the plasmonic impact.[142,237] Au coated maghemite nanoparticles have exhibited enhanced Faraday rotation which spectrally matched the LSPR peak, once more indicating the connection between the two.[238] Work on Au nanodisks that were spatially separated by a SiO_2 layer from a Au/Co/Au trilayer has shown that the two materials do not necessarily need to be in contact, and enhancement of the MO properties can still be achieved if the electromagnetic field

from the LSPR reaches the MO material.[142,143] In particular, a certain separation between the plasmonic and MO materials, depending on the materials and geometry involved, can result in stronger MO effects.[239] However, it should be noted that larger area of contact between the two materials, such as nanodisks of larger diameter for instance, has also been observed to result in larger MO enhancement. Furthermore, manipulation of the electromagnetic field due to the LSPR via device engineering can lead to modification of the MO properties observed.[142] Structures that involve plasmonic nanoparticles and dielectric MO continuous layers have also been investigated as the dielectric material can preserve the strong LSPR resonance, whereas ferromagnetic metal films typically suffer from high optical losses.[142,240] Such structures have successfully demonstrated enhanced Faraday rotation spectrally matching the LSPR of the Au NPs.[241–247]

In summary, prior work has made it evident that MO properties can indeed be enhanced through LSPR excitation, in a range of structures and materials, through enhancement of r_{pp}, r_{ps}, or both. Additionally, previous efforts have successfully proved that magneto-plasmonic heterostructures offer some flexibility in their architecture, which is crucial for easy device fabrication. Substantial has been done on demonstrating MO enhancement using materials that support surface plasmon polaritons (SPPs), such as planar interfaces, but this is not the focus of the work done here, and will therefore not be discussed. More information on coupling between SPPs and MO effects can be found in reference [142].

2.10.2 Modification of plasmonic properties through MO effects

While more significant effects have been predicted and observed for heterostructures demonstrating SPPs, the impact of magnetic field and MO effects on materials that exhibit LSPR are more limited. Splitting of the LSPR is predicted in the case of very large magnetic fields, under circularly polarized light excitation, but the effect is not large enough for experimental demonstration.[142,228] Nevertheless, it has also been predicted and demonstrated that the MO material could result in narrower SPR spectrum, which would consequently lead to devices with higher figure-of-merit, which is defined as:[240]

$$Figure - of - merit = \frac{Device\ refractive\ index\ sensitivity, S}{SPR\ full\ width\ at\ half\ maximum, \Gamma} \quad (39)$$

Pure Au-based plasmonic sensors suffer from low figure-of-merit, attributed to high propagation loss of noble metals.[248] Hence, research efforts have attempted to raise this value via material engineering and nanostructuring.[249–251] Important enhancements in these devices were achieved once Au was integrated with MO materials, due to coupling of the SPR with the waveguide mode of the MO materials, leading to long propagation of the SPR and narrower SPR spectrum.[240,252] Moreover, these enhancements were accomplished with considerable flexibility in device architecture, as they were observed over a range of material thicknesses. On the other hand, the intensity of the reflectivity exhibited by the plasmonic nanoparticles is reduced after introduction of the magnetic material.[253]

Magneto-plasmonics have become a prominent area of optics research in recent years due to their promise in revolutionizing sensing and nanophotonic devices such as integrated optical isolators and modulators.[142] Improvements are continuously and rapidly accomplished due to extensive research efforts and are already surpassing equivalent plasmonic devices in performance.

Chapter 3

Experimental techniques

The techniques used to prepare and characterize samples in the work presented in this dissertation are outlined in this chapter. This includes scientific principles, equipment, and procedures involved in each technique. Any variations from the techniques presented here will be specified in subsequent chapters.

3.1 Sample preparation

The samples used in this work include Perovskite thin films prepared with different precursors as will be discussed below, and ZnO nanostructures and microstructures. Other samples include the ZnO single crystal, which was purchased from Tokyo Denpa Inc., as well as hematite nanowires with and without Au NPs at different loadings, which were prepared by Professor Yat Li's group at University of California, Santa Cruz, and will therefore not be discussed in this chapter.

All samples are prepared on indium tin oxide (ITO)-coated glass substrates as they are transparent, and therefore do not interfere with optical measurements, and the ITO coating is conductive, enabling scanning electron microscopy measurements, which will be discussed later in this chapter. The glass substrates are cut from a large substrate into $15\ mm \times 15\ mm$ pieces using a diamond cutter and a metal ruler to ensure straight edges. The size is chosen such that samples can easily fit in the cryostat for low temperature measurements. The conductive side of the glass substrates is identified with a multimeter, and the non-conductive side is marked using the diamond cutter to allow for sample identification during measurements. Once cut, the substrates are washed sequentially in soap, twice deionized water, acetone, and twice in isopropyl alcohol, under sonication, for 20 minutes each. The substrates are then dried in a stream of air and are ready for use.

3.1.1 ZnO nanostructures

The technique used to prepare the ZnO nanostructures was developed and reported by the Lu group.[254] The precursor for the ZnO nanostructure growth is prepared as follows: 8 ml of 1-butanol are combined with 36.45 mg of poly-4-vinyl-pyridine (P4VP) powder, with 19 000 molecular weight, and 7 ml of 1-butanol are combined with 73.2 mg of zinc acetylacetonate powder. The solutions are magnetically stirred at 250 rpm at room temperature for approximately 5 hours until fully dissolved. The zinc acetylacetonate solution is then added dropwise to the P4VP solution while stirring to achieve 15 ml of precursor solution with 0.8:1 metal-to-polymer ratio with 0.3 wt% polymer content. The precursor solution is spin coated on the ITO-coated glass substrates at 3000 rpm for 30 s, followed by drying on a hot plate for 2 minutes at 100 $^{\circ}$C to prevent intermixing of layers. This process is repeated 5 times, drying for 5 minutes after the last layer. When this

procedure is completed the samples are annealed in a furnace for 30 minutes at 350 ˚C, with a 30-minute ramp up period. This removes the P4VP template and leaves zinc precursor particles, which act as nucleation sites for ZnO nanowire growth.

After the substrates have cooled down, solutions for hydrothermal growth of ZnO nanowires are prepared, right before the growth. The solutions include 20 mM of zinc nitrate hexahydrate in deionized water, which corresponds to 190.4 mg of zinc nitrate hexahydrate powder and 16 ml of deionized water, and 20 mM of hexamethylenetetramine (HMTA) in deionized water, which requires 89 mg of HMTA powder and 16 ml of deionized water. The solutions are stirred under sonication and are mixed in a 50 ml autoclave. The substrates with the precursor particles are then placed in the autoclave at an angle, with the active side facing down, as shown in figure 16.

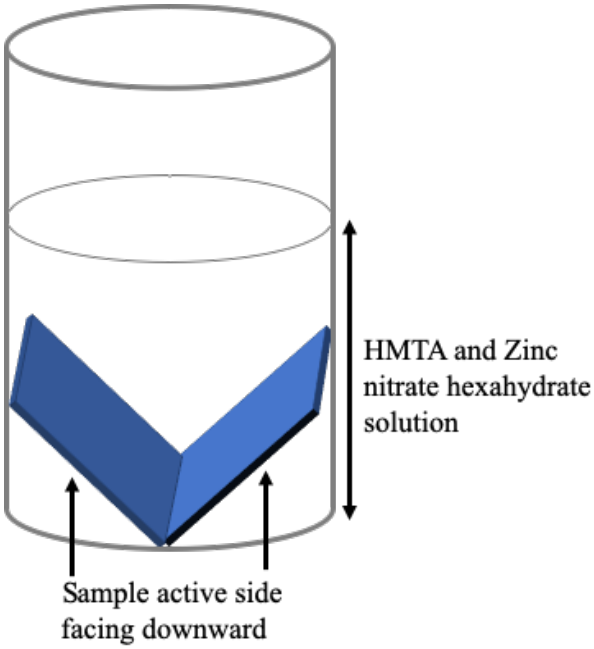

Figure 16. Sample placement in autoclave for hydrothermal growth of ZnO nanowires.

The autoclave is tightly shut and placed in a pre-heated oven at 95 ˚C for 6 hours. At the end of 6 hours, the autoclave is removed from the oven and cooled down under water stream, which reduces pressure in the autoclave and enables removal of the lid. The samples are removed from the autoclave and are rinsed in a beaker with deionized water, and any ZnO deposited on the non-conductive side of the sample is wiped away. The samples are then allowed to dry at room temperature and once they are dry, they are annealed in a furnace at 400 ˚C for 30 minutes, with a 30-minute ramp up period.

3.1.2 ZnO microstructures

ZnO microstructures are prepared using a recipe reported in reference [255], using a three-electrode setup in an oil bath. The active electrode is the sample, the counter electrode is zinc foil, and the reference electrode is Ag/AgCl. The precursor solutions

include 5 mM of zinc chloride in 0.1 M potassium chloride solution in deionized water, with the latter dissolved using vortex stirring. The solutions are added to the electrodeposition cell and the solution is saturated with molecular oxygen, while a slight oxygen bubbling is maintained throughout deposition. The oil bath is set at a temperature of 88 ˚C, and the applied potential is set at -0.82 V, and deposition is done until the total charge exchanged reaches 1.1 C/cm^2 for our samples with area of 2.25 cm^2, which can be converted into time using the current values displayed by the electrodeposition setup and expression 40:

$$t(s) = \frac{charge\ exchanged(\frac{C}{cm^2}) \times area(cm^2)}{I(A)} \quad (40)$$

The samples are then removed from the cell and are rinsed in deionized water and dried under a low stream of air. They are then annealed at 400 ˚C for 30 minutes, with a 30-minute ramp up period.

3.1.3 Perovskite thin films

Perovskite thin film precursors can be prepared using a combination of methylammonium iodide (MAI) and a lead source, with the lead source varying between lead iodide, lead acetate, and lead chloride, resulting in different film properties as will be further discussed in chapters 4 and 5. MAI is purchased from Luminescence Technology Corp. and is purified to ensure good properties. The MAI powder is mixed with 28.5 ml of anhydrous ethanol and 1.5 ml of anhydrous methanol and is sonicated for a few minutes. The mixture is then placed in an oil bath at 60 ˚C and is magnetically stirred at 150 rpm for at least 2 hours, until fully dissolved. The solution is transferred to a beaker and is stirred at room temperature at 180 rpm. 150 ml of diethyl ether are added to the solution which results to re-crystallization of the MAI powder. The mixture is filtered using filter paper, collecting the discarded solution, and washing the collected MAI crystals with diethyl ether. If the discarded solution is yellow in color it indicates that MAI is still present, and the procedure can be repeated on the discarded solution to get more MAI; if all the MAI has been crystallized the solution is clear. The MAI powder is stored in vacuum overnight for drying.

Two types of lead sources are used to prepare the PVSK precursor in this work, lead (II) acetate trihydrate ($PbAc_2$) from Sigma Aldrich, and lead (II) chloride ($PbCl_2$) from Sigma Aldrich. When the former is combined with MAI it leads to the formation of methylammonium lead triiodide ($CH_3NH_3PbI_3$) with I being the only halide, whereas the latter results in mixed halide PVSK ($CH_3NH_3PbI_{3-x}Cl_x$), which contains both I and Cl.[17] Precursor preparation includes dispersion of 2.64 M of MAI in either a single solvent system containing N,N-dimethylformadide, or a bi-solvent system of anhydrous dimethyl sulfoxide and N-methyl-2-pyrrolidione at a ratio 4:6, v/v. The solution is first sonicated for a few minutes and is then magnetically stirred at room temperature in N_2 environment for 30 minutes. Once the MAI is completely dissolved, 0.88 M of lead source is added to the solution, and is then allowed to magnetically stir overnight at room temperature in N_2

environment. The solution is filtered through a polytetrafluoroethylene (PTFE) membrane filter before use.[256,257]

In order to ensure improved coating of substrates, whether that is ITO-coated glass or ZnO structures, the substrates are treated under UV-Ozone for 20 minutes, at room temperature, as this has been observed to enhance hydrophilicity of the substrates. The PVSK precursor solution is spin coated at 4000 rpm for 30 seconds in N_2 environment followed by annealing. Annealing is done either on a hot plate at 110 °C until the sample turns dark brown (5 minutes to 1 hour depending on the precursor) in N_2 environment, or in a vacuum oven at 60 °C for 20 minutes.[2,258]

3.2 Photoluminescence spectroscopy

Optical characterization of materials can be used to extract useful information regarding a semiconductor material, including electronic band gap, free electrons and holes, impurities and defects. Furthermore, optical characterization is crucial in evaluating device performance or interface characterization. Optical characterization techniques are non-invasive and do not require extensive sample preparation, whereas variation of the probing wavelength and power allows for acquisition of different types of information. Among the various optical characterization techniques, photoluminescence spectroscopy has become a routine technique in material and device characterization research.[259]

Absorption of a photon with energy equal or higher than the band gap value excites an electron from the valence to the conduction band to form an exciton (electron-hole pair), when the excited electron returns to the initial state and the electron-hole pair recombines, photoluminescence occurs. The recombination process can be radiative or non-radiative. If the relaxation process is radiative, photoluminescence will be observed, and the emission is characteristic of the material band gap.[259] Recombination is a non-equilibrium process and requires a supply of electrons at an excited state, which is provided by the laser excitation. As the electron-hole pairs have well-defined energies, the emission spectrum is narrow and provides accurate values for band gap and impurity levels. Excitons can recombine via a recombination center, or non-radiatively through the Auger process, or multi-phonon processes due to defect sites.[259]

In the case of a pure semiconductor, the Coulomb attraction results in excitons, whereas the presence of dopants and the associated free charges screen out the Coulomb interaction and reduce the probability of excitons forming. However, if the sample contains impurities free excitons are attracted by Coulomb forces to form bound excitons, with emission of lower energy due to higher binding energy. Furthermore, radiative transitions also occur between impurity levels and conduction or valence bands, as well as donor to acceptor transitions. Therefore, photoluminescence spectra of impure materials are characterized by various peaks corresponding to different types of excitons, and thus photoluminescence is a useful tool in assessing the quality and purity of a material, as well as an effective probe on the recombination processes taking place in a material following photoexcitation.[259]

3.2.1 Steady-state photoluminescence spectroscopy

Steady-state photoluminescence can be conducted at various temperatures, typically from 4 K to 300 K as low temperatures enhance the signal observed by the sample and reduce phonon contributions which can be detrimental to the photoluminescence signal. In addition, photoluminescence measurements can be performed at various excitation powers to observe changes in the intensity of the signal. The experimental setup for steady-state photoluminescence spectroscopy is displayed in figure 17 below.

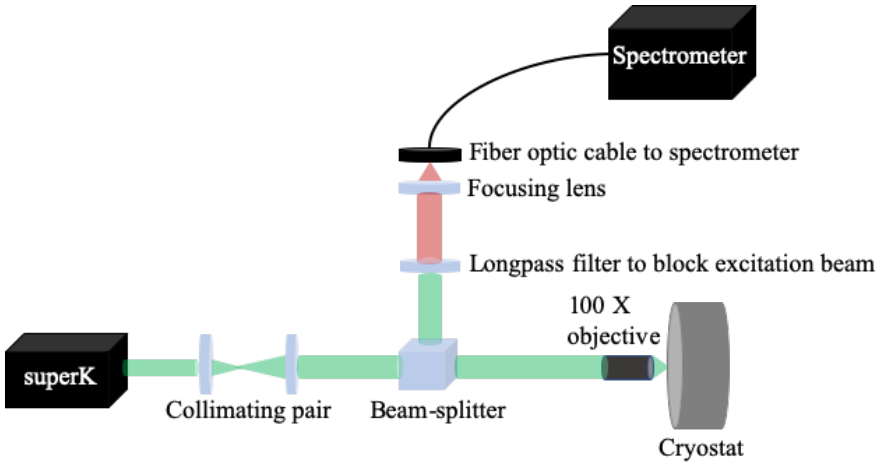

Figure 17. Optical setup for photoluminescence spectroscopy.

The setup shown here uses different types of laser sources: an ultrafast tunable mode-locked laser that provides excitation wavelengths ranging from 350 nm to 1200 nm with repetition rate of 13 ns, or a supercontinuum white light source that allows tuning from 430 nm to 700 nm and variability in the repetition rate. The sample is grown on glass substrate with dimensions of $15mm \times 15mm$ in order to be mounted in the cryo-free system which enables cool down of the samples. The cryogen-free system uses a combination of helium gas to cool down and a heater which controls the temperature setting. The excitation laser is focused on the sample using a 100 X objective to form a ~ 1μm spot. The objective collects the emission of the sample which travels through the beamsplitter to reach the optical fiber that is connected to the spectrometer which is coupled to a thermo-electrically cooled CCD camera that allows spectral analysis.

3.2.2 Scanning photoluminescence spectroscopy

Scanning photoluminescence spectroscopy is used to generate high-resolution photoluminescence map of a sample. This can provide useful information on non-uniformity of the sample, as well as any defects present, through variations in the intensity and wavelength of photoluminescence. The resolution of this measurement is diffraction limited to the wavelength of the laser excitation, typically chosen to be a short wavelength

beam to allow for the highest resolution possible. A schematic of the setup is depicted in figure 18. The setup is mostly identical to the one described in section 3.2.1, except the sample is mounted on a motorized 3D scanning state with step size resolution of 40 nm, which enables raster scanning of the excitation beam across the sample. The spectra collected by the spectrometer at each excitation spot are acquired by a LabView program and the spectra are used to generate maps of photoluminescence intensity and emission wavelength.

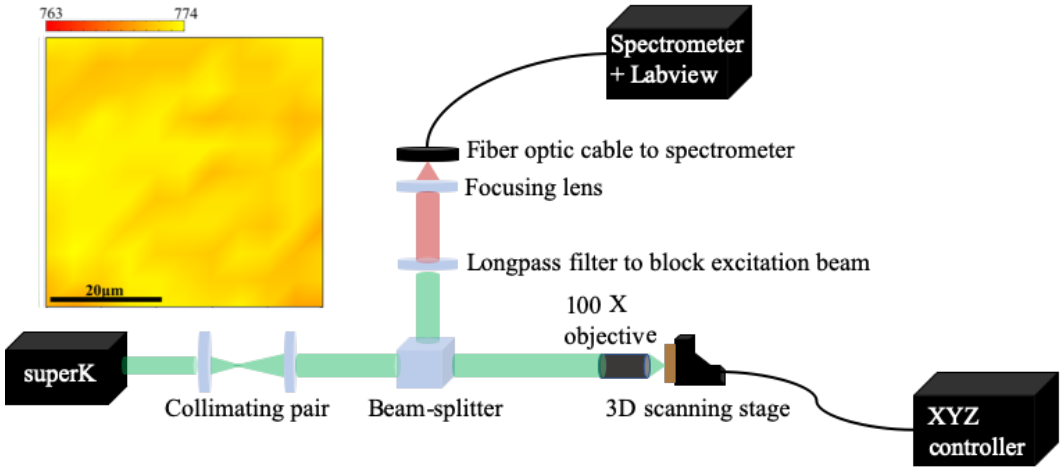

Figure 18. Optical setup for scanning photoluminescence spectroscopy. Map of peak wavelength for a PVSK thin film acquired from this setup is shown.

3.3 Time-correlated single photon counting

Time-correlated single photon counting (TCSPC) is a technique used to obtain the time-dependent profile of light emitted from a sample following excitation and get numerical values for the excited state lifetime of a fluorophore, or electron-hole recombination lifetime in semiconductors. Excitation is achieved with a laser pulse which arrives at the sample periodically, and data collection is done over multiple cycles. The emitted photons are then collected by a single photon avalanche diode (SPAD) and are used to reconstruct the emission decay profile, which appears as a histogram of photon arrivals against time bins.[260] This process is depicted in figure 19 below.

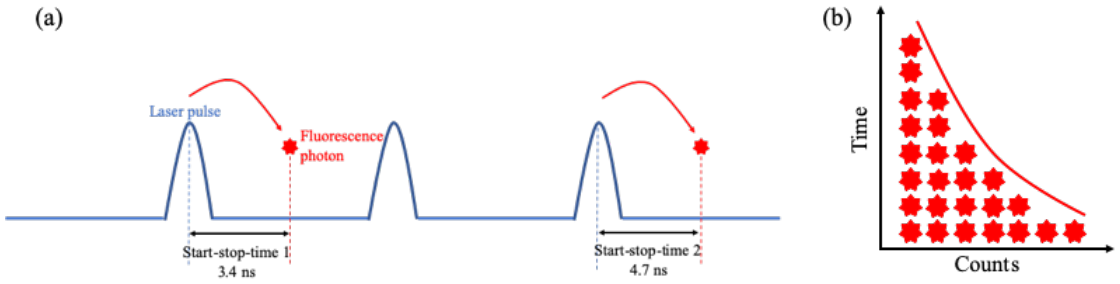

Figure 19. (a) Sample is excited after the laser pulse arrives and emits a photon a certain time later. This process is repeated multiple times. (b) The emitted photons are then used to prepare a histogram depending on the time they were detected. The histogram shows the decay profile which is an exponential decay.

The exponential shape of the emission decay can be explained by considering that each excited molecule has a 50% probability of returning to the ground state after the first nanosecond after excitation, leaving 50% of the population in the excited state. This process is repeated over and over, and as the intensity of emission is given by the number of emitted photons at each time, it is proportional to the population of excited molecules, with all of them reaching ground state when the intensity drops to zero.[260] The measurement is done experimentally by recording the time difference between the excitation pulse and photon emission, with the former being detected via a trigger diode and the latter via the SPAD. However, in the case that there is an electrical synchronization signal supplied by the laser, the trigger diode is not necessary. These signals are then converted into electrical pulses, which allows the fast electronics to perform digital timing which accesses the histogram memory, and once sufficient counts have been recorded, the histogram memory is read out and displayed.[260] The optical setup for this measurement is shown in figure 20.

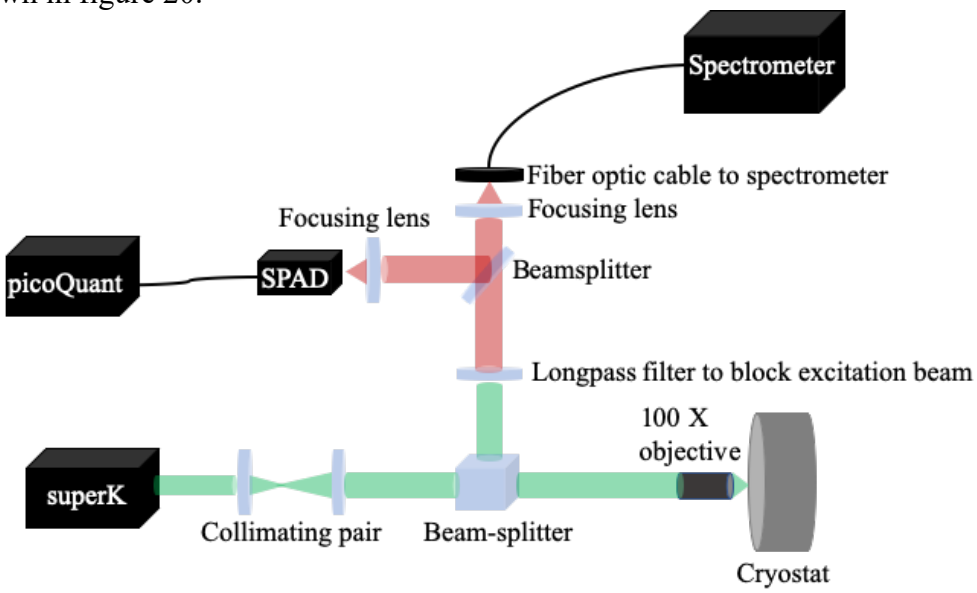

Figure 20. TCSPC setup.

Since the detectors and electronics have a "dead" time after recording a photon, during which another photon cannot be processed, it is necessary to keep the probability of recording more than one photon low, as the TCSPC system is designed to register only one photon per excitation. If this is not done, the system would miss subsequent photons that are emitted by the fluorophore and would result in overestimating the early photons in the histogram, leading to a "pile up". This would ultimately affect the extracted lifetime values from the histogram.

Once the exponential decay histogram is obtained, the recombination lifetime can be estimated by fitting a bi-exponential decay function:[69]

$$I_{PL}(t) = A_1 e^{-t/\tau_1} + A_2 e^{-t/\tau_2} \tag{41}$$

where A_1 and A_2 are fitting constants, t is time, and τ_1 and τ_2 are recombination lifetimes. The average lifetime is then computed by:[69]

$$\tau_{avg} = \frac{A_1 {\tau_1}^2 + A_2 {\tau_2}^2}{A_1 \tau_1 + A_2 \tau_2} \tag{42}$$

Lifetime measurements are a crucial tool in the characterization of any material and interface and therefore, TCSPC is often used for these purposes. This measurement can be performed at room temperature, as well as low temperatures to monitor changes in the recombination lifetime of a material with temperature.

3.4 Ultraviolet-Visible spectroscopy

When light is incident on a material, one of the many procedures that may occur is absorption of light by the sample. The absorbed light results in an increase in the energy of the atoms, and depending on the energy of the photon a transition between electronic energy levels is caused, with the photons providing the additional energy for electrons to move to a higher energy level.[261] Absorption spectra can be used to identify materials, or to gain information on their energy levels.

In the case of ultraviolet-visible (UV/Vis) spectroscopy, the absorption spectrum of a sample is measured through transmittance measurements. Light of known wavelength and intensity (I_0) is incident on the sample and the transmitted light intensity (I) is measured with a detector. Transmittance can be expressed as:[261]

$$T = I/I_0 \tag{43}$$

And Absorbance is estimated by:[261]

$$A = -log\,\frac{I}{I_0} \tag{44}$$

In a UV/Vis spectrophotometer the sample is placed between the light source and the detector and the spectrophotometer performs this measurement, while scanning over different excitation wavelengths, ranging from near-infrared to UV, and estimates the absorbance at each wavelength. This is depicted in figure 21. One important limitation of this equipment is the inability to distinguish between absorbed or reflected light, which could be achieved using an integrating sphere.

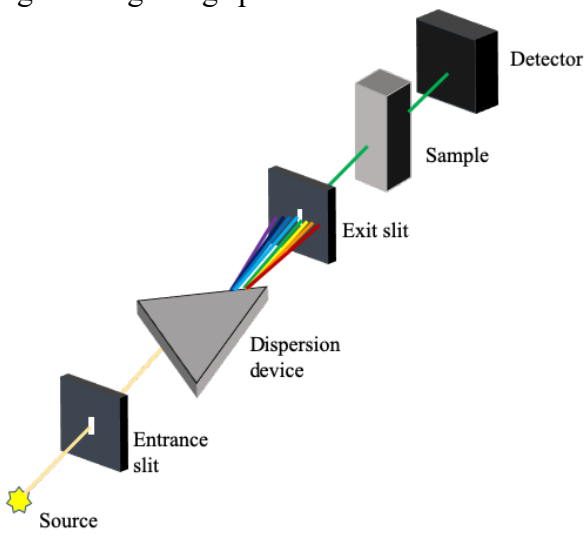

Figure 21. The setup of a typical UV/Vis spectrophotometer.

3.5 Confocal microscopy

Excitation of atoms via light absorption is often followed by atoms emitting photons with lower energy as a means of relaxing back to the ground state. This emission can be detected using a fluorescence microscope and it provides an image of the emission or fluorescence of a sample at various locations, which can be used to extract valuable sample information.

A confocal microscope allows acquisition of fluorescence images with certain benefits over a conventional fluorescence microscope, such as the ability to obtain serial optical sections from thick samples to form three-dimensional images, eliminating any out of focus glare, and allowing shallow depth of field.[262] In a conventional microscope, fluorescence from a different region of the sample interferes with the fluorescence of the region of interest resulting in low resolution of features, with the problem becoming significant for samples thicker than 2 μm. However, in a confocal microscope, the out-of-focus fluorescence can be excluded from the image, as shown in figure 22. This is achieved by incorporating a pinhole at the image side of the setup, which only allows the desired light rays to pass through to the detector, whereas the rest is blocked. This pinhole is the size of an Airy disk, in order to prevent losing useful emission. Furthermore, while in a conventional microscope light illuminates the entire sample and the image is projected onto the image capture device, meaning that the entire sample is fluorescing, in a confocal microscope illumination is done by scanning a focused laser beam across the sample, which further reduces background contributions to the fluorescence image.[262,263]

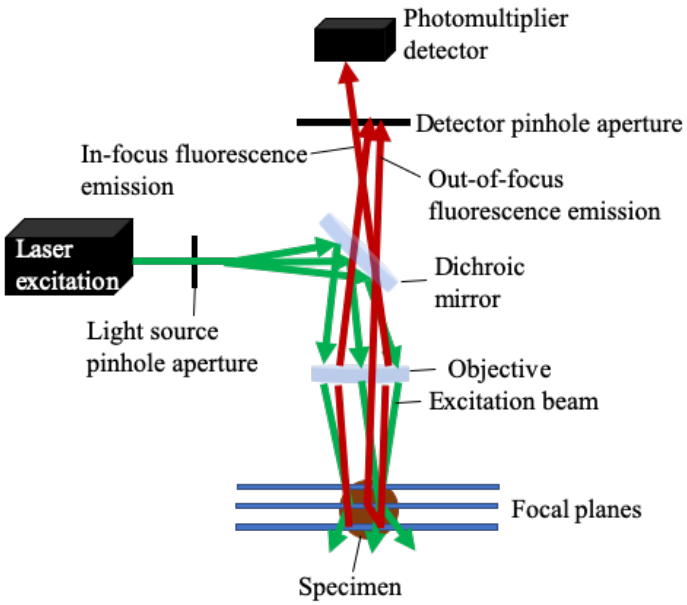

Figure 22. Light beam path in a confocal microscope.

In more detail, laser light is used to excite the sample, and is reflected by a dichroic mirror and directed towards the sample. The laser beam reaches two mirrors which are used to scan the beam across the sample. The sample emission is then descanned by these mirrors, it is transmitted through the dichroic mirror, and is focused on the pinhole, with the emission passing through the pinhole being detected by a photomultiplier tube. Since one point of the sample is observed at a time, the detector and the attached computer build the image. [262,263] Not only does the confocal microscope block emission from other focal planes in the sample, but it also blocks emission from areas in the focal plane but not at the focal point, therefore enhancing vertical and lateral resolution.[262,263]

Confocal microscopy is performed on PVSK thin film samples deposited on various ZnO substrates in order to observe emission from grains and any dark regions that may appear. Samples are grown on ITO glass and no further treatment is necessary for this procedure.

3.6 Field emission scanning electron microscopy (FE-SEM)

Scanning electron microscopy (SEM) is a type of microscopy that can be used to extract topographical and elemental information about a sample at much higher resolution than that of an optical microscope, due to the use of electrons for imaging instead of photons, which possess a much smaller wavelength. Magnification can reach 100000X. Its operation is based on a focused electron beam which scans the sample surface and results in secondary electrons, backscattered electrons, and characteristic X-rays, which are collected by different detectors to form images of the sample that are displayed on a screen.[264,265] Secondary electrons are a result of inelastic interactions between the

incoming electrons and the sample, and are used for observations of the topography of the sample.[266] Backscatter electrons are due to elastic collisions of the incident electrons with the atoms in the sample and since the number of backscatter electron increases with the atomic number of the element, they can be used to extract elemental information of the sample, as well as topography information.[266]

Field emission SEM (FE-SEM) provides higher quality images than a conventional SEM, reaching magnifications of 2000000X, and three to six times higher spatial resolution (down to 1.5 nm).[264,267] In addition, low-voltage is used which allows for easier imaging of semiconductors or insulating materials which are prone to electron charging. Top-down and cross-sectional FE-SEM imaging is performed on PVSK thin films grown on ZnO substrates of various morphologies. Top-down SEM imaging is used to observe uniformity, smoothness, grain sizes, or grain separation in PVSK thin films and any changes depending on the substrate. For this purpose, samples must be grown on ITO glass as this provides a pathway for electrons to leave the sample to prevent electron accumulation (referred to as "charging"), as this does not allow acquisition of good images due to incoming beam deflection by the accumulated electrons. The samples on ITO glass are anchored to a flat aluminum stub via conductive carbon tape, both of which assist with electron extraction. Images are then acquired using the in-lens detector, which collects the secondary electrons that originate from the surface of the sample, at a voltage of 0.5 kV to prevent rapid charging of the semiconducting samples.[266] As for cross-sectional SEM, samples are cut using a diamond cutter and the exposed cross-section is imaged. Different aluminum stubs are used for this type of imaging which allow vertical anchoring of the sample, which is achieved via carbon tape – with the active side of the sample facing the aluminum stub – and silver paint on the sides of the sample to enhance adhesion to the aluminum stub. Cross-sectional SEM is more likely to result in charging of the sample, hence why it is necessary to provide multiple pathways for electron extraction from the sample. Secondary electrons are used to observe the cross-section of the sample, and thus the in-lens detector is used. As the area imaged in this case is much smaller – most the sample is now the glass substrate – higher voltage is required to increase the signal for good images. Therefore, voltage values from 3 V to 10 V are used to obtain these images. Cross-sectional SEM is a very useful tool in interface characterization as it provides an image of the interface and shows how good the contact between materials is, or if the interface has detrimental effects on the PVSK thin film.

3.7 Magneto-optical Kerr effect spectroscopy

As discussed in section 2.7, MOKE refers to changes in the polarization of incident plane polarized light upon reflection from a magnetic material. Figure 12 demonstrated the various configurations to observe MOKE, and in this section focus is given to polar MOKE spectroscopy, as it is used to investigate changes in polarization of incident s-polarized light after it is reflected from hematite nanowires, with and without Au NPs on their surface. The setup for this measurement is depicted in figure 23.

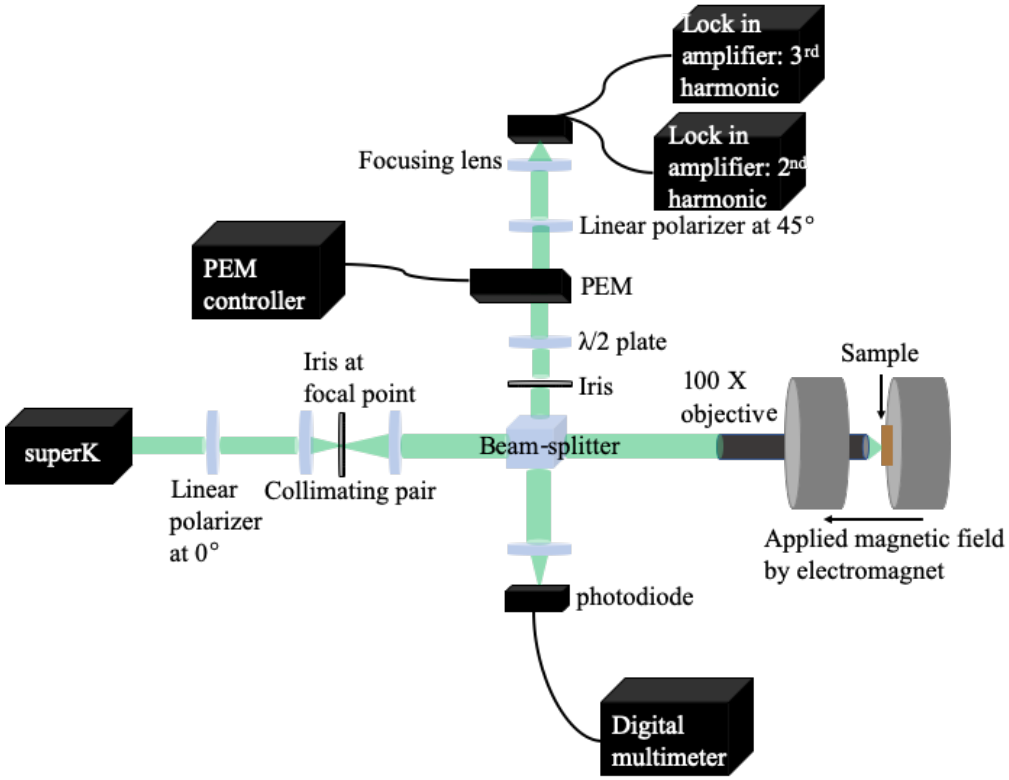

Figure 23. Experimental setup for polar MOKE spectroscopy. In this geometry, light is at normal incidence to the sample, which is magnetized perpendicular to its surface. In polar MOKE, Kerr rotation and ellipticity are proportional to the magnetization of the sample.

MOKE results in Kerr rotation (θ_{Kerr}) and Kerr ellipticity (φ_{Kerr}), therefore both components are investigated using spectroscopic measurements. In order to achieve this experimentally, the complex Kerr angle (ϕ_{Kerr}) is expressed in terms of the complex refractive index for the LCP ($\tilde{n}_+$) and RCP ($\tilde{n}_-$) components of the linearly polarized light, where $\widetilde{n_\pm} = n_\pm + ik_\pm$, as shown in equation 45:[268]

$$\phi_{Kerr} = \frac{2i(\widetilde{n_-} - \widetilde{n_+})}{1-\varepsilon} = \frac{2}{1-\varepsilon}[-(k_- - k_+) + i(n_- - n_+)] \tag{45}$$

From this expression, it can be deduced that Kerr rotation ($\mathrm{Re}(\phi_{Kerr})$) is proportional to circular dichroism given by $(k_- - k_+)$, whereas Kerr ellipticity ($\mathrm{Im}(\phi_{Kerr})$) is proportional to circular birefringence, given by $(n_- - n_+)$, assuming that the imaginary component of ε is small compared to 1. This provides a route to measuring Kerr rotation and ellipticity experimentally.

This is achieved via a photoelastic modulator (PEM), as the light reflected from the sample travels through the PEM, which allows determination of light polarization. The PEM is made of an optically isotropic crystal and two piezoelectric transducers which provide stress alternations at a resonant frequency (ω_{PEM}) of 50 kHz. This results in large changes in strain in the horizontal direction, and consequently, large changes in the refractive index in the x-direction:[268]

$$n_x(t) = n_0 + \Delta n \times \sin(\omega_{PEM} t) \quad (46)$$

where n_0 is the unstrained refractive index and Δn is the resultant difference in refractive index. The refractive index in the y-direction remains equal to n_0. Due to this time-dependent variation of refractive index in one direction, the x-component of the electric field experiences a periodical phase retardation $\delta(t)$ with respect to the y-component, given by:[268]

$$\delta(t) = \beta \cos(\omega_{PEM} t) \quad (47)$$

where β is the phase modulation amplitude, or retardance, and can be expressed as:

$$\beta = 2\pi \frac{\Delta L}{\lambda} = 2\pi \frac{\Delta n D}{\lambda} \quad (48)$$

In expression 48, ΔL is the optical path difference between the two components of light due to the refractive index difference, D is the PEM crystal thickness, and λ is the wavelength of light. Since the optical axis of the PEM is parallel to the y-component of light, modulation only happens if the sample results in variations in the x-component of polarization due to Kerr rotation or ellipticity.[268] The PEM undergoes a calibration procedure, which helps determine the retardance setting for the setup and wavelength used. In brief, the PEM is set at 45° between two crossed polarizations, which block any light from reaching the detector if the retardance is zero. When the retardance is close to half-wave, the transmitted light intensity at a maximum, and minor adjustments can be made to reduce the sensitivity of the transmission signal to alignment of the setup.

When light emerges from the PEM, the component of the incident electric field ($\boldsymbol{E_0}$) along the y-axis of the PEM experiences a phase shift, meaning that the transmitted electric field ($\boldsymbol{E_1}$) is given by:[268]

$$\boldsymbol{E_1} = (E_0 cos45)\hat{x} - \left(E_0 e^{i\delta(t)} sin45\right)\hat{y} = E_0 \frac{\sqrt{2}}{2}(\hat{x} - e^{i\delta(t)}\hat{y}) \quad (49)$$

The field $\boldsymbol{E_1}$ then travels through the polarizer, which results in the field $\boldsymbol{E_2}$ to be transmitted through, with magnitude:

$$E_2 = E_0 \frac{\sqrt{2}}{2}(1 - e^{i\delta(t)}) \quad (50)$$

Therefore, the intensity of the light reaching the detector is:

$$I_2 = \frac{1}{2} c\varepsilon_0 |E_2^2| = I_0(1 - 1\cos[\beta \cos(\omega_{PEM} t)]) \quad (51)$$

In this formula, the last term can be expressed in terms of the even harmonics of ω_{PEM}:

$$\cos[\beta \cos(\omega_{PEM} t)] = J_0(\beta) + 2J_2(\beta)\cos(2\omega_{PEM} t) + 2J_4(\beta)\cos(4\omega_{PEM} t) + \cdots \quad (52)$$

where J_n represent the n^{th} order Bessel functions.

The signal reaching the detector can be correlated to the complex Kerr angle as:[268]

$$Re(\phi_{Kerr}) = \frac{1}{4J_2(\beta)} \frac{I_{2\omega_{PEM}}}{I_0} \propto I_{2\omega_{PEM}} \quad (53)$$

$$Im(\phi_{Kerr}) = \frac{1}{4J_3(\beta)} \frac{I_{3\omega_{PEM}}}{I_0} \propto I_{3\omega_{PEM}} \quad (54)$$

where $I_{n\omega_{PEM}}$ represents the signal intensity at the nth harmonic of ω_{PEM}, and I_0 is the signal intensity at the frequency of ω_{PEM}, which is proportional to laser power. As seen from equations 53 and 54, Kerr rotation is associated with the even harmonics, and Kerr ellipticity is associated with odd harmonics. The frequency components are measured using two lock-in amplifiers, one corresponding to each harmonic, which are connected to the detector indicated in figure 23. The lock-in amplifiers modulate the small signals detected at frequency ω_{PEM} and are connected to a LabView program which reads these values at various applied magnetic fields. Magnetic field is applied perpendicular to the sample, via an electromagnet, with currents varying from 0 to 3 A. The current of the magnet is converted to applied field using the following empirical expression:

$$H_{applied}(G) = 13.14398 - 1238.76968I - 0.30105I^2 + 2.57253I^3 + 0.04771I^4 \quad (55)$$

where I represents the electromagnet current in Amperes. Expression 55 describes the magnetic field in the case of two poles present, but since for polar MOKE one of the poles is removed, finite element analysis was performed to obtain the field with a single pole, to an accuracy of 1 %.

The LabView program generates curves of Kerr rotation and ellipticity as a function of applied magnetic field. For wavelength dependent measurements, the PEM settings are changed accordingly and Kerr rotation and ellipticity values are recorded at maximum field, since values are expected to be maximized.

Chapter 4

Hybrid Perovskite Thin Films as Highly Efficient Luminescent Solar Concentrators

This chapter studies the viability of PVSK thin films as the active medium in planar LSCs. The study involves spectroscopic and photovoltaic measurements to investigate variation of optical stability and device performance for PVSK thin films prepared with precursors possessing different lead sources. Even though the devices show high self-absorption losses, they exhibit high optical efficiency, ranging from 15 % to 29 %, and remain operational after seven weeks in ambient conditions. These findings are supported by Monte Carlo simulations, and the outstanding performance is attributed to the high quantum yield and refractive index of PVSKs. Therefore, the results of this study are encouraging the implementation of PVSK thin films as LSCs, but also the preparation of tandem devices which would capture energy escaping as radiative exciton recombination in PVSK solar cells.

4.1 Introduction

Luminescent solar concentrators, proposed as alternatives to solar cells in the 1970s, typically consist of high refractive index substrates doped with photoluminescent materials that absorb both direct and diffuse sunlight. The resultant down-converted emission is then conveyed to the edges of the device by total internal reflection, to be captured by attached solar cells.[71–73] As the lateral surface area of an LSC is considerably larger than its edge area, the photon density incident on the solar cells is increased, named the “concentrator” effect. Additionally, by a propitious choice of the dopants, the emission can be spectrally-matched to the solar cell bandgap, further optimizing the generated photocurrent.[74] The initial motivation for LSCs had been financial, as large panels of glass or polymer materials were far less expensive than an equivalent sized solar panel.[75] With time, this aspect has been considerably negated, but LSCs remain of interest on account of other advantages they offer over conventional photovoltaics. One of these is the simplicity of fabrication compared to the multistep, and often rigorous, procedures involved in solar cell development. Other benefits include operation under both diffuse and direct lighting, which make tracking machinery and focusing optics unnecessary, and allow for mounting on vertical surfaces, greatly enhancing the deployable area, particularly in crowded urban landscapes.[71,75,269]

The characteristics of a desirable LSC candidate include high QY, large Stokes shift to minimize self-absorption, and broad spectral absorption range to collect as much sunlight as possible. The earliest materials used in LSCs were fluorescent organic dyes, followed by laser dyes,[71] both chosen for their high QYs. Optical efficiency of 40 % has been achieved using a mixture of Lumogen F Red 305 dye in polymer, and power conversion efficiency of 7.1 % has been reported using a combination of dyes with GaAs solar cells attached at the edges.[270,271] Higher power conversion efficiency of 14.5 % has been achieved using a tandem planar solar concentrator, employing a mixture of dyes in combination with copper indium gallium selenide cells.[272] Dyes have inherent problems that include rapid photobleaching and narrow absorption bands,[273–275] and while there are some, such as Red305 by BASF that demonstrate long lifetimes and broad absorption spectra,[276,277] these are the exception rather than the rule. Consequently, the efforts to develop stable and high performing LSC active materials shifted to semiconducting quantum dots (QDs). QDs have broadband absorption extending from the band edge into the ultraviolet, and although the most commonly used QDs emit in the visible region,[278] there have been LSCs developed using QDs with narrow bandgaps emitting in the near infrared that are better spectrally-matched to silicon.[74] "Giant" QDs designed to eliminate "blinking" and photo-degradation have emerged as yet another possible LSC candidate.[279] A recent development incorporating nontoxic QDs with high QY and a 150 nm Stokes shift has achieved optical efficiency of 26.5 %, bringing LSCs one step closer to utilization in large area building integrated applications.[280–282] In addition to progress on the materials engineering front, there have been research efforts on modifying the standard planar architecture with other geometries, such as cylinders, where reduced self-absorption and increased scattering have enhanced device efficiency.[283]

Despite the progress outlined above, LSCs have not replaced traditional solar cells. While QD-based LSCs are an improvement over their dye-based counterparts, they also oxidize and degrade with time,[281,284] which is particularly severe for the near infrared emitting QDs. Additionally, most have low QY and have not demonstrated power conversion efficiencies above 9 %.[71,74,272,285] In this paper, we move away from discrete fluorescent dopants, and examine the viability of continuous thin films of PVSK as the active medium in planar LSCs. Hybrid PVSKs have dominated the photovoltaic field in the past few years as solution-processed high efficiency solar cells,[286] combining the ease of fabrication of organic materials with the high carrier mobility of inorganic semiconductors.[3] Typically, opaque thin films would not be ideal for LSCs due to high self-absorption, but PVSK materials have several advantages that could compensate for this aspect. These include an absorption band that spans a large portion of the solar spectrum, a high QY often reaching 80 %[3,18] and a refractive index of 2.5, significantly larger than glass and polymer films, indicating the likelihood of more efficient confinement.[287,288] In a prior instance, PVSK films were used to coat a silicon solar cell to exploit the superior absorption and QY to improve the solar cell performance.[289] In our case, hybrid PVSK thin films are used in the traditional LSC configuration with silicon PV cells attached at the edges, and we focus on two main aspects in our study. The first is optimizing LSC performance with PVSK composition and film quality, achieved by varying the ratio of precursors during the synthesis stage. The second is investigating an issue that is a big hurdle to the deployment of PVSK photovoltaics in the field—the

structural instability that causes rapid deterioration of film quality and electronic transport properties when exposed to humidity.[290,291]

Our results reveal high optical efficiency (15 %–29 %), which we find to be strongly dependent on the sample preparation process, and we correlate device performance to optical quality by spatially-resolved photoluminescence (PL) spectroscopy, and to structural integrity via SEM. Additionally, our LSCs remain operational after seven weeks under ambient conditions, far longer than expected for a hybrid PVSK sample.

4.2 Results

4.2.1 Spectral and morphological characterization

Figure 24 summarizes the spectral properties of a characteristic PVSK thin film with 50 % $PbAc_2$ content. The emission is centered at 780 nm with a full width at half maxima (FWHM) of 40 nm. The absorption, uncharacteristically for 3D systems, spans the entire visible spectrum and extending into the near infrared. In traditional dye or QD doped LSCs, quality of surface emission is not an important indicator of device performance; edge emission is the critical parameter. For thin film PVSKs fabricated by solution-based processing techniques, however, surface emission uniformity is a reflection of sample crystallinity and structural homogeneity, and has become a necessary measurement for characterizing film quality on a length scale larger than what is possible using electron microscopy.[17,256] Spatial uniformity of spectral intensity and wavelength should reflect the lack of defects that serve as nonradiative recombination centers, which in turn could hinder LSC photocurrent output.[12,257] In the inset we plot the peak wavelength λ_P of a spatially resolved PL scan over a 50 μm^2 area. The variation is ≈10 nm, well within the FWHM of the emission, and signifies that our samples are spectrally homogenous and associated self-absorption losses will be as well.

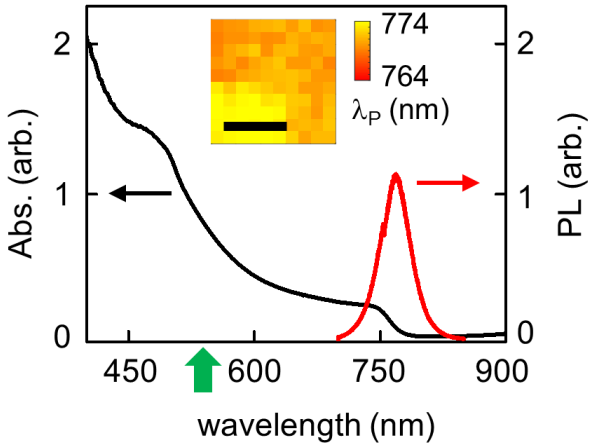

Figure 24. Absorption and PL emission spectra of PVSK thin film. Bold arrow shows laser excitation wavelength. (Inset) Spatially-resolved peak emission wavelength λ_P map. Scale bar is 25 μm. Reproduced from [1] with permission. © WILEY-VCH Verlag GmbH & Co. KGaA, Weinheim

The use of $PbAc_2$ precursor has been previously shown to form highly uniform PVSK thin films due to the volatile nature of the byproduct, whereas the longer annealing time required for $PbCl_2$ based PVSKs, which may produce larger crystals favorable for charge carrier transport, are prone to pore formation prior to crystallization.[292] In figure 25 we systematically correlate the stoichiometric ratio between Pb precursors and the corresponding optical quality and morphology of the thin films. As shown in the SEM images of the PVSK films in figure 25a–d, films with 100 % $PbAc_2$ are characterized by lack of pinholes and ultrasmooth surface, while increasing stoichiometric ratio of $PbCl_2$ leads to the formation of larger grains and abundant pinholes. The high density of pinholes has been associated with increased nonradiative recombination. The accompanying PL intensity maps show an interesting correlation between structural and optical qualities: the smooth 100 % $PbAc_2$ film has PL emission that is expectedly very uniform, but of low intensity; the films with 95 % and 90 % acetate content have brighter but highly inhomogeneous PL; the 50 % $PbAc_2$ sample appears to have the most homogenous PL emission that is also of high intensity. Based on these observations, an LSC with either 50 % or 100 % $PbAc_2$ would appear to have potential for most success.

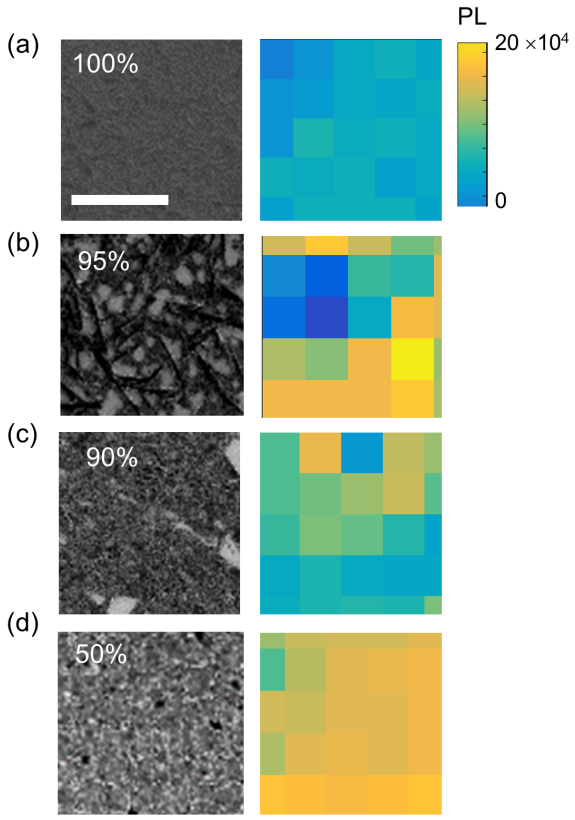

Figure 25. SEM images of samples with varying $PbAc_2$ content, along with spatially-resolved PL maps. a–d) 100 %, 95 %, 90 %, and 50 % acetate content, respectively. All images are 25 μm^2. Reproduced from [1] with permission. © WILEY-VCH Verlag GmbH & Co. KGaA, Weinheim

We additionally demonstrate in figure 26 that the 50 % $PbAc_2$ sample has the highest external quantum efficiency (EQE), which is expected given that higher Cl content improves electronic properties.

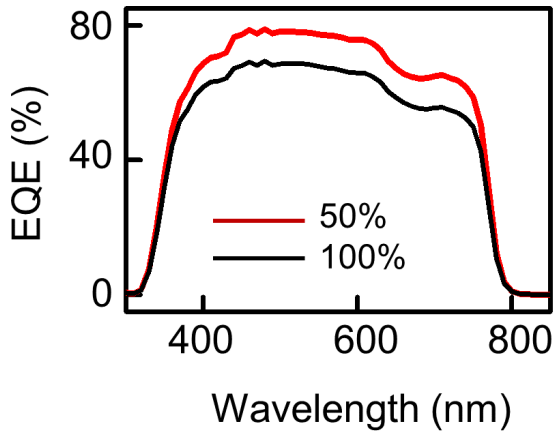

Figure 26. External quantum efficiency (EQE) varying with $PbAc_2$ content. Reproduced from [1] with permission. © WILEY-VCH Verlag GmbH & Co. KGaA, Weinheim

4.2.2 Estimating self-absorption and surface losses

In addition to structural integrity and optical homogeneity, LSC active materials should aim to minimize self-absorption (SA) losses that arise from reabsorption of the light emitted by the active material itself along the optical path to the edges. SA is accompanied by a red-shift in emission wavelength as the more energetic photons are reabsorbed and subsequently re-emitted at lower energy (longer wavelength). To quantify SA, we use PL measurements in figure 27 with excitation and collection spatially separated by a distance d. The excitation spot is ≈1 μm, and the emission is collected using a fiber optic at the edge of the device. Figure 27a,b summarize the results obtained using 532 nm laser excitation and shows PL intensity and peak wavelength red-shift ($\Delta\lambda_P$) as a function of d, data taken four weeks apart. The maximum value of d is 12 mm, limited by the size of the samples. PL intensity taken as soon as the samples are prepared decreases by 90 % with increasing d but $\Delta\lambda_P$ only shifts by 3 nm over the same length. Such small red-shift is indicative of minor SA by the PVSK film, which implies the accompanying intensity drop is most likely due to top/bottom surface losses. Data re-taken after the samples are exposed to ambient conditions for four weeks do not show significant change in $\Delta\lambda_P$, and PL intensity now drops by 75 %. This is an encouraging result as it indicates that despite the instability of PVSK in photovoltaic applications, the optical properties are far more stable and will thus enable more viable alternative applications. To gain a more realistic picture of the SA losses, we repeat the measurements with a broadband white light source in figure 27c,d. In this case, PL intensity decreases more rapidly than in figure 27a, and $\Delta\lambda_P$ is much larger, measuring 15 nm over the same range of d. Large SA is expected in a continuous film, but it is significant that SA is higher with white light in comparison to illumination by

monochromatic light. This may be attributed to the differential absorption of PVSKs over the spectral range of the broadband source, which results in the production of fewer photo-generated carriers on average compared to excitation by 532 nm.[293,294]

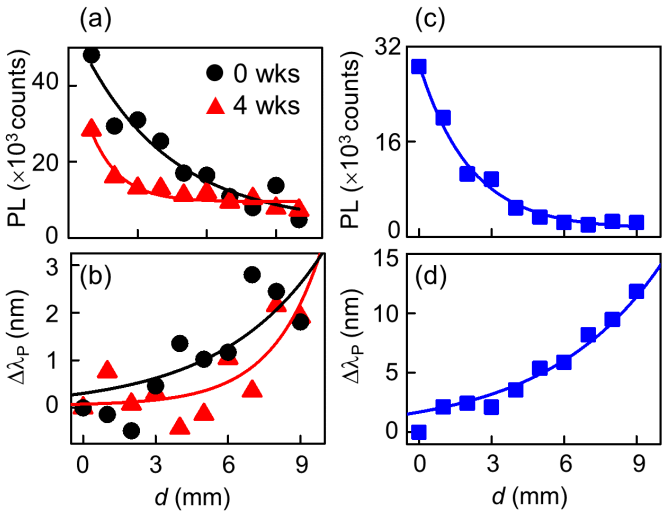

Figure 27. a) PL and b) peak wavelength shift $\Delta\lambda_P$ varying with pump probe separation d measured using laser excitation. c) PL and d) $\Delta\lambda_P$ measured with broadband white light excitation. Reproduced from [1] with permission. © WILEY-VCH Verlag GmbH & Co. KGaA, Weinheim

To accurately estimate both SA and surface losses that would be associated with our samples when exposed to the solar spectrum, we perform 3D Monte Carlo simulations for three different types of LSCs, which include (i) thin film PVSK with refractive index 2.5, and QY = 0.8, (ii) PVSK QDs embedded in a substrate with refractive index 1.7, and QY = 0.8, and (iii) CdSe/CdTe core-shell QDs embedded in a substrate with refractive index 1.7, and QY = 0.9. The substrate refractive index used is 1.7 instead of the more common 1.5 to mimic our indium tin oxide (ITO) coated glass substrates. We note here however, that we have repeated simulations of (ii) and (iii) with a refractive index of 1.5 and the results are practically unchanged. CdSe/CdTe QDs typify dots emitting in the visible spectrum used in LSCs. We include PVSK QDs in our calculations as they share the high QY of their thin film counterparts and may have lower SA. Figure 28 summarizes the results. Figure 28a shows histograms representing the number of absorption events that each photon undergoes in all three materials. Ideally, each photon should undergo a single absorption event and then be re-emitted to propagate up to the edges. If that were the case, the second column from the left (labeled "1") would have 100 % of the photon counts. In the thin film PVSK sample more than 40 % of the incident photons undergo a single absorption and re-emission event, with less than 20 % of the incident photons not being absorbed at all, and even fewer undergoing multiple absorption (self-absorption) events, attesting to efficient absorption and adequate Stokes shift. The histogram using the PVSK QDs is comparable to the thin film. In contrast, the CdSe/CdTe QDs results in most of the photons (> 50 %) not being absorbed at all, and only 15 % being absorbed exactly once, which is quite wasteful. In figure 28b we compile the proportions of photons that are lost

through the surfaces, that are not re-emitted, and that are ultimately collected. For the two LSCs based on PVSK, ≈40 % of the incident photons are collected, compared to only 9 % in CdSe/CdTe LSCs. To obtain a meaningful comparison, the optimal QD concentrations for maximal optical gain were used, which corresponds to volume fractions of 10^{-4} and 10^{-3} for the PVSK and CdSe/CdTe QDs, respectively. Even though the PVSK QY was below that of CdSe/CdTe QDs, the results using the PVSK QDs are better because its larger Stokes shift allows for a tenfold higher concentration. In all these simulations we have assumed a mirror coated bottom surface and silicon PV cells on all four sides. The PVSK simulations used the experimental absorption and PL data reported here and the CdSe/CdTe simulations used measured optical properties in prior work.[295] The sunlight is incident normal to the surface and its spectrum is sampled from the solar irradiance.[296] Further details on the Monte Carlo method used can be found in references [295,297]. We calculate the amount of collected and escaped photons as a function of PVSK film thickness in figure 28c. For the thickness of our samples, ≈400 nm, 60 % of the incident photons are collected. Higher thickness, as these results indicate, could improve light absorption. However, figure 28d shows that while increased film thickness does lead to better absorption, with the highest percent of single absorption events, it also has higher proportion of subsequent absorption counts. This implies increased thickness is also associated with greater self-absorption, thereby negating the initial benefit of enhanced light absorption.

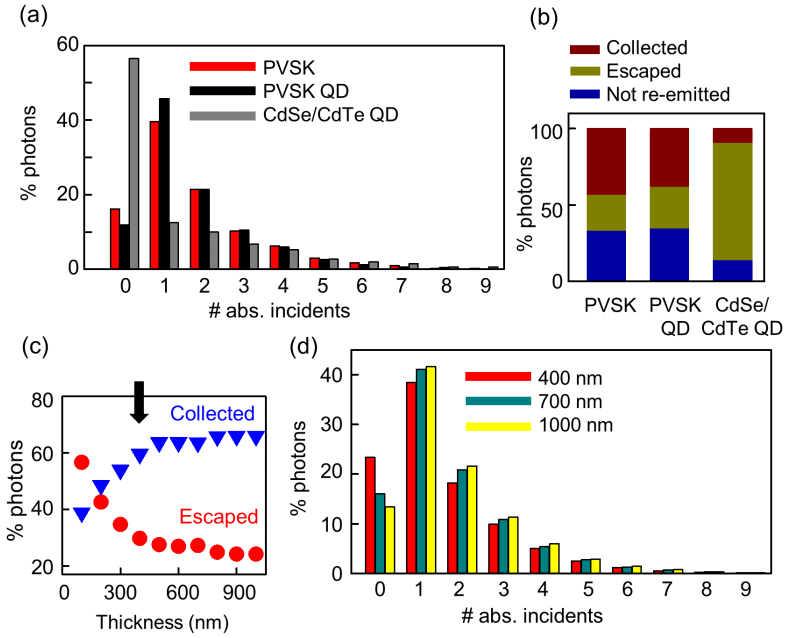

Figure 28. a) Calculated distribution of reabsorption events of absorbed photons for different LSC materials. b) Relative proportions of photons collected, escaped and not re-emitted. c) Photon collection and escape percentages varying with PVSK thin film thickness. Arrow indicates thickness of thin films used in the experiment. Note: these are deposited on a 1 mm glass substrate. d) Absorption events varying with PVSK film thickness. Reproduced from [1] with permission. © WILEY-VCH Verlag GmbH & Co. KGaA, Weinheim

4.2.3 Optical efficiency and device stability

In figure 29 we monitor the effect of the ratio of $PbAc_2$ to $PbCl_2$ in the PVSK precursor solution on absorption, SA, and LSC-to-PV current ratio. As shown in figure 29a, SA, directly proportional to the measured spectral red-shift $\Delta\lambda_P$, increases almost monotonically with acetate content, while absorption, shown in figure 29b, starts increasing around $PbAc_2$ content of 80 %, peaking at 98 %. Figure 29c shows the current generated by each of these. In the low $PbAc_2$ regime (50 % acetate), as the uniform PL scan in figure 25d indicated, SA is low, but unfortunately so is the total absorption, resulting in low total I_{LSC}. With 100 % acetate, PL scan in figure 25a had been homogenous but of low intensity, and here it exhibits high SA cancelling the advantage of high absorptance. The highest current is observed in the PVSK sample with 90 % $PbAc_2$ and these results indicate the SEM images and PL scans do not accurately predict photocurrent generation ability, and neither does EQE data. As with other LSC materials the ratio of absorption to SA is the most critical factor.

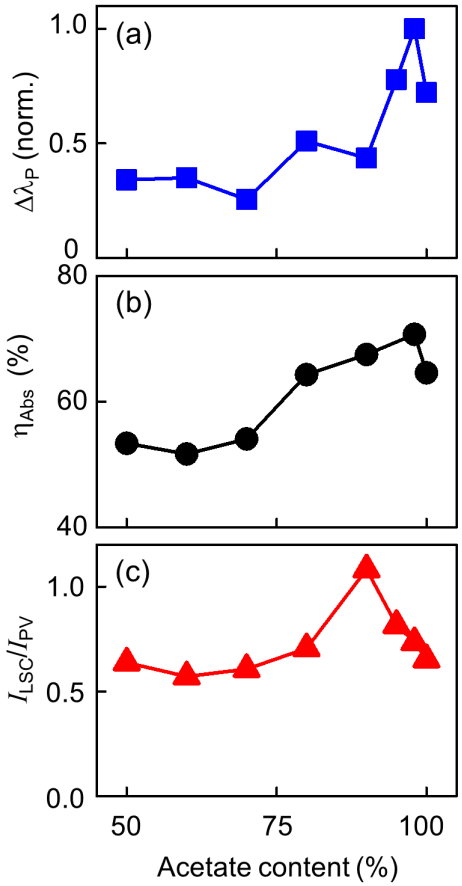

Figure 29. a) $\Delta\lambda_P$, b) η_{Abs}, and c) current ratio I_{LSC}/I_{PV} varying with $PbAc_2$ content. Reproduced from [1] with permission. © WILEY-VCH Verlag GmbH & Co. KGaA, Weinheim

Using the current I_{LSC} we can calculate the optical efficiency using:[75]

$$\eta_{opt} = \frac{I_{LSC} \times A_{PV}}{I_{PV} \times A_{LSC}} \tag{56}$$

The concentration factor is defined as the ratio of the areas of the LSC and the PV cells attached at the edges and taking the entire circumference into account, it is 3.75 for our samples, resulting in the optical efficiency shown in figure 30. Expectedly, η_{opt} follows the same trend with $PbAc_2$ as the I_{LSC} data in figure 29c, exhibiting a maximum of 29 % for PVSK film with 90 % acetate content.

This is an impressive result, one of the highest optical efficiencies reported in semiconductor-based LSCs, demonstrating the suitability of PVSK films as LSC active material. Even the worst device has an efficiency of 15 %. Finally, given the concern regarding the stability of hybrid PVSKs, we follow up with photocurrent measurements after four weeks. The optical efficiency and current output is surprisingly stable, dropping by 15 %–20 % across the different devices, shown in figure 30. We continued monitoring performance up to seven weeks, by which time I_{LSC} decreases by a further 5 %. Such long device stability is unusual for PVSK based devices due to degradation of the PVSK thin film upon exposure to moisture. When certain regions of the PVSK thin film degrade, efficient electron transport is hindered and is thus detrimental to electrical properties of the entire film. However, the film still emits efficiently and since LSCs are purely optical devices, they can be operational in this case. Furthermore, the degradation of PVSK thin film regions results in reduced self-absorption as shown in figure 27, where I_{PL} drops by a smaller amount in the four-week old sample, thus allowing for fewer losses in the older devices and ultimately compensating for the lower initial emission.

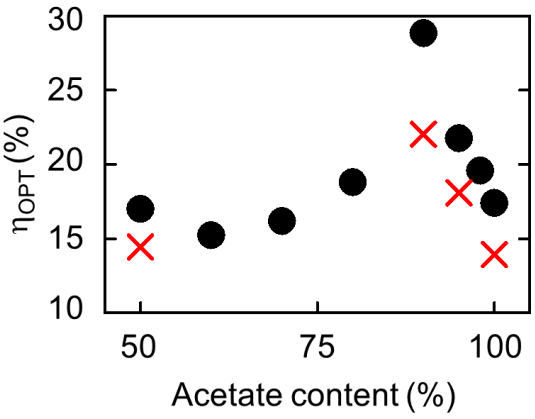

Figure 30. Optical efficiency η_{OPT} varying with $PbAc_2$ content immediately after PVSK film synthesis (circles) and after four weeks (crosses). Reproduced from [1] with permission. © WILEY-VCH Verlag GmbH & Co. KGaA, Weinheim

The power conversion efficiency of the devices is estimated to vary between 7 % and 13 %, and follows the same trend as optical efficiency, calculated using the fill factor from the standard current–voltage curve of a PV cell, shown in figure 31.

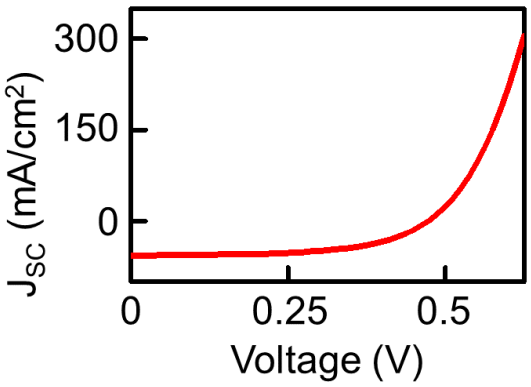

Figure 31. Short circuit current density for PV cell attached to PVSK LSCs. Reproduced from [1] with permission. © WILEY-VCH Verlag GmbH & Co. KGaA, Weinheim

4.3 Conclusion

PVSK films perform very well as active media in LSCs, borne out here by the experimental results and confirmed by simulations. Devices with optical efficiency reaching 29 % have been fabricated, with the lowest optical efficiency being 15 %, whereas the devices were still operational seven weeks later. This superior photocurrent output is resultant of several positive attributes. These include high quantum yield combined with a large refractive index that confines most of the photons in the films. Furthermore, the 780 nm centered emission achieves good spectral matching with the absorption of silicon PV cells, allowing the latter to perform under optimal external quantum efficiency conditions. Tapping into the inherent property of fluorescent materials to down-convert the incident solar light to a more favorable wavelength for solar cells is a central tenet of LSCs.[285] This is the reason that for use with silicon PVs, LSC fluorophores emitting in the far red or near infrared have been so sought after.[298] Dyes are rare at this part of the spectrum and QDs such as PbSe and PbS have low QY and poor photo stability. Hybrid perovskites address most of these concerns and as our time-delayed studies confirm, even though $PbAc_2$ based PVSK thin films are usually associated with quick degradation, their optical properties are preserved for longer, opening a new realm of possibilities for PVSK-based optical devices.[3,299] This study further provides useful insights for optimizing future endeavors of implementing PVSK LSCs. Based on our present results, PVSK LSCs will require significant device engineering before achieving commercialization. Despite the longevity of these devices when compared to PVSK solar cells, efforts to extend their lifetime further is necessary. Such efforts could include encapsulation of films between transparent metal oxides, previously shown to prolong device lifetime in photovoltaic devices.[58] In addition, bottom surface losses could be minimized by deployment of substrates with higher refractive index than glass. PVSK films in photovoltaic device are adjacent to a metal oxide or polymer layer, which commonly have refractive indices higher than glass,[300] and as these deposition techniques have been optimized already, adopting these protocols for LSC devices will prove simple and low cost alternatives.[301,302]

Lastly, self-absorption may be reduced by using PVSK quantum dots and spectral filtering of incident radiation, as it has been demonstrated (figure 27) that selective illumination of PVSK LSCs with a single wavelength reduces the observed emission red-shift and subsequently, self-absorption. Both modifications would aid greatly toward enhancing optical efficiency.

4.4 Experimental section

PVSK precursor solutions of different lead sources are prepared using as-synthesized methylammonium iodide (MAI) (Luminescence Technology Corp.) and various ratios of lead (II) acetate trihydrate ($PbAc_2$, Sigma Aldrich) to lead (II) chloride ($PbCl_2$, Sigma Aldrich); the ratios used are 1:1, 9:1, 19:1, 49:1, and 1:0. For PVSK precursor solutions based on $PbAc_2$ or PbI_2, the only halide present is I, which results in the production of methylammonium lead triiodide ($CH_3NH_3PbI_3$) films. On the other hand, PVSK prepared from precursor solution with $PbCl_2$ contains both I and Cl, thus forming a mixed halide PVSK ($CH_3NH_3PbI_{3-x}Cl_x$).[17] The precursors are dispersed in a bi-solvent system of anhydrous dimethyl sulfoxide and N-methyl-2-pyrrolidione (4:6, v/v) in concentrations of 2.64 M for MAI and 0.88 m for the lead source, respectively.[17,256] PVSK thin films are prepared on UV-ozone treated ITO substrates by spin coating in a nitrogen environment at 4000 rpm for 30 s and are subsequently annealed in a vacuum oven at 60 °C for 20 min. The absorbance spectra are obtained using an Agilent UV–vis spectrophotometer. The PL measurements are done using a 532 nm continuous wave diode laser (Verdi V6, Coherent Inc.) and the spectra are recorded using a 300 mm Acton spectrometer with a thermoelectrically cooled charge-coupled device (spectral resolution ≈0.18 nm). White light experiments are conducted using a broadband source (Motic MLC—150C). SEM images are acquired using Zeiss Gemini SEM 500. Photocurrent measurements are done using a calibrated silicon PV of active area 15×1 mm^2 attached to the edge of the LSC of size $15 \times 15 \times 1$ mm^3 and are conducted outdoors to leverage the solar spectrum.

4.6 Acknowledgements

This research was supported by funds from the National Aeronautics and Space Administration (NASA) grant no. NNX15AQ01A. V.T. gratefully acknowledges the support of user proposals (#3192 and #3715) at the Molecular Foundry, Lawrence Berkeley National Lab, supported by the Office of Basic Energy Sciences, of the U.S. Department of Energy under grant No. DE-AC02-05CH11231.

Chapter 5

Tuning Excitonic Properties of Pure and Mixed Halide Perovskite Thin Films via Interfacial Engineering

This chapter discusses an investigation in the potential of ZnO single crystalline, micro-structured, and nano-structured substrates as means to tune the exciton binding energy and modify charge extraction of pure ($CH_3NH_3PbI_3$) and mixed ($CH_3NH_3PbI_{3-x}Cl_x$) halide PVSK thin films. The interfaces are characterized via scanning electron microscopy and charge transfer is probed via temperature, power, and time-resolved PL spectroscopy. The results indicate that single crystalline ZnO substrates act as efficient electron extraction layers, as they promote PL quenching, and reduced exciton recombination lifetime and exciton density in the PVSK films. On the other hand, micro-structured ZnO substrates show a small increase in PL intensity of PVSK films at room temperature, whereas nano-structured ZnO substrates enhance PL up to 30 thousand times in intensity, and increase exciton recombination rate by 50 %. These trends are seen to vary with temperature, and underline how the underlying ZnO substrate affects exciton dissociation in PVSK thin films. While single crystalline ZnO substrates could be successfully implemented as electron extraction layers in photovoltaic devices, micro-structured and nano-structured ZnO substrates would be suitable for opto-electronic platforms that benefit from high quantum yield of PVSKs.

5.1 Introduction

Hybrid organic–inorganic halide perovskites were first incorporated in solar cells in 2009 as sensitizers, with TiO_2 serving as the electron transport material, and resulted in a device with power conversion efficiency of 3.8 %.[47] Since then, focused effort on device design and materials engineering have resulted in significant improvements, with power conversion efficiencies exceeding 20 % in PPVs.[57,303,304] These superlative metrics can be attributed to the favorable characteristics of hybrid PVSKs as light harvesting media, including broadband absorption, high electron and hole mobilities, when compared to typical values in organic semiconductors, and long charge carrier lifetimes.[305,306] Furthermore, PVSKs can be prepared using solution-based, low temperature techniques that allow for considerable flexibility.[307–310]

The characteristics that have brought cost-effective and high-efficiency solar cells closer to reality also lend themselves to a variety of other applications, such as in tunable lasers, light-emitting diodes, and photodetectors.[22,308,311] In all of these, efficient performance is strongly dependent on the optimal interaction at the interfaces between the

active PVSK film and the extraneous layers implemented for charge dissociation, extraction, and conveyance. The properties of the electron and hole transport layers (ETL and HTL, respectively) therefore play critical roles in the device design.[312] Various ETL materials have been incorporated in PVSK solar cells,[50,58,302,312–316] and among these, ZnO has proven superior in several respects as an ETL. For example, its electron mobility is in the range of 200–300 $cm^2 V^{-1} s^{-1}$, significantly higher than that of TiO_2,[312] and additionally, there have been indications of its contribution to improving long-term operational stability of PVSK devices.[58] Aside from thin films and epi-layers, metal oxide nanostructures have also been incorporated as ETLs in solar cells as a means of increasing absorption cross section without adding to the physical size of the device. Nanowires and nanorods of TiO_2, Y:TiO_2, ZnO, and WO_3 have been implemented in PVSK solar cells as ETLs with promising results,[302,317,318] and again, ZnO is an attractive candidate here too, as ZnO nanostructures can be grown at relatively low temperatures.[254,255,302]

Thus far, the research effort on investigating heterostructures comprising PVSK films and ZnO layers has been focused primarily on photovoltaic characterization. This has necessarily limited the perspective to optimization of power conversion efficiency alone, without systematically studying the fundamental processes occurring at the interface. A detailed and thorough understanding of the interaction between the two materials is necessary not just to optimize device design, but to allow correlation of ZnO layer morphology with charge extraction properties. Only then will it be possible to fully exploit the potential of hybrid perovskites for applications beyond photovoltaics. In this work, we quantify the interfacial interactions using recombination lifetime in PVSK as deposited on ZnO, as well as steady-state PL spectroscopy with varying temperature and excitation power.[18,317,319] The results obtained indicate that while single-crystalline ZnO can be leveraged as an efficient electron extraction layer for application in photovoltaic devices, the micro- and nanostructured layers lead to PVSK emission enhancement, the latter by almost a thousand-fold. While this is far from ideal for charge extraction, it opens new opportunities for other optoelectronic applications that can benefit by leveraging the high optical quantum yield of PVSK materials.

5.2 Results

5.2.1 ZnO layer characteristics

Figure 32 introduces the different ZnO substrates used in this study. The microstructured ZnO sample (MS-ZnO), shown in figure 32a, consists of relatively large features, with lengths of ≈1 μm and diameters ranging between 200 and 400 nm. The nanostructured ZnO sample (NS-ZnO) consists of nanowires that are ≈1.5 μm long and 50 nm in diameter, shown in figure 32b. The third ZnO layer used is a commercially acquired single crystal (SC-ZnO) from Tokyo Denpa Inc. The PL spectra of the three layers are summarized in figure 32c,d. Figure 32c compares the PL of MS-ZnO and SC-ZnO. The emission centered around 380 nm is the direct bandgap emission, while the luminescence in the range 500–600 nm, routinely observed in ZnO samples, is associated with defects

arising from surface states and oxygen vacancies.[320] The emission spectra of the NS-ZnO before and after annealing in figure 32d show that these have the most intense PL, as the radial confinement of excitons within the nanostructures increase the probability of recombination.[321] Emission intensity of NS-ZnO is enhanced, and the defect emission significantly quenched, after annealing, a common observation attributed to improved crystallinity.[322,323] The emission peaks of the ZnO structures prepared in our laboratory are redshifted compared to the single-crystal emission, resultant of increased contribution from recombination of bound excitons as the size of the structure is reduced and carriers confined.[322,323]

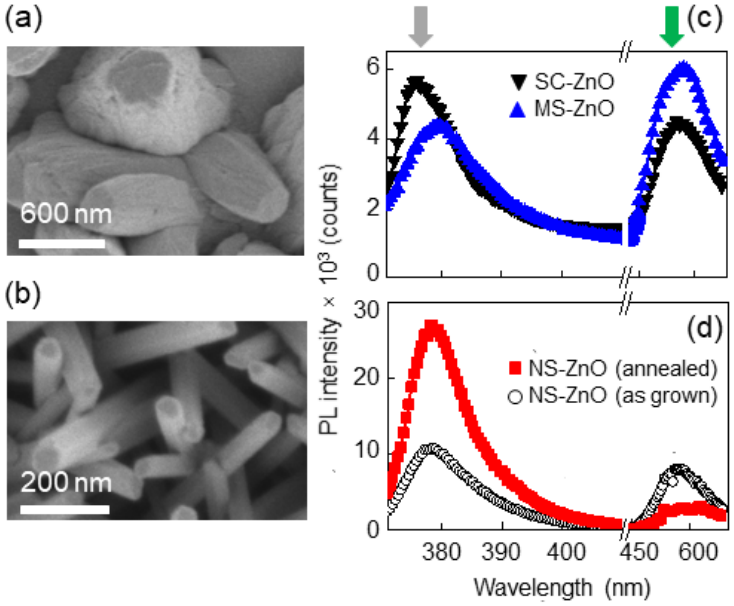

Figure 32. (a, b) SEM image of micro-structured (MS-ZnO) and nano-structured (NS-ZnO) layers. (c) PL results comparing the emission from both the band edge (gray arrow) and defect states (green arrow) from single crystalline (SC-ZnO) and micro-structured (MS-ZnO) layers. (d) PL of NS-ZnO layers pre- and post-annealing in air demonstrates significant success in suppressing defect emission and consequently, enhancing band gap signal. Reproduced from [2] with permission. © WILEY-VCH Verlag GmbH & Co. KGaA, Weinheim

5.2.2 PVSK thin film and ZnO layer interface characteristics

Figure 33 is a compilation of morphological and fluorescence characteristics of the surface of the $CH_3NH_3PbI_3$-ZnO samples. Figure 33a is the scanning electron microscope (SEM) image of a PVSK film deposited on indium tin oxide (ITO) coated glass (ITO/PVSK), and shows uniform small grains, as is associated with PVSK thin films prepared with precursor containing lead acetate.[17]

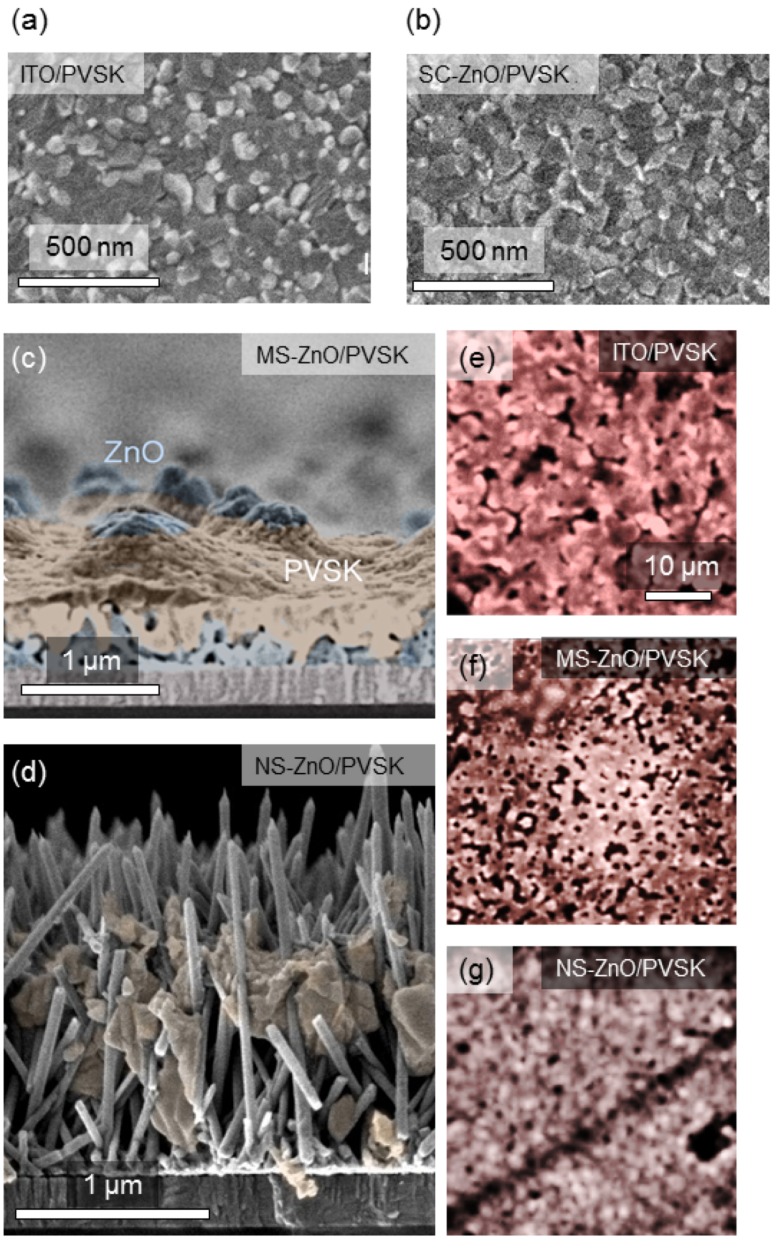

Figure 33. Top down SEM images of $CH_3NH_3PbI_3$ films deposited on (a) ITO and (b) SC-ZnO showing very similar morphology. Side-view of $CH_3NH_3PbI_3$ deposition on (c) MS-ZnO and (d) NS-ZnO. Fluorescence images of (e) ITO/PVSK, (f) MS-ZnO/PVSK, and (g) NS-ZnO/PVSK show increasingly smaller grain formation with reduction in size of ZnO features. Hence, grain size is now below the microscope resolution limit, which prevents acquisition of a clearer image. Scale bar in (e) applies to (f, g). Reproduced from [2] with permission. © WILEY-VCH Verlag GmbH & Co. KGaA, Weinheim

The choice of ITO-coated glass as the control sample is motivated by the fact that along with FTO, ITO is one of the most commonly used substrates for PVSK thin film deposition. Given that ITO itself may act as an electron extraction layer, we have investigated PVSK deposited on glass without ITO coating to provide a second baseline. SEM imaging (figure 34a,b) and spectroscopy (figure 34c,d) data demonstrate that there is no noticeable difference between these two substrates, and therefore, ITO itself does not have a significant impact as an extraction layer.

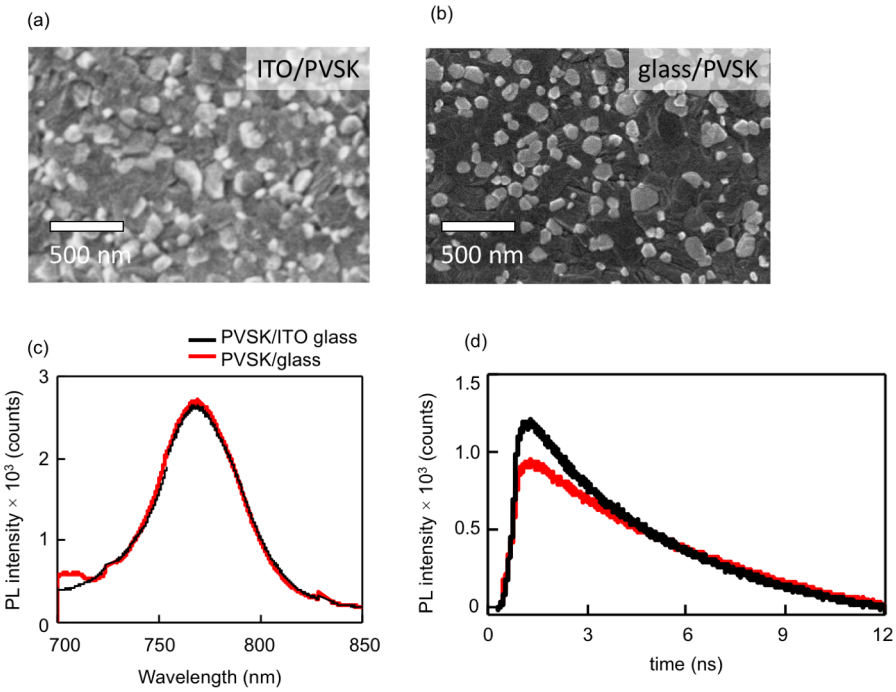

Figure 34. SEM images of $CH_3NH_3PbI_3$ deposited on (a) ITO glass, and (b) glass. (c) Static and (d) time-resolved PL of the two samples. Exponential fits to the time-resolved data reveal a lifetime of 7.4± 0.3 ns for PVSK/ITO and 8±1 ns for PVSK/glass. The static spectra curves shown are averaged over three data sets for each type of sample. Reproduced from [2] with permission. © WILEY-VCH Verlag GmbH & Co. KGaA, Weinheim

Figure 33b shows the PVSK thin film as deposited on the ZnO single crystal (SC-ZnO/PVSK). This PVSK layer also has a pinhole-free surface and small grain size, like the ITO/PVSK film in figure 33a, demonstrating that the smooth surface of the ZnO single crystal is not disruptive to the PVSK thin film structure. Figure 33c is a cross-sectional SEM image of the MS-ZnO/PVSK sample, and highlights that while there is good contact between the two materials, the PVSK film has discontinuities arising from the roughness of the ZnO layer (figure 35). Figure 33d shows that contact between PVSK and NS-ZnO is not as optimal due to the high surface roughness of the ZnO layer, and while the PVSK infiltrates the nanowires to form a heterostructure with multiple points of contact between the two materials, coalescing of PVSK occurs in regions deep in the nanostructured layer (figure 35). Fluorescence microscope images of three samples, ITO/ PVSK, MS-ZnO/PVSK, and NS-ZnO/PVSK, prepared with $CH_3NH_3PbI_{3-x}Cl_x$, are shown in figure

33e–g, respectively. These images underline the impact of roughness of the ZnO layers on the PVSK thin film. In figure 33e, the ITO/PVSK thin film shows a characteristic pattern of large grains of varying fluorescence intensity delineated by dark grain boundaries, the latter known to act as recombination centers.[15] A similar image of MS-ZnO/PVSK in figure 33f shows a decrease in grain size, and a further proliferation of grain boundaries accompanied by even greater reduction in grain size is observed in the fluorescence image of NS-ZnO/PVSK in figure 33g, reaching the limit of the microscope resolution. These would suggest that ZnO layers with higher surface roughness are detrimental to charge transfer across the device interface[15,286] and this conjecture is validated in figure 36, where we observe increased PVSK PL, instead of PL quenching, the typical signature of efficient ETLs.[324]

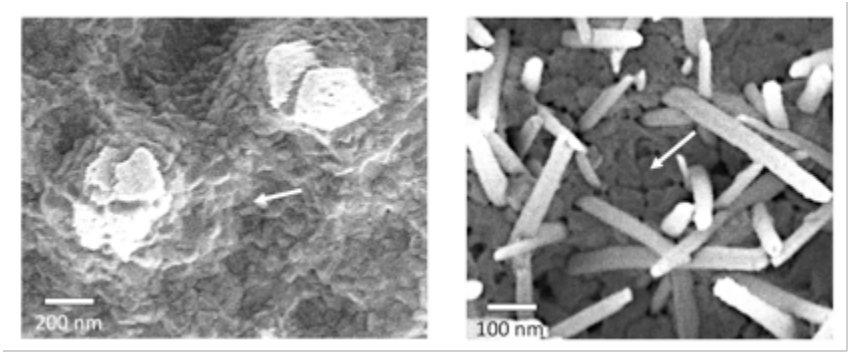

Figure 35. Top down SEM image of $CH_3NH_3PbI_3$ deposited on (left) MS-ZnO and (right) NS-ZnO showing the disruption of the $CH_3NH_3PbI_3$ film (arrows) due to the high surface roughness of the ZnO layer. Reproduced from [2] with permission. © WILEY-VCH Verlag GmbH & Co. KGaA, Weinheim

The PL spectrum of SC-ZnO/PVSK in figure 36a shows the emission intensity quenching by a factor of ≈3 when compared to that of ITO/PVSK and is accompanied by a small decrease in room-temperature recombination lifetime (figure 36b), from 4.9 to 4 ns. The behavior of the PVSK thin films deposited on the micro- and nanostructured ZnO layers is very different. The PL spectra of MS-ZnO/PVSK and NS-ZnO/PVSK are plotted in figure 36c. MS-ZnO/PVSK exhibits an enhancement of PVSK luminescence by a factor of 20, while PL intensity upsurges by almost $\times 10^3$ in NS-ZnO/PVSK. Room-temperature time-resolved PL in figure 36d, and the extracted lifetimes averaged over different spots on the samples summarized in the inset to figure 36b show that, in conjunction with PL increase, both MS-ZnO/PVSK and NS-ZnO/ PVSK heterostructures reduce the recombination lifetimes, by 16% and 55%, respectively. PVSK PL quenching is characteristic of charge extraction from the PVSK layer to the underlying ETL as depicted in figure 37,[324] and together with the reduced lifetime, suggests that SC-ZnO is indeed acting as one. The PL enhancement in figure 36c, particularly that observed in the NS-ZnO/PVSK, is more reminiscent of Purcell effect, a result supported by the rapid recombination occurring in those samples. The proliferation of grain boundaries in the PVSK thin film when deposited on the micro and nanostructured ZnO layers might be causing increased confinement of excitons in the smaller PVSK grains, resulting in increased spontaneous emission and faster recombination based on a random walk

model.[325] The PL enhancement factor in the NS-ZnO/PVSK samples can be driven as high as 3×10^4 with excitation power, as shown in the inset to figure 36d, before it saturates. While this combination is not suitable for charge extraction, it demonstrates great potential for optoelectronic applications, such as photodetectors with the capability of magnifying the input signal many-fold. This variation in how PVSK PL is modulated by the ZnO substrates might have a contribution beyond the morphology, since there is an inherent variation in the carrier concentration of the three substrates, resultant of the synthesis process. The single-crystal carrier density[326,327] is in the range 10^{14}–10^{15} cm^{-3},[326,327] while that of the MS-ZnO and NS-ZnO is higher,[328,329] in the range 10^{17}–10^{18} cm^{-3}. It is possible that a higher carrier concentration makes MS-ZnO and NS-ZnO substrates inefficient as ETLs, but that cannot be established beyond doubt. It is quite certain, however, carrier density is not the cause of the increased PL emission of the NS-ZnO/PVSK heterostructures, since the MS-ZnO/PVSK does not demonstrate an enhancement anywhere close despite having a similar carrier concentration.

The variation in PVSK characteristics with the use of different halide precursors is well-documented,[1] and for consistency, we repeated our measurements with samples fabricated with lead chloride as the source in the precursor to confirm the trends observed in samples prepared with lead acetate. For $CH_3NH_3PbI_{3-x}Cl_x$ thin films annealed in the vacuum oven, the observed trends for PL quenching and exciton recombination lifetime agree with the trends demonstrated with $CH_3NH_3PbI_3$ thin films. PL intensity of PVSK is reduced by 90 % when PVSK is deposited on SC-ZnO, as shown in figure 36e. Also, as before, PL intensity is enhanced (albeit very slightly, by a factor of 1.4) when NS-ZnO is used. Figure 36f plots the time-resolved PL of $CH_3NH_3PbI_{3-x}Cl_x$ on the different ZnO layers, all of which reduce the average recombination lifetime, summarized in the inset. Again, while SC-ZnO and MS-ZnO reduce the average lifetime by ≈20 %, use of NS-ZnO results in a lifetime 40 % shorter. These results are attributed to similar phenomena as discussed previously: SC-ZnO is effectively extracting electrons from the PVSK layer, whereas NS-ZnO is confining excitons within grains, as indicated by the short lifetime but enhanced PL intensity. However, the phenomenon is not as prominent as in the case of lead acetate based PVSK due to the larger PVSK grains when fabricated with lead chloride precursor.

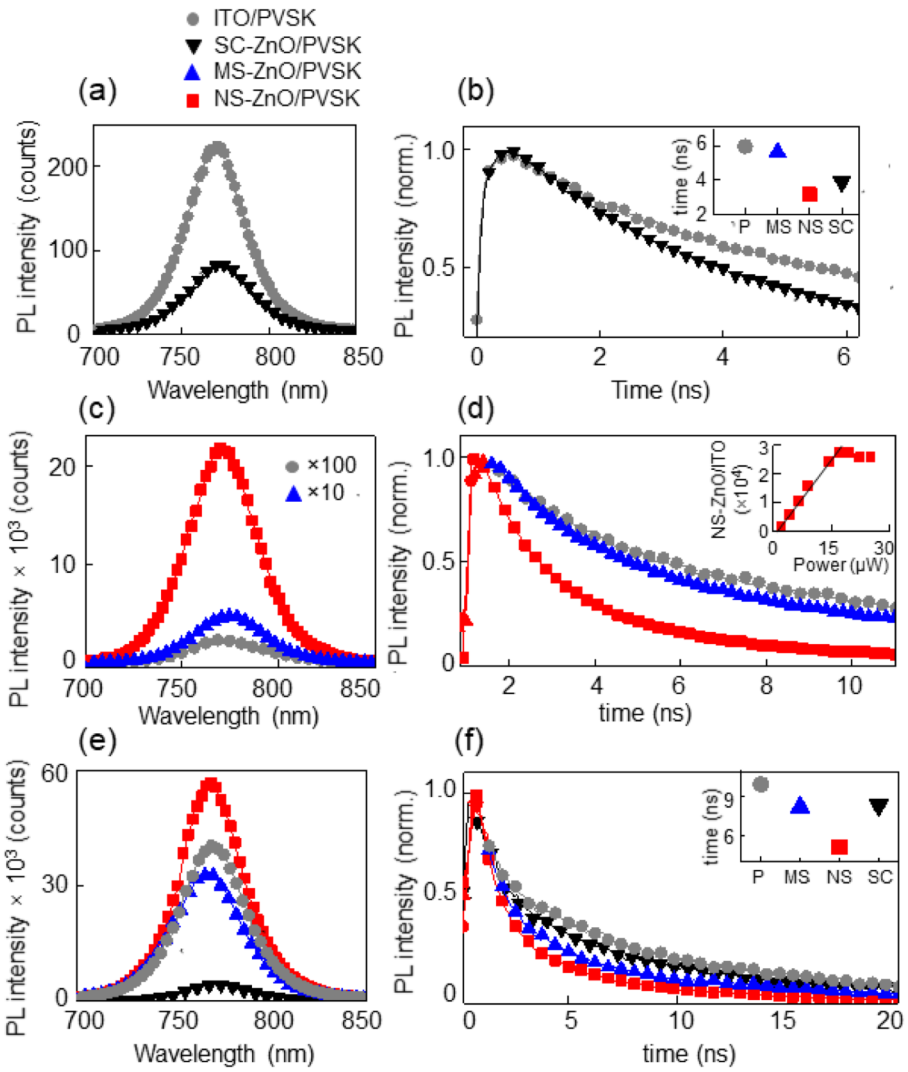

Figure 36. (a) Static and (b) time-resolved PL emission of $CH_3NH_3PbI_3$ on ITO and SC-ZnO exhibit PL quenching and faster charge extraction in the latter. (c, d) Static and dynamic PL comparing results of ITO/PVSK, MS-ZnO/PVSK, and NS-ZnO/PVSK. (b, inset) Average recombination times of $CH_3NH_3PbI_3$ on the four different ZnO layers. (d, inset) Integrated PL from NS-ZnO/PVSK varying with excitation power, normalized to ITO/PVSK emission (e, f) Static and dynamic PL of $CH_3NH_3PbI_{3-x}Cl_x$ deposited on the four layers. (f, inset) Average lifetimes. Reproduced from [2] with permission. © WILEY-VCH Verlag GmbH & Co. KGaA, Weinheim

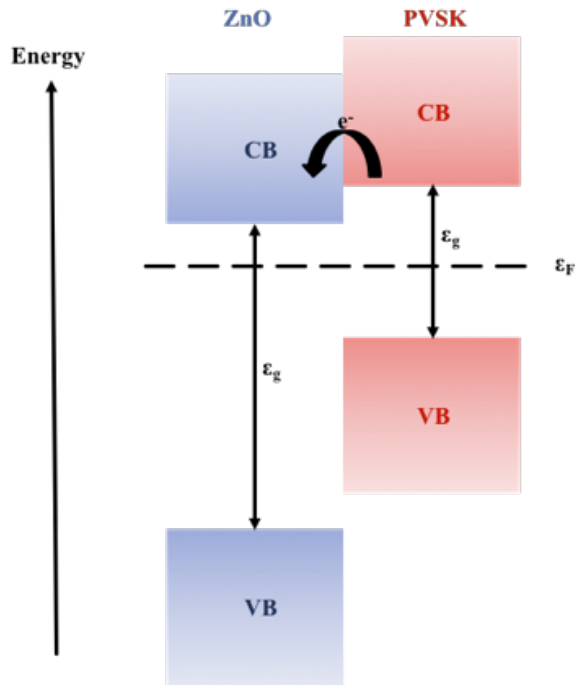

Figure 37. PVSK PL quenching is characteristic of electron extraction by electron transport layer (ZnO). Reproduced from [2] with permission. © WILEY-VCH Verlag GmbH & Co. KGaA, Weinheim

We have also investigated the properties of thermally annealed $CH_3NH_3PbI_{3-x}Cl_x$ thin films, performed using a hot plate at a significantly higher temperature than vacuum annealing (110 °C), and over a period thrice as long. High-temperature thermal annealing of PVSK has been associated with reduced number of pores in the film, but also with increased pore size, which results in reduced coverage of the substrate.[330,331] Furthermore, annealing for long time periods has been observed to lead to PVSK decomposition due to the formation of PbI_2.[69,332] Expectedly, these samples show significantly modified properties. The PVSK thin film deposited on ITO glass appears to be optically almost "dark," and PL is progressively enhanced by the nanostructured, single-crystalline, and micro-structured ZnO layers, as shown in figure 38a, in that order. Further, incorporation of ZnO prolongs the recombination lifetime for all the samples, indicating electron transfer is hindered for these samples, as demonstrated in figure 38b. These results underline the importance of the annealing method during fabrication, not only for the quality of the PVSK layer but also for proper interpretation of the electron extraction afforded by ZnO.

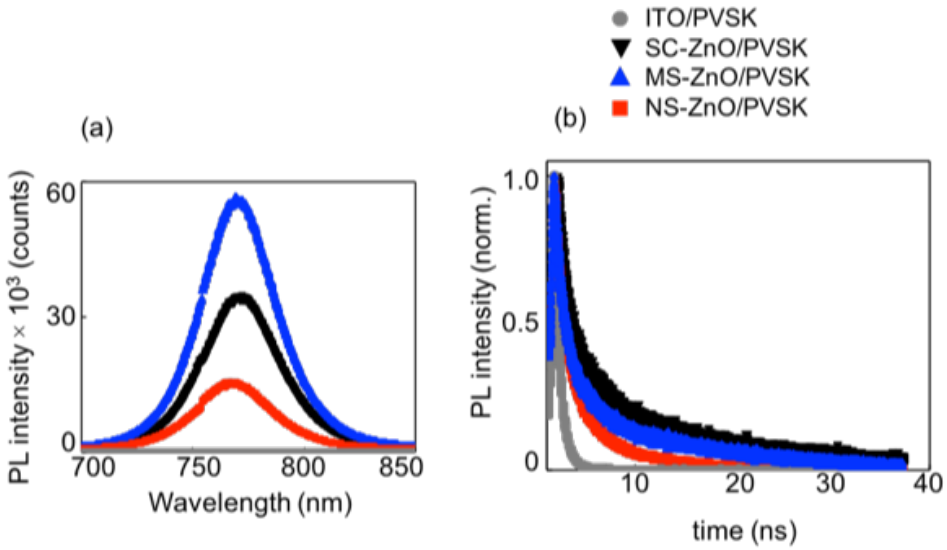

Figure 38. (a) Static and (b) time-resolved PL of hot plate annealed $CH_3NH_3PbI_{3-x}Cl_x$ deposited on ITO glass, SC-ZnO, MS-ZnO, NS-ZnO. Reproduced from [2] with permission. © WILEY-VCH Verlag GmbH & Co. KGaA, Weinheim

5.2.3 Temperature dependence of PL tuning

In hybrid PVSK thin films, PL emission has contributions from recombination of both excitons and free electron–hole pairs, with the proportion of each determined by the temperature and the exciton binding energy E_B. Tuning E_B has been successfully leveraged to improve interactions at the interface, including charge extraction efficiency and PL enhancement. Some examples comprise the use of heterostructures[333] and plasmonic nanoparticles[334] to modify E_B and improve electronic transport properties in hybrid PVSK solar cells. Beyond PVSKs, the use of coulomb engineering through modification of the local dielectric environment[335] has been demonstrated to tune E_B in 2D WS_2 and WSe_2 heterojunctions. Integration with a wide bandgap ETL has the potential of tuning E_B in PVSKs as well, and we investigate that possibility next. Figure 39 follows the variation in $CH_3NH_3PbI_3$ emission on the ZnO layers at different temperatures. The spectral shift between the results in figure 39a,b is driven by the structural phase transition. The other notable difference is that while at 180 K PL intensities from all four sample types have the same relationship with respect to the ITO/PVSK film, from 100 K down, SC-ZnO/PVSK PL is no longer quenched. In fact, by 20 K, SC-ZnO enhances PVSK PL by almost a factor of 4. This variation as a function of temperature T is shown in figure 39e in the form of the ratio of PL intensities of SC-ZnO/PVSK and ITO/ PVSK. Similar data for MS-ZnO/PVSK in figure 39f demonstrate a mild increase in PL over the entire temperature range, without any quenching. Nanostructured ZnO layers affect the PVSK PL most strikingly, resulting in a steady enhancement that reaches a thousand-fold by room temperature, in figure 39g. To investigate if the quenching/enhancement driven by the substrates relate to the PVSK thin films, we focus next on calculating the proportion of free and bound charge carriers and if the presence of the different substrates has any noticeable effect.

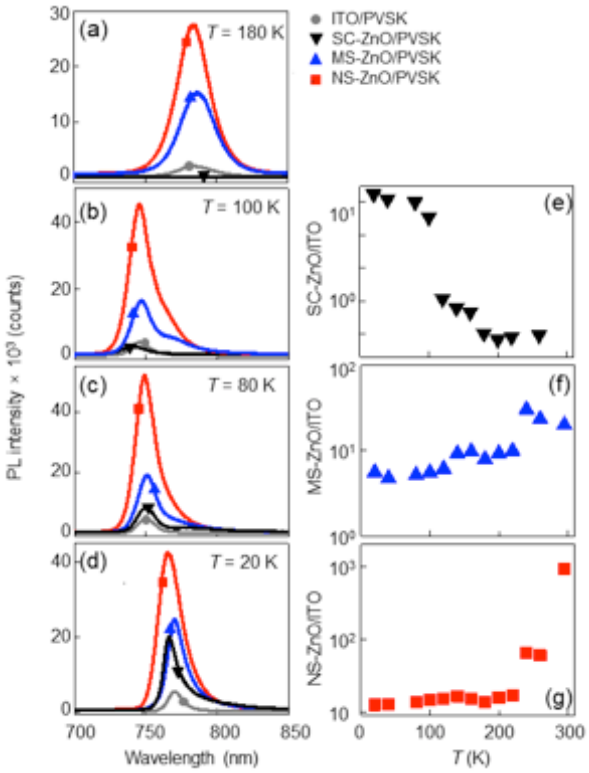

Figure 39. PL spectra of $CH_3NH_3PbI_3$ deposited on the four different ZnO layers at (a) 180 K, (b) 100 K, (c) 80 K, and (d) 20 K. The integrated PL intensity of PVSK deposited on: (e) SC-ZnO, (f) MS-ZnO, and (g) NS-ZnO, normalized with respect to emission from PVSK on ITO. Reproduced from [2] with permission. © WILEY-VCH Verlag GmbH & Co. KGaA, Weinheim

5.2.4 Exciton recombination in PVSK tuned by ZnO layers

The variation of spectrally integrated PL intensity with excitation power at different temperatures has proven insightful in estimating the exciton binding energy E_B. Equation 57 shows the variation of the integrated intensity I_{PL} as

$$I_{PL} \sim Ax^2[N_{tot}]^2 + B(1-x)N_{tot} \tag{57}$$

where x is the fraction of free charge carriers, and $(1-x)$ the fraction of excitons that recombine radiatively; A and B are the bimolecular and the monomolecular recombination coefficients, respectively. N_{tot} is the total charge carrier density, directly proportional to the excitation power P, implying $I_{PL} \propto P^2$ for free charge carriers and $I_{PL} \propto P$ for excitonic recombination. Therefore, by fitting a second order polynomial to the power-dependent PL of PVSK at any fixed temperature T, as described in figure 42 in Supporting Information, the quadratic and linear coefficients corresponding to free charge carriers and excitons[18,69] at that T can be extracted, which in turn allow E_B and the relative proportion of free and bound charge carriers to be evaluated, as summarized in figure 40.

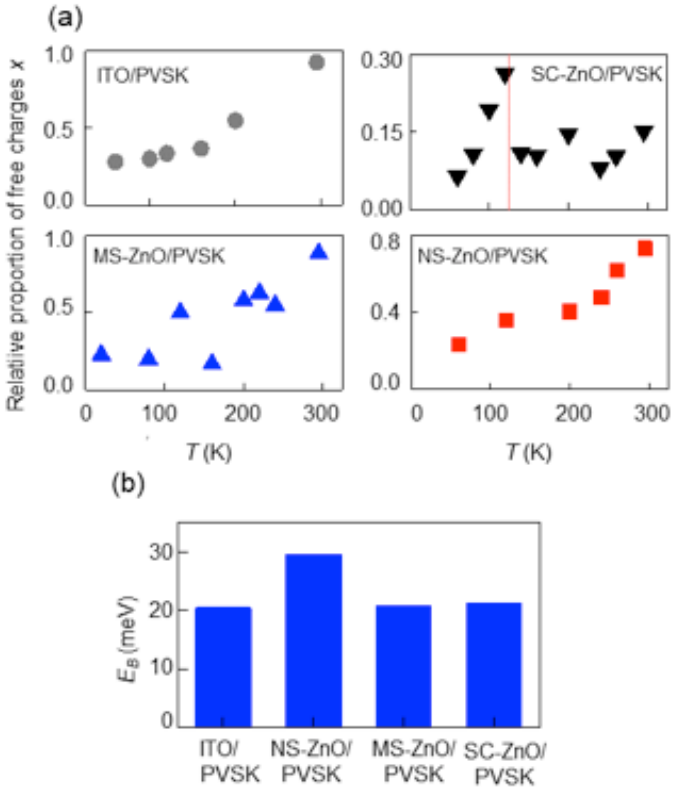

Figure 40. (a) Relative proportion of free charge carriers varying with temperature T for $CH_3NH_3PbI_3$ deposited on ITO and the three ZnO substrates, normalized to the ITO/PVSK result. (b) exciton binding energy E_B calculated for each type of substrate. Reproduced from [2] with permission. © WILEY-VCH Verlag GmbH & Co. KGaA, Weinheim

We use a formalism[69] based on the Saha–Langmuir equation shown in Equation 58:

$$\frac{x^2}{1-x} = \frac{1}{N_{tot}}\left(\frac{2\pi\mu k_B T}{h^2}\right)^{3/2} e^{-E_B/k_B T} \tag{58}$$

μ is the reduced exciton mass ($\approx 0.1 m_e$), where m_e is the free electron mass, k_B is the Boltzmann constant, and h is the Planck's constant. To extract E_B from the acquired data while accounting for the coefficients A and B of Equation (57), we fit Equation (58) to the ratio of the quadratic-to-linear weights versus $1/T$, as depicted in figure 43 in Supporting Information.

The proportional weights of free charge carriers, normalized to the ITO/PVSK control sample's, are plotted in figure 40a as functions of T, while E_B values for each sample are plotted in figure 40b. In ITO/PVSK, the proportion of free carriers contributing to recombination decreases with temperature T, which is typical, as excitonic recombination begins to dominate with reduced T. The same is the case for the other samples as well, although in SC-ZnO/PVSK there is a nonmonotonicity, with a discontinuity arising around the temperature where the structural phase transition occurs.

We have calculated E_B averaged over the entire temperature range over which PL is collected, but in some instances,[69] E_B has shown different values in the two structural phases, with a smaller binding energy in the low *T* orthorhombic phase. This might explain the increase in free carriers around the transition. Aside from this, figure 40a further shows significantly fewer free charge carriers in SC-ZnO/PVSK at 295 K (70 % fewer than in ITO/PVSK), which cannot be attributed to higher E_B, which is practically unchanged from E_B in ITO/PVSK, as figure 40b demonstrates. Therefore, the apparent reduced proportion of free carriers can only be a consequence of transfer from PVSK to SC-ZnO, confirming carrier extraction indicated by quenching of PL. Additionally, the temperature where free carrier fractional value shows a jump in figure 40a, indicated by the dashed line, is very close to where PVSK PL is no longer quenched by the SC-ZnO substrate in figure 39e. MS-ZnO/PVSK behaves most like ITO/PVSK, with E_B and free carrier proportions both being very similar. Given that these microstructured substrates do not affect PL significantly in figure 39f, this is not unexpected.

The results from samples incorporating the NS-ZnO substrates are subtler. The free carrier contribution in figure 40a is 20 % less compared to ITO/PVSK, but PL enhancement, rather than quenching, over the entire experimental temperature range affirms that there is no carrier extraction. E_B is higher than all the other three samples in figure 40b, and this accounts for fewer free electrons and holes. The question then is: what the underlying cause for the increased binding energy is, and if the same can also account for the markedly reduced recombination time seen in figure 36d. The surface topology of the NS-ZnO layer most definitely has a role to play, and we have observed the increased roughness disrupts the formation of the PVSK thin films during annealing, as demonstrated in figure 41.

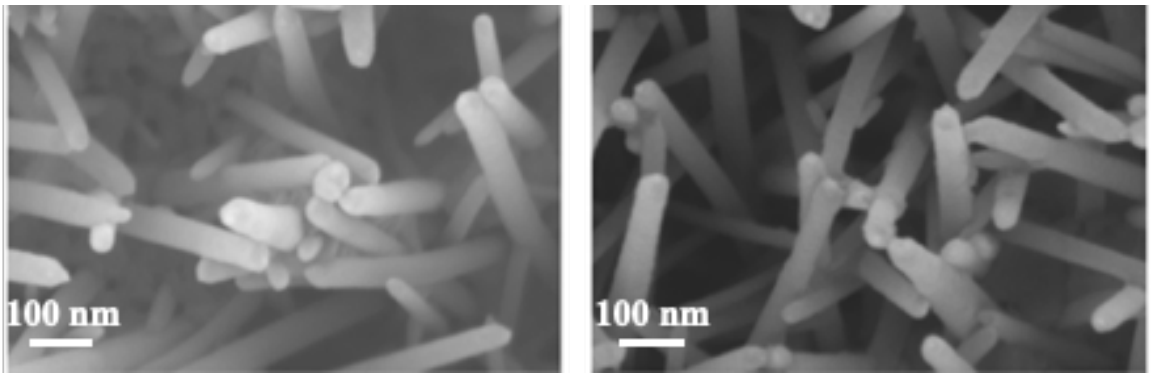

Figure 41. SEM images demonstrating radial coverage of ZnO NWs by PVSK. Reproduced from [2] with permission. © WILEY-VCH Verlag GmbH & Co. KGaA, Weinheim

This leads to the formation of smaller grains, with average size on the order of the diffraction limit of the optical microscope in figure 33g. We speculate that these sub-micrometer sized grains could be confining the excitons, not only limiting charge carrier transport within the PVSK film, but also increasing E_B. Further, this confinement would account for higher recombination rates, as the wavefunctions of electrons and holes are overlapping, leading to increased probability of recombination of the electron-hole pairs.

Interestingly, in the $CH_3NH_3PbI_{3-x}Cl_x$ films with prolonged thermal annealing that results in smaller grains, we observe a similar PL enhancement for all the ZnO substrates, likely arising from the same cause as highlighted here.

5.3 Conclusion

Hybrid perovskites have properties that make them highly desirable for a range of applications, extending well beyond photovoltaics. Customizing them for optimal performance in different applications will necessarily require careful design of device architecture, which makes tailoring interface properties to achieve desired optoelectronic characteristics essential. Based on our work, planar interfaces appear to be the most optimum structure for charge extraction. This result is supported by means of optical measurements which have been used to quantify exciton lifetime, nature of charge carriers recombining to result in PL, and PL intensity quenching. The experimental data are supplemented by calculations of E_B to better understand the fundamental processes occurring at the SC-ZnO/PVSK interface. And, while optical measurements portray a clear picture, future endeavors must also include electrical measurements to fully quantify electron flow within the device.

The more interesting part of our findings is the PL enhancement observed in the roughened layers, most significantly in the nanostructured films, which we establish cannot be attributed to the carrier density of the ZnO substrates. Instead of reducing E_B and increasing charge carrier extraction as might have been expected owing to the increased contact area between the ZnO and PVSK, we observed enhanced exciton binding by carrier confinement and up to several thousand-fold increase in PVSK emission intensity. This is an aspect of charge modulation in hybrid PVSK thin films that have not been focused on, centered on optoelectronic properties rather than photovoltaics. Hybrid PVSKs are renowned for excellence in the former as well, with consistently high quantum yield and long charge lifetimes. Our results highlight the possibility of entirely novel applications that would exploit these characteristics, paving the way for device platforms that have not been considered in the realm of PVSKs yet.

5.4 Experimental Section

ZnO nanowires (NS-ZnO) are synthesized using previously reported techniques.[254] A catalyst containing solution was prepared using poly(4-vinyl pyridine) (P4VP, Polymer Source, Inc.) of molecular weight 60 000 g mol−1 and Zn(II) acetylacetone (Sigma Aldrich) dissolved in 1-butanol (Sigma Aldrich). The P4VP weight ratio is 0.3 wt % and the metal-to-polymer molar ratio is 0.8:1. The solution was mixed for 5 h under magnetic stirring and was deposited on indium tin oxide (ITO) glass substrate by spin-coating at 3000 rpm for 30 s. After the deposition of each layer the sample was baked for 2 min at 100 °C to remove the solvent and prevent intermixing. The samples were then annealed at 350 °C for 30 min in air to remove the polymer template and form nanoparticles. Although the annealing temperature might reduce the conductivity of the ITO layer, it does not influence the interaction between the PVSK and ZnO layers.

Nanowires were grown using a solution-based hydrothermal technique in a Teflon-lined stainless steel autoclave, with the active side of the substrates facing down. 20×10^{-3} M of hexamethylenetetramine (HMTA, VWR, 99+ %) and zinc nitrate hexahydrate (VWR, 99.998 %) mixed in deionized water were used for the growth.[254] The synthesis was done at 95 °C in an oven (Yamato ADP 21 vacuum oven) for 6 h. Once nanowire synthesis was complete the nanowires underwent post-annealing at 400 °C in air.

Electrodeposition of micro-structured ZnO (MS-ZnO) was achieved using conditions reported elsewhere.[255] Electrodeposition was done in a three-electrode cell maintained at 88 °C with the aid of an oil bath, with zinc foil as the counter electrode and Ag/AgCl as the reference electrode, raised above the solution to keep at lower temperature. A Princeton Instruments galvanometer was used to monitor and provide the necessary voltage for deposition. Deposition was conducted using deionized water based solutions of 5×10^{-3} M of $ZnCl_2$ (Alfa Aesar) and 0.1 M KCl (VWR). The solution was saturated with molecular oxygen and slight O_2 bubbling was kept throughout the deposition. The applied potential is −0.82 V versus Ag/AgCl and deposition was finished when the total electrical charge exchanged was 1.1 C cm^{-2}. A ZnO single crystal, commercially purchased from Tokyo Denpa Inc., was used as the lowest surface roughness sample. PVSK ($CH_3NH_3PbI_3$) precursor was prepared from 2.64 M of methylammonium iodide (MAI, Luminescence Technology Corp.) and 0.88 M of lead (II) acetate trihydrate (Sigma Aldrich), dispersed in N,N-dimethylformadide (DMF). PVSK thin films were spin-coated on UV/ozone-treated ITO glass substrate or UV/ozone-treated ZnO at 4000 rpm for 30 s and were subsequently annealed on a hot plate at 100 °C for 5 min, in a nitrogen environment. Similarly, for preparation of $CH_3NH_3PbI_{3-x}Cl_x$ thin films, 2.64 M of MAI and 0.88 M of lead chloride (Sigma Aldrich) were dispersed in DMF, followed by spin-coating at 4000 rpm for 30 s. Annealing of samples was done using two different methods: on a hot plate in N_2 environment at 110 °C until the surface turned dark brown or in a vacuum oven at 60 °C until samples turned dark brown.[257,329]

A pulsed Ti:sapphire laser (Mira, Coherent Inc., repetition rate 13 ns) was frequency-doubled using a BBO crystal to 355 nm for the optical measurements of ZnO, and tuned to 408 nm for acquiring PVSK PL. An Acton 300i spectrometer with a thermoelectrically cooled charge-coupled device, with spectral resolution of 0.18 nm, was used to collect PL spectra. Temperature-dependent measurements were conducted in a cryo-free system from Advanced Research Systems (base temperature 10 K). A time-correlated single photon counting (TCSPC) system from Picoquant was used for time-resolved PL. An Agilent UV– vis spectrophotometer was used to record the absorbance spectra of the samples and SEM images were obtained with Zeiss Gemini SEM 500. Fluorescence images of the PVSK thin films were obtained using a confocal microscope (Zeiss LSM 700) which allows the possibility of dual-mode fluorescence-SEM imaging.

5.5 Supporting Information

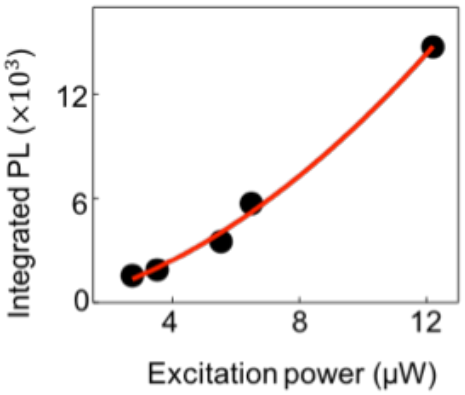

Figure 42. Integrated PL intensity of $CH_3NH_3PbI_3$ plotted with excitation power. The line represents the second order polynomial fit used to extract the number of excitons and free charge carriers in the PL signal, Eq. 59. Reproduced from [2] with permission. © WILEY-VCH Verlag GmbH & Co. KGaA, Weinheim

$$I_{PL} \sim Ax^2[N_{tot}]^2 + B(1-x)N_{tot} \tag{59}$$

This fitting exercise returns the quadratic and linear coefficient, where quadratic = Ax^2 and linear = $B(1-x)$

Therefore,

$$\text{quadratic/linear} = Ax^2 / B(1-x) \tag{60}$$

$$\Longrightarrow \frac{x^2}{1-x} = \frac{B \times quadratic}{A \times linear} \tag{61}$$

substituting in the Saha-Langmuir equation

$$\frac{x^2}{1-x} = \frac{1}{N_{tot}} \left(\frac{2\pi\mu k_B T}{h^2}\right)^{3/2} e^{-E_B/k_B T}$$

we get

$$\frac{B \times quadratic}{A \times linear} = \frac{1}{N_{tot}} \left(\frac{2\pi\mu k_B T}{h^2}\right)^{3/2} e^{-E_B/k_B T} \tag{62}$$

$$\Longrightarrow \frac{quadratic}{linear} = \frac{A}{B} \times \frac{1}{N_{tot}} \left(\frac{2\pi\mu k_B T}{h^2}\right)^{3/2} e^{-E_B/k_B T} \tag{63}$$

We then proceed to plot quadratic/linear versus *1/T* in for the different substrates in figure 43.

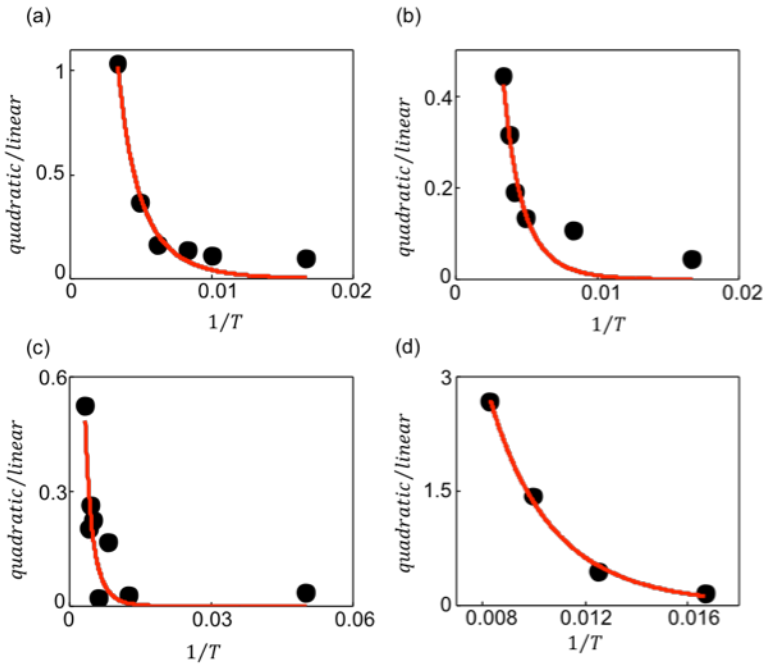

Figure 43. The ratio of quadratic/linear coefficients as extracted from equations 60 and 61 are plotted against *1/T* for $CH_3NH_3PbI_3$ films deposited on (a) ITO, (b) NS-ZnO, (c) MS-ZnO, and (d) SC-ZnO. The fitted lines are used to extract EB value of each sample using Equation 63. Reproduced from [2] with permission. © WILEY-VCH Verlag GmbH & Co. KGaA, Weinheim

This data is fitted:

$$y = Constant \cdot (1/\mathrm{x})^{3/2} e^{-\frac{E_B}{k_B}x} \tag{64}$$

In this equation, *y=quadratic/linear*, *x=1/T*, and constant = $\frac{A}{B} \times \frac{1}{N_{tot}} (\frac{2\pi\mu k_B}{h^2})^{3/2}$.

From these fits the constant and the exponent values are extracted, allowing us to solve for *A/B* (since all the other values in the constant are known) and E_B, respectively. Since we know what *A/B* is, now we can solve for *x* for each sample using equation 61.

5.6 Acknowledgements

This work was supported by NASA MIRO Grant No. NNX15AQ01A. K.N. and S.S. acknowledge support of the Southern California Edison Graduate Fellowships. Part of imaging characterizations in this work was performed under User Proposals (No. 3715) at the Molecular Foundry, Lawrence Berkeley National Lab, supported by the Office of Basic Energy Sciences, of the U.S. Department of Energy under Contract No. DE-AC02-05CH11231.

Chapter 6

Magneto-plasmonic coupling in α-Fe_2O_3/Au heterostructures

In this chapter, the interaction of weakly ferromagnetic hematite (α-Fe_2O_3) nanowires with Au nanoparticles is investigated via magneto-optical Kerr effect (MOKE) spectroscopy to observe any modifications of the magneto-optical properties of hematite due to excitation of the localized surface plasmon resonance of the Au nanoparticles. The impact of different loadings of Au nanoparticles (1 wt% and 5 wt%) is observed, for samples that are tested as grown and for samples that have undergone post-annealing at 300 °C. Strong coupling between the two materials is observed for annealed samples and is demonstrated as an enhancement of the complex Kerr rotation of the reflected light. It is believed that post-annealing enhances the properties of Au nanoparticles and the contact between the two materials, leading to improved MO response of the heterostructures. While Kerr rotation shows greater enhancement for samples with 1 wt% Au nanoparticles, Kerr ellipticity shows greater increase in samples with higher Au nanoparticle loading. This is attributed to a lower amount of hematite present in the sample as the Au nanoparticle loading increases, which results in smaller changes of Kerr rotation as it is proportional to sample magnetization and is therefore linked to hematite contribution, whereas the higher amount of Au yields higher Kerr ellipticity changes, which are associated with different absorption coefficients experienced by the two components of linearly polarized light. These results indicate the potential of these heterostructures for improved magneto-optical devices and their properties can be leveraged for highly sensitive sensors.

6.1 Introduction

Magneto-optical (MO) phenomena refer to changes in the polarization state of reflected (Kerr) or transmitted (Faraday) light, and can be used to extract valuable information on the electronic and spin structure of a material.[225,238] Since the first observations of MO effects, they have been used for the development of various applications, including data storage, optical modulators, and optical sensors, to name a few.[137,139,225,238,336,337] Among extensive efforts to enhance the performance of these devices by developing materials with larger MO activity, incorporation of photonic crystals into these devices has been a prominent option with encouraging results, as they have successfully demonstrated increased Faraday and Kerr rotation at the photonic band gap edge.[338–342] More recent work has focused on inclusion of plasmonic nanostructures to achieve enhanced MO activity.[143,237–240,242,343,344] These efforts have demonstrated the plausibility of such heterostructures for improved MO devices by experimentally showing increased Faraday or Kerr rotation and ellipticity in spectral regions matching the localized surface plasmon resonance (LSPR) of the included noble

metal, which has predominantly been Au nanoparticles, nanodiscs, or thin films. Analysis of the experimental results has isolated the contribution of the plasmonic material, displayed a clear contribution to the MO activity enhancement, whereas variations in sizes of the Au nanoparticles and distance between the Au layer and the MO material were also investigated. It was shown that while the LSPR intensity decreased for higher proximity of the two materials, the plasmonic contribution to MO enhancement was larger due to increased penetration of the electromagnetic field in the MO material.[143] Furthermore, for smaller separation of the plasmonic and magnetic materials the Kerr signal peak was narrower, whereas a broadening of the LSPR spectrum was observed, as well as a red-shift in the resonance wavelength.[237,239] On the other hand, changes in size of Au nanoparticles showed that as the LSPR peak red-shifted for larger nanoparticles, so did the Kerr rotation peak, which matched the absorption spectrum.[237] Additionally, it has been shown that increased nanoparticle size enhanced the Kerr signal.[239] This was attributed to larger area of contact between the two materials, thereby improving their interaction, based on the mechanism mentioned earlier. However, the Kerr ellipticity peak, while also changing, was red-shifted with respect to the absorption peak.[237] Not only do these results underline the connection of the MO activity enhancement to the presence of the plasmonic nanoparticles, but they also indicate the strong influence of the choice of architecture to achieving different results, hence providing different pathways to manipulate the response of these devices.

Popular materials for work on magneto-plasmonic heterostructures have previously included combinations of ferromagnetic materials with Au. Ferromagnetic materials are preferred as they demonstrate strong MO activity, orders of magnitude higher than that of paramagnetic and diamagnetic materials.[225,237] Common examples include cobalt, nickel, permalloy, bismuth-substituted yttrium iron garnet, magnetite (Fe_3O_4), and maghemite (γ-Fe_2O_3).[143,225,237–240,242,344,345] While magnetic metal films might demonstrate favorable MO response, they suffer from surface oxidation, which ultimately limits the device stability.[237,240] In addition, metal films could hinder good device performance due to high optical losses, resulting to significant broadening of LSPR.[225,240,346] Therefore, metal oxides are preferred due to their inherent stability and reduced optical losses.[240] They have been mostly combined with Au nanoparticles and films, due to the favorable properties of Au as a plasmonic material: apart from its stability in ambient environment, Au offers tunable response in the visible part of the spectrum for nanoparticles, extending to the infrared region for thin films, allowing for devices that can respond to various wavelengths by simple architecture modifications.[143,225,237–240,242,344,345] Typical architectures have been mostly limited to core-shell nanoparticles and layers of thin films, with limited work done in use of nanowire arrays for magneto-plasmonic devices.[235,347]

In this work, we focus on heterostructures composed of hematite (α-Fe_2O_3) nanowires and Au nanoparticles 10-20 nm in diameter. While the MO properties of hematite have not been as extensively investigated as those of magnetite and maghemite due to its lower magnetization value, some earlier work on observation of magnetic domains using MOKE have shown encouraging results.[348] Unexpectedly, magnetic domains were observed, with Kerr contrasts more pronounced than other samples, including magnetite, which was attributed to sub-lattice magnetization dominating Kerr

rotation, and not the resultant spin-canting moment. Hematite also demonstrates multiple favorable qualities, which make it suitable for implementation in a device. These include excellent chemical stability, low cost, nontoxicity, and abundance.[77–80,349] Furthermore, hematite is characterized by a relatively low absorption coefficient in the visible region of the spectrum as it possesses an indirect bandgap.[77–79] This is preferred in ferromagnetic materials implemented in magneto-plasmonic heterostructures, as a magnetic material with high optical loss would significantly broaden the LSPR spectrum.[240] This has presented as a common problem in magneto-plasmonic sensors and has recently led to the pursuit of alternative materials, such as Bi or Ce doped yttrium iron oxides.[240,350–355]

Investigation of hematite for its potential in magneto-plasmonic applications is not the only novelty of our work. Use of nanowires has been limited in magneto-plasmonic applications so far, and it can be used to leverage various beneficial properties, as 1-D nanostructures were previously seen to modify magnetic domain structures.[356–358] In earlier work, hematite nanowires and nanorods has demonstrated that the magnetic properties are different from that of bulk hematite.[119,120,126] While magnetocrystalline anisotropy favors magnetization along a preferred crystal orientation, shape anisotropy energy favors magnetization along the long axis of a nanorod. The two contributions are approximately equal and are therefore in competition, with resultant magnetization in a direction such that the total energy is minimized. However, if the long axis of a nanowire aligns with the magnetocrystalline direction, the magnetization will align with the long axis, which has been observed in hematite nanorods below the Morin transition temperature (T_M), resulting in a larger magnetic susceptibility value for $T < T_M$, under low applied magnetic field.[120] It should be noted that T_M has been observed to be much lower in hematite nanorods than in bulk hematite, and has been reported to decrease with smaller particle sizes.[120,359] Consequently, the incorporation of hematite nanowires could prove beneficial for magneto-plasmonic devices as the nanostructures have been shown to enhance its magnetic properties.

In this work we evaluate the potential of hematite/Au NP heterostructures to enhance MO effects via polar magneto-optical Kerr effect (MOKE) spectroscopy. We investigate the variation of Kerr rotation and Kerr ellipticity under different light excitations to observe any changes caused by LSPR excitation. This is monitored for various types of samples: bare hematite nanowires as the control sample, and hematite nanowires with increasing loading of Au NPs (1 wt% and 5 wt%) with and without post-annealing. We conclude that post-annealing of samples, which is done to enhance contact between the two materials, is crucial to good coupling between the two and ultimately leads to enhanced Kerr rotation and ellipticity which is not seen for as-grown samples. Furthermore, it is observed that while 1 wt% Au NP loading results in enhanced Kerr rotation, larger Kerr ellipticity enhancement is seen with higher loading of Au NPs (5 wt%) indicating that the higher content of Au has a larger effect on the amplitude of two components of linearly polarized light while they are traveling through the medium.

6.2 Results

6.2.1 Characteristics of α-Fe_2O_3/Au heterostructures

Figure 44 summarizes the structure of the samples used in this work. Figure 44a shows a top-view SEM image of the bare hematite nanowires. The nanowires show a preferential vertical growth, with diameter of approximately 50 nm. Figure 44b shows the hematite nanowires coated with Au NPs of sizes 10 – 20 nm. Coating with Au NPs appears to be even, with no uncoated regions and only a few regions more densely coated than others. Figure 44c shows a cross-sectional SEM image of the hematite nanowires, which appear to be approximately 800 nm long, and further establishes the vertical orientation of the nanowires, which will become important in magnetic measurements. Figure 44d shows the absorption spectra of the hematite/Au samples with various loadings of Au NPs, divided by the absorption spectrum of bare hematite to isolate the Au contribution. The absorption spectrum distinguishes between various weight percentages, as well as annealed and as-grown samples. The latter refers to post-annealing of samples which enhances the contact between Au NPs and hematite nanowires. As demonstrated in Figure 44d, the annealed sample with 1wt% Au NPs shows the highest absorption throughout the entire spectrum, while also showing a small peak centered at 530 nm which matches the LSPR of Au NPs of this size. It should be noted that the LSPR spectrum is red-shifted and broader compared to bare Au NPs due to the presence of hematite which alters the surrounding dielectric constant and dipolar coupling effects that appear for short separations between the two materials.[143] A faint LSPR peak can also be seen in the absorption spectrum for the annealed 5 wt% Au NP/hematite sample shown in figure 44e. Comparison with the as-grown samples with similar Au NP loading shows that absorption is reduced throughout the entire spectrum, whereas the LSPR peak is further quenched. This indicates that annealing not only improves contact between the two materials, but also the quality of Au NPs. Additionally, as Au NP loading increases, absorption decreases; this can be attributed to the reduced amount of hematite present when Au NP loading increases during fabrication, leading to lower number of sites where Au NPs can be deposited.

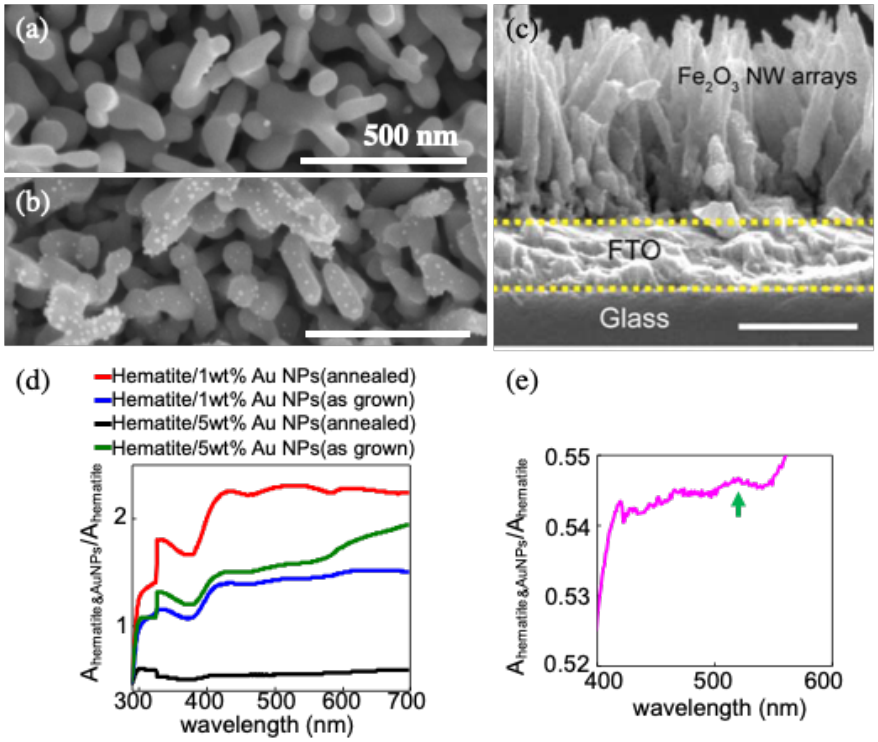

Figure 44. (a) Top-down SEM image of hematite nanowires. (b) Top-down SEM image of Au-coated hematite nanowires. (c) Cross-sectional SEM image of hematite nanowires. (d) Absorption spectra of Au-coated hematite nanowires, normalized by the absorption of bare hematite nanowires. Vertical dashed line indicates the expected spectral position of the LSPR peak. (e) Absorption spectrum of the annealed 5 wt% Au NP on hematite nanowires sample with the arrow indicating a faint LSPR peak.

6.2.2 Magnetic properties of α-Fe_2O_3 nanowires

Figure 45 introduces the magnetic properties of hematite nanowires with and without Au NPs. Figure 45a shows the variation of magnetization with temperature. The bare hematite nanowires used in this work is a canted antiferromagnet with Néel temperature of 950 K, resulting in weak ferromagnetism above 230 K, also seen in figure 45b. T_M is lower than bulk hematite, as expected, and the magnetic moment at room temperature is ~0.01μ_B.

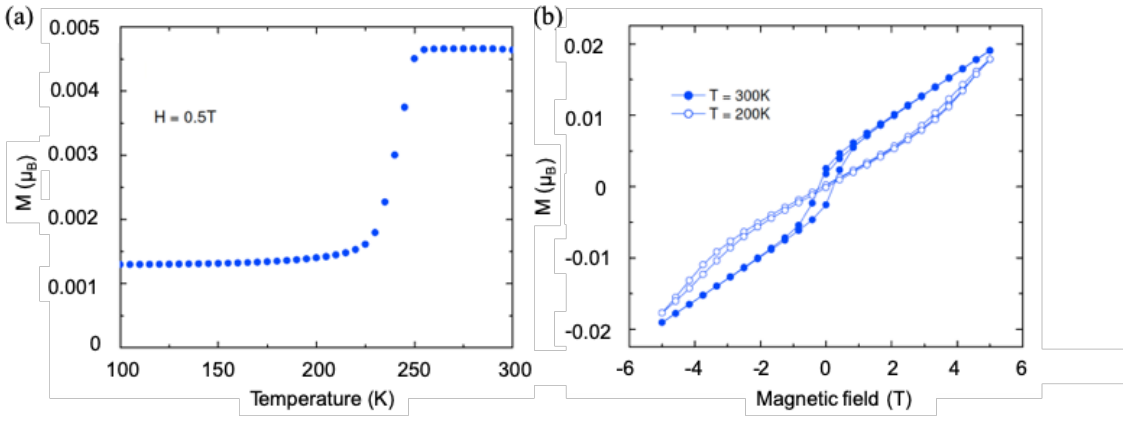

Figure 45. (a) Variation of magnetization of hematite nanowires with temperature. (b) Magnetization of hematite nanowires with applied magnetic field for 300 K and 200 K.

6.2.3 Complex Kerr rotation analysis of 1 wt% Au NP sample

Figure 46 summarizes the MOKE analysis conducted on the sample with 1 wt% Au NP loading. Figure 46a shows the variation of Kerr rotation and Kerr ellipticity with applied magnetic field for the sample that has undergone annealing. As expected, Kerr rotation increases with magnetic field, due to higher sample magnetization, resulting in a change of 0.025 as the applied field is varied from 0 T to 0.15 T. On the other hand, Kerr ellipticity shows a much smaller change as the applied field increases to 0.15 T, showing an increase of only 0.0025. The much smaller values of Kerr ellipticity is a consequence of the polarization analysis as explained in section 3.7: Kerr ellipticity is correlated with the 3rd harmonic of ω_{PEM} and, as described by equations 53 and 54, the signal intensity reaching the detector is much lower than for the 2nd harmonic. Furthermore, as Kerr ellipticity is a result of the appearance of p-polarized light as well as s-polarized light (since the incident light is s-polarized), it is a milder effect leading to smaller increase as the magnetic field increases to its maximum value. Figure 46b depicts the variation of Kerr rotation with excitation wavelength for the same sample, as well as bare hematite and the sample with 1 wt% Au NP loading that has not been annealed. The annealed sample demonstrates a clear enhancement in the region of the spectrum matching the LSPR of the Au NPs (~ 550 nm) indicating that coupling between hematite and Au is successful and the electric field enhancement caused by LSPR excitation leads to higher Kerr rotation. Figure 46c shows the variation of Kerr ellipticity with excitation wavelength for the three samples. As the origin of Kerr ellipticity lies within the different absorption coefficients experienced by the two components of linearly polarized light while traveling through the material, it is expected that the presence of Au NPs would impact its values.[135] As shown, the as-grown sample shows higher values in the high energy region (centered at ~ 510 nm), whereas the annealed sample shows a milder enhancement at longer wavelengths (around ~ 580 nm), which agrees with previous work where red-shift of the ellipticity peak with respect to the LSPR was observed due to the difference in wavelength dependence of optical and MO constants.[237]

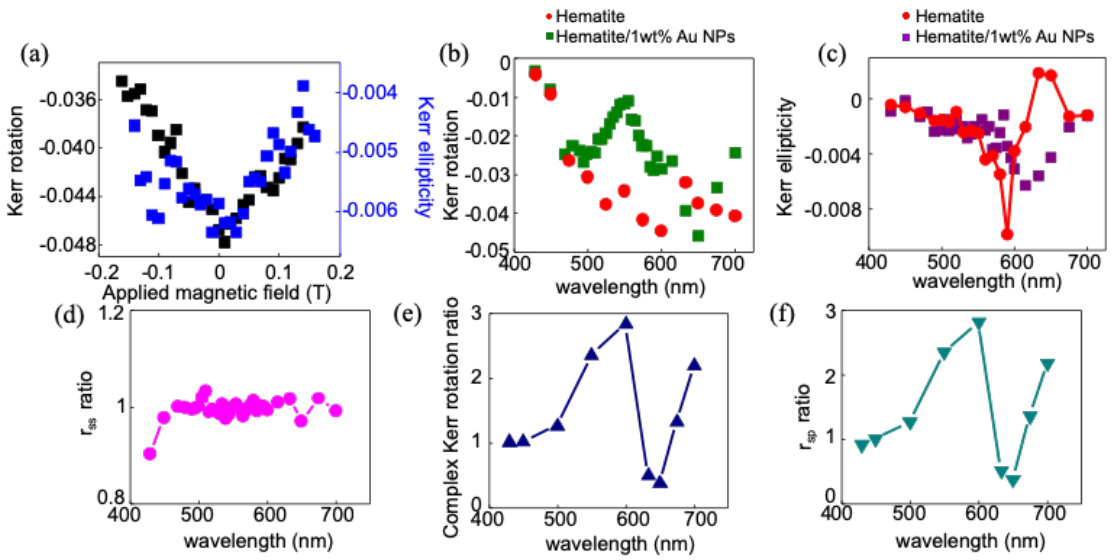

Figure 46. (a) Kerr rotation and Kerr ellipticity variation with applied magnetic field for 1 wt% Au NPs on hematite nanowires post-annealed at 300 °C. (b) Kerr rotation variation with incident light wavelength for 1 wt% Au NPs on hematite nanowires post-annealed at 300 °C and bare hematite nanowires. (c) Kerr ellipticity variation with incident light wavelength. (d) Reflectivity (r_{pp}) ratio for 1 wt% Au NPs on hematite nanowires post-annealed at 300 °C over bare hematite nanowires against incident light wavelength. (e) Complex Kerr rotation ratio values against incident light wavelength. (f) MO contribution of reflectivity (r_{sp}) ratio against incident light wavelength.

Further analysis of the results is done to confirm the origin of the enhancement. Kerr rotation (θ) and ellipticity (φ) are related to the elements of the reflectivity matrix as described in equations 30 through 32. The complex Kerr rotation is then given by the magnitude of expression 32, since both θ and φ are measured experimentally, and r_{pp} can be found by measuring the reflectivity of the sample at no applied magnetic field. The MO contribution (r_{sp}) can then be estimated by multiplying the magnitude of the complex Kerr rotation by r_{pp}. Figure 46d shows the measured r_{pp} at various wavelengths, divided by the measured r_{pp} of the bare hematite sample to isolate the Au NP contribution. The small dip in reflectivity centered at ~ 550 nm is consistent with LSPR excitation and matches the Kerr rotation enhancement seen in Figure 46b. As expected, the decrease is not very large due to the sparse distribution of the Au NPs shown in Figure 44b. Figure 46d can be contrasted with the reflectivity spectrum of the as-grown sample shown in Figure 47d, which does not show a reduction in reflectivity, further indicating that post-annealing enhances the quality of Au NPs. The ratio of complex Kerr rotation of the annealed sample with 1wt% Au NPs against the bare hematite sample is plotted against excitation wavelength in Figure 46e. It can be seen that the complex Kerr rotation is higher than 1 for the region ~500 – 600 nm, indicating that the presence of Au NPs improves the MO effects in that region, reaching three-fold enhancement at 600 nm. This is further validated in Figure 46f which depicts the ratio of r_{sp} of the same sample over bare hematite and it follows the same trend, demonstrating the enhancement of the pure MO contribution due

to Au NPs. These results are contrasted with the ratios including the as-grown 1wt% Au NP sample shown in Figure 47e and Figure 47f, which do not surpass values of 1, indicating that no enhancement is achieved due to the presence of Au NPs in this case.

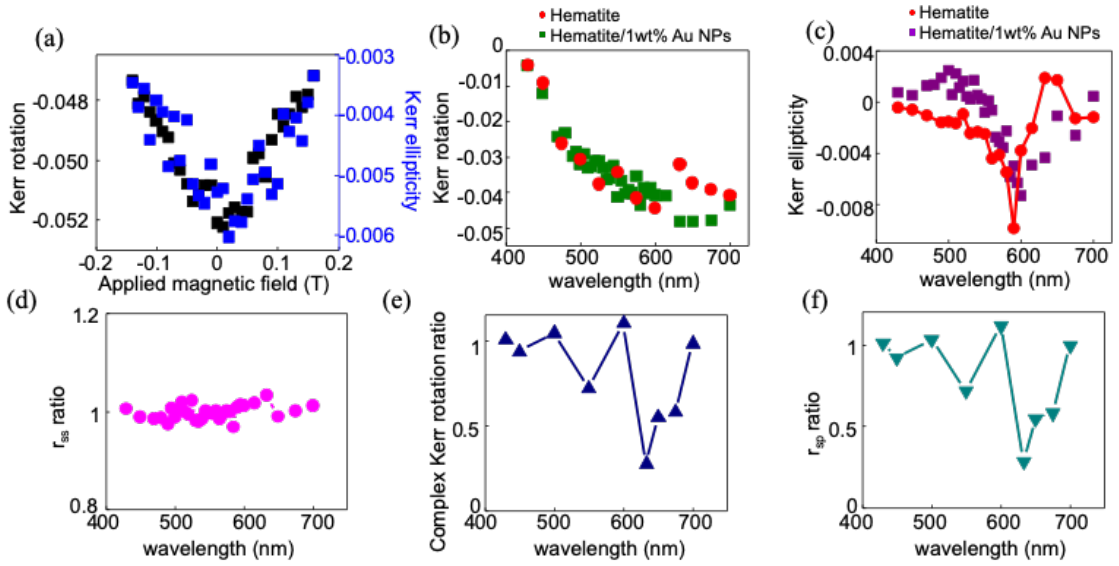

Figure 47. (a) Kerr rotation and Kerr ellipticity variation with applied magnetic field for 1 wt% Au NPs on hematite nanowires (as-grown). (b) Kerr rotation variation with incident light wavelength for 1 wt% Au NPs on hematite nanowires and bare hematite nanowires. (c) Kerr ellipticity variation with incident light wavelength. (d) Reflectivity (r_{pp}) ratio for 1 wt% Au NPs on hematite nanowires over bare hematite nanowires against incident light wavelength. (e) Complex Kerr rotation ratio values against incident light wavelength. (f) MO contribution of reflectivity (r_{sp}) ratio against incident light wavelength.

6.2.4 Complex Kerr rotation analysis of 5 wt% Au NP sample

Figure 48 summarizes the results obtained from the samples with 5 wt% Au NP loading. Figure 48a shows the variation of Kerr rotation and Kerr ellipticity with applied magnetic field. As with the previous samples, Kerr rotation increases with applied magnetic field and hence, sample magnetization. The change of Kerr rotation with increasing applied magnetic field is smaller for this sample compared to the one with 1 wt% Au NP loading, whereas Kerr ellipticity changes by 0.007 in this case. Figure 48b demonstrates the Kerr rotation enhancement seen in the annealed 5 wt% Au NP. As with the previous samples, the as-grown sample does not show any discernible enhancement in Kerr rotation values, whereas a clear peak emerges at the spectral region matching the LSPR for the annealed sample, demonstrating that once more the enhanced electric field due to the LSPR excitations enhances MO effects in hematite. Figure 48c depicts the Kerr ellipticity values for different excitation wavelengths. A striking result is seen here, with a very strong peak centered at ~ 590 nm emerging for the annealed 5 wt% Au NP sample, which was not seen in the case of the 1 wt% Au NP sample. This Kerr ellipticity

enhancement is again a consequence of coupling between the two materials in the heterostructure, with the higher Au NP loading leading to a larger enhancement. This could be because higher Au NP leads to a larger effect on the absorption coefficients experienced by the two components of linearly polarized light, resulting in larger modifications. Moreover, higher loading has the possibility of producing larger Au NPs, which have been previously associated with Kerr ellipticity enhancement and red-shifting of the ellipticity enhancement peak.[143,237] Nevertheless, any enhancement in Kerr rotation or ellipticity is absent in the as-grown 5 wt% Au NP sample, further establishing that lack of annealing prevents successful coupling between Au NPs and hematite nanowires.

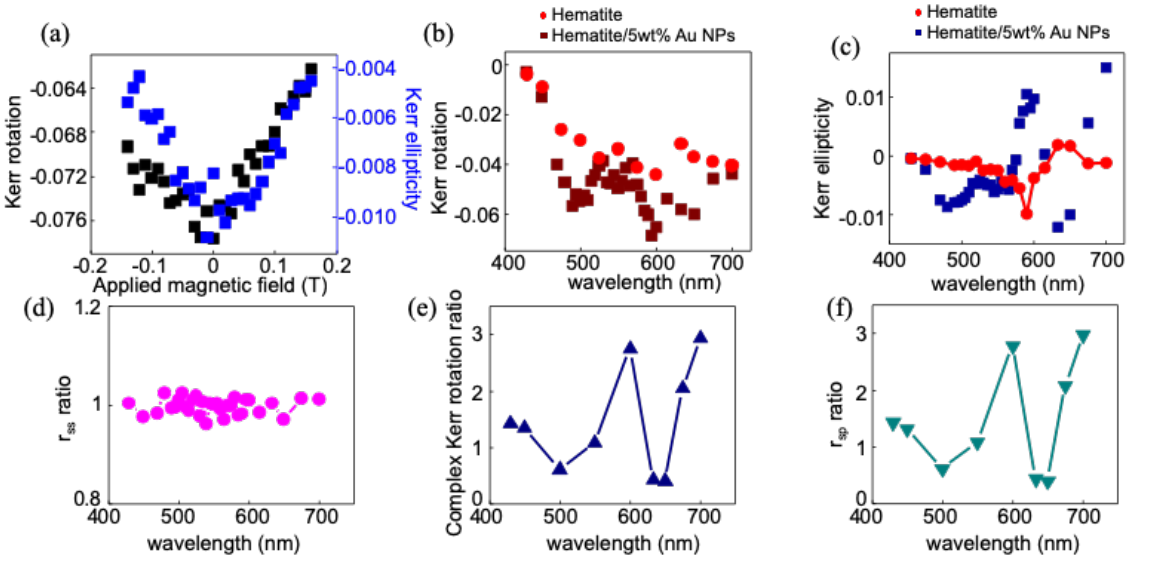

Figure 48. (a) Kerr rotation and Kerr ellipticity variation with applied magnetic field for 5 wt% Au NPs on hematite nanowires post-annealed at 300 °C. (b) Kerr rotation variation with incident light wavelength for 5 wt% Au NPs on hematite nanowires post-annealed at 300 °C and bare hematite nanowires. (c) Kerr ellipticity variation with incident light wavelength. (d) Reflectivity (r_{pp}) ratio for 5 wt% Au NPs on hematite nanowires post-annealed at 300 °C over bare hematite nanowires against incident light wavelength. (e) Complex Kerr rotation ratio values against incident light wavelength. (f) MO contribution of reflectivity (r_{sp}) ratio against incident light wavelength.

Figure 48d shows the reflectivity (r_{pp}) values of the annealed 5 wt% sample, which like figure 46d, is characterized by a small dip in reflectivity centered at ~ 550 nm, matching the LSPR of Au NPs. Similar to the previous case, the as-grown sample shows no specific trend, as seen in Figure 49a. Figure 48e shows the variation of the annealed 5 wt% Au NP/no Au NP ratio of the complex Kerr rotation with wavelength. The trend is similar in this case, with a four-fold enhancement of complex Kerr rotation and r_{sp} achieved at 600 nm. The higher enhancement compared to the 1wt% Au NP sample is indicative of a positive correlation on the amount of Au NPs present. Similar to the previous case, the as-grown 5 wt% Au NP sample does not demonstrate significant enhancement of MO effects, as demonstrated in figure 49.

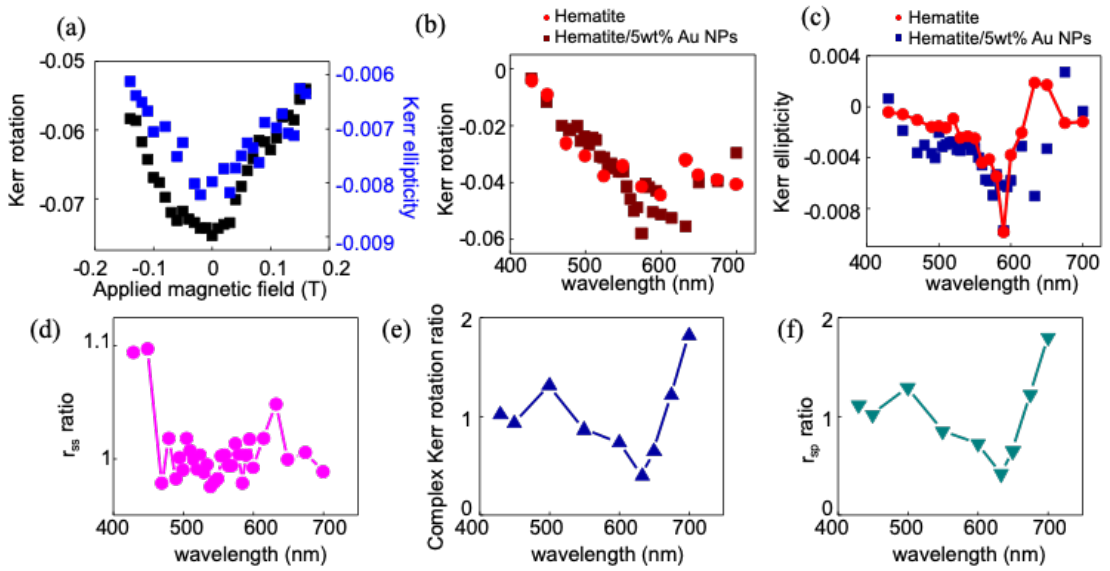

Figure 49. (a) Kerr rotation and Kerr ellipticity variation with applied magnetic field for 5 wt% Au NPs on hematite nanowires (as-grown). (b) Kerr rotation variation with incident light wavelength for 5 wt% Au NPs on hematite nanowires and bare hematite nanowires. (c) Kerr ellipticity variation with incident light wavelength. (d) Reflectivity (r_{pp}) ratio for 5 wt% Au NPs on hematite nanowires over bare hematite nanowires against incident light wavelength. (e) Complex Kerr rotation ratio values against incident light wavelength. (f) MO contribution of reflectivity (r_{sp}) ratio against incident light wavelength.

6.3 Conclusion

Hematite is a novel material in the area of magneto-plasmonics, which offers benefits such as ease of fabrication, high abundance, and low cost, while synthesis of hematite nanowires enhances its magnetic properties via magnetocrystalline and shape anisotropy. The incorporation of hematite in magneto-plasmonic devices provides further benefits due to the extraordinary stability of hematite in ambient conditions, as well as its low absorption coefficient which is expected to minimize optical losses. Au has been the most common plasmonic material in magneto-plasmonic devices due to its superior plasmonic properties and impressive stability, and it has been implemented both as a thin film or in nanoparticle form.

In this work, the potential combination of hematite nanowires and Au NPs for magneto-plasmonic applications is investigated via MOKE studies, with encouraging results. Complex Kerr rotation enhancement is observed for hematite nanowires decorated with 1 wt% and 5 wt% Au NPs if the samples have undergone post-annealing, as it improves contact between the materials and the plasmonic properties of the Au NPs. A more interesting result is the difference caused by changes in Au NP loading of the sample. Since samples with increasing Au NP content showed reduced hematite content, it was observed that the 1 wt% Au NP sample, with higher hematite content, showed greater changes in the real component of Kerr rotation upon LSPR excitation, which is associated

with sample magnetization and higher sample thickness. On the other hand, the 5 wt% Au NP sample showed larger modifications of Kerr ellipticity, which is caused by the two components of the linearly polarized light experiencing different absorption coefficients, an effect that appears to be enhanced when LSPR is excited. It is concluded that while LSPR excitation, associated with increased local electric field, leads to complex Kerr rotation enhancement, the presence of more Au NPs favors Kerr ellipticity enhancement as coupling between Au NPs leads to stronger local electric field enhancement, whereas fewer Au NPs lead to more prominent Kerr rotation enhancement. These results indicate the possibility of tuning the properties of these heterostructures, not only in terms of wavelength response by modifying the size of the Au NPs, but also by adjusting the amount of Au NPs present selective modifications of Kerr rotation or Kerr ellipticity can be achieved. Therefore, these underline the promise of these heterostructures in highly responsive sensing applications.

6.4 Experimental section

Hematite nanowires are prepared on indium tin oxide (ITO)-coated glass by hydrothermal growth, followed by air annealing as described in [360]. The morphology of the samples is controlled via modification of growth conditions and encapsulation techniques, as outlined in reference [361]. The Au NPs are synthesized by chemical bath deposition, as described in [362]; the hematite nanowire surface is chemically modified with thiol groups and the nanowires are immersed in aqueous solution of Au NPs to decorate the nanowires with Au NPs. Samples can undergo post-annealing at 300 °C to enhance contact between hematite nanowires and Au NPs.

Magneto-optical Kerr effect (MOKE) measurements are done using a pulsed supercontinuum source (NKT Photonics). The wavelength is swept from 430 nm to 700 nm, and the repetition rate is kept constant at 77.9 MHz. The signal is modulated at 50 kHz via a photo-elastic modulator, and the Kerr rotation and ellipticity are resolved using lock-in amplifiers with a resolution of 0.2·μrad.[363,364] The reflectivity of the sample is recorded by a photodiode in the collection path.

Chapter 7

Conclusions

In this dissertation, the importance of optical spectroscopy as characterization tool for nanostructured materials and interfaces is underlined through a variety of measurements, which result in evaluating the potential of these materials in devices, ranging from photovoltaic applications to sensors.

The potential of hybrid PVSK thin films as LSCs was demonstrated via photoluminescence and electrical measurements. PVSK LSCs achieve high optical efficiencies varying from 15 % to 29 %, while being operational after 7 weeks of storage in ambient conditions. This is an impressive result, and the outstanding performance of PVSK LSCs is attributed to the high quantum yield and high refractive index of PVSK thin films, which negates the effect of self-absorption demonstrated by the thin films. Furthermore, due to the emission of PVSK being centered at 780 nm, it matches well the absorption spectrum of silicon PV cells, enhancing their photovoltaic performance. In addition, the durability of these LSCs indicates that while the electrical properties of PVSK deteriorate rapidly, the optical properties are preserved for longer, making the possibility of stable all optical PVSK-based devices realistic.

As PVSK thin films have been on the forefront of photovoltaic research, which has so far encompassed a vast number of ETL materials and morphologies, a systematic study of PVSK thin film interaction with ZnO of various morphologies was conducted to understand the impact of the ETL morphology on the properties of the PVSK thin film. It was demonstrated that planar ZnO acted most efficiently as ETL, as indicated by photoluminescence studies which showed signs of electron extraction. On the other hand, ZnO substrates with increased surface roughness, and most strikingly, ZnO nanowires resulted in photoluminescence enhancement, up to 30 thousand times, of the PVSK thin films. This was associated with reduced carrier extraction and increased exciton binding energy of the PVSK layer, a consequence of grain separation in the PVSK thin films due to the high surface roughness of the substrate, which ultimately confined photogenerated excitons within grains and inhibited efficient charge carrier transport across the PVSK thin film, thereby limiting charge transfer to the underlying ZnO. This result encouraged the implementation of roughened substrates with PVSK thin films in applications where high quantum yield and emission is the goal.

In addition to investigating PVSK/ZnO interfaces for photovoltaic applications, the interface of Au NPs with hematite nanowires was also studied by means of magneto-optical Kerr effect spectroscopy. It was demonstrated that excitation of the LSPR of Au NPs enhances the MO effects demonstrated by hematite nanowires, and in particular, adding a limited amount of Au NPs leads to larger changes in Kerr rotation of reflected light, whereas increasing the amount of Au NPs further causes larger modifications in the Kerr ellipticity of reflected light. This result encourages implementation of such interfaces in devices that would leverage the enhanced MO effects of hematite nanowires after

incorporation of Au NPs. This work could be further expanded in the future by investigating the impact of the MO effects of hematite on the LSPR of Au NPs. This could lead to narrower LSPR spectra that could be implemented in gas sensors which would be highly sensitive to the refractive index of the surrounding environment, as any change in a narrow LSPR due to changes of the surrounding medium would be more easily observed.

References

[1] Nikolaidou K, Sarang S, Hoffman C, Mendewala B, Ishihara H, Lu J Q, Ilan B, Tung V and Ghosh S 2016 Hybrid Perovskite Thin Films as Highly Efficient Luminescent Solar Concentrators *Adv. Opt. Mater.* **4** 2126–32

[2] Nikolaidou K, Sarang S, Martin D, Tung V, Lu J Q and Ghosh S 2018 Tuning Excitonic Properties of Pure and Mixed Halide Perovskite Thin Films via Interfacial Engineering *Adv. Mater. Interfaces* **5** 1800209

[3] Leijtens T, Eperon G E, Noel N K, Habisreutinger S N, Petrozza A and Snaith H J 2015 Stability of Metal Halide Perovskite Solar Cells *Adv. Energy Mater.* **5** 1500963

[4] De Wolf S, Holovsky J, Moon S-J, Löper P, Niesen B, Ledinsky M, Haug F-J, Yum J-H and Ballif C 2014 Organometallic Halide Perovskites: Sharp Optical Absorption Edge and Its Relation to Photovoltaic Performance *J. Phys. Chem. Lett.* **5** 1035–9

[5] Stoumpos C C, Malliakas C D and Kanatzidis M G 2013 Semiconducting Tin and Lead Iodide Perovskites with Organic Cations: Phase Transitions, High Mobilities, and Near-Infrared Photoluminescent Properties *Inorg. Chem.* **52** 9019–38

[6] Umari P, Mosconi E and De Angelis F 2015 Relativistic GW calculations on CH3NH3PbI3 and CH3NH3SnI3 Perovskites for Solar Cell Applications *Sci. Rep.* **4** 4467

[7] Menéndez-Proupin E, Palacios P, Wahnón P and Conesa J C 2014 Self-consistent relativistic band structure of the CH 3 NH 3 PbI 3 perovskite *Phys. Rev. B* **90** 045207

[8] Brenner T M, Egger D A, Kronik L, Hodes G and Cahen D 2016 Hybrid organic—

inorganic perovskites: low-cost semiconductors with intriguing charge-transport properties *Nat. Rev. Mater.* **1** 15007

[9] Even J, Pedesseau L, Jancu J-M and Katan C 2013 Importance of Spin–Orbit Coupling in Hybrid Organic/Inorganic Perovskites for Photovoltaic Applications *J. Phys. Chem. Lett.* **4** 2999–3005

[10] Giorgi G, Fujisawa J-I, Segawa H and Yamashita K 2013 Small Photocarrier Effective Masses Featuring Ambipolar Transport in Methylammonium Lead Iodide Perovskite: A Density Functional Analysis *J. Phys. Chem. Lett.* **4** 4213–6

[11] Guo Y, Yaffe O, Paley D W, Beecher A N, Hull T D, Szpak G, Owen J S, Brus L E and Pimenta M A 2017 Interplay between organic cations and inorganic framework and incommensurability in hybrid lead-halide perovskite CH 3 NH 3 PbBr 3 *Phys. Rev. Mater.* **1** 042401

[12] Duan H-S, Zhou H, Chen Q, Sun P, Luo S, Song T-B, Bob B and Yang Y 2015 The identification and characterization of defect states in hybrid organic–inorganic perovskite photovoltaics *Phys. Chem. Chem. Phys.* **17** 112–6

[13] Samiee M, Konduri S, Ganapathy B, Kottokkaran R, Abbas H A, Kitahara A, Joshi P, Zhang L, Noack M and Dalal V 2014 Defect density and dielectric constant in perovskite solar cells *Appl. Phys. Lett.* **105** 153502

[14] Baumann A, Väth S, Rieder P, Heiber M C, Tvingstedt K and Dyakonov V 2015 Identification of Trap States in Perovskite Solar Cells *J. Phys. Chem. Lett.* **6** 2350–4

[15] deQuilettes D W, Vorpahl S M, Stranks S D, Nagaoka H, Eperon G E, Ziffer M E, Snaith H J and Ginger D S 2015 Solar cells. Impact of microstructure on local carrier

lifetime in perovskite solar cells. *Science* **348** 683–6

[16] Buin A, Pietsch P, Xu J, Voznyy O, Ip A H, Comin R and Sargent E H 2014 Materials Processing Routes to Trap-Free Halide Perovskites *Nano Lett.* **14** 6281–6

[17] Zhang W, Saliba M, Moore D T, Pathak S K, Hörantner M T, Stergiopoulos T, Stranks S D, Eperon G E, Alexander-Webber J A, Abate A, Sadhanala A, Yao S, Chen Y, Friend R H, Estroff L A, Wiesner U and Snaith H J 2015 Ultrasmooth organic–inorganic perovskite thin-film formation and crystallization for efficient planar heterojunction solar cells *Nat. Commun.* **6** 6142

[18] Saba M, Cadelano M, Marongiu D, Chen F, Sarritzu V, Sestu N, Figus C, Aresti M, Piras R, Geddo Lehmann A, Cannas C, Musinu A, Quochi F, Mura A and Bongiovanni G 2014 Correlated electron-hole plasma in organometal perovskites *Nat. Commun.* **5** 5049

[19] Geng W, Zhang L, Zhang Y-N, Lau W-M and Liu L-M 2014 First-Principles Study of Lead Iodide Perovskite Tetragonal and Orthorhombic Phases for Photovoltaics *J. Phys. Chem. C* **118** 19565–71

[20] Huang H, Susha A S, Kershaw S V, Hung T F and Rogach A L 2015 Control of Emission Color of High Quantum Yield CH3NH3PbBr3 Perovskite Quantum Dots by Precipitation Temperature. *Adv. Sci. (Weinheim, Baden-Wurttemberg, Ger.* **2** 1500194

[21] Stranks S D, Burlakov V M, Leijtens T, Ball J M, Goriely A and Snaith H J 2014 Recombination Kinetics in Organic-Inorganic Perovskites: Excitons, Free Charge, and Subgap States *Phys. Rev. Appl.* **2** 034007

[22] Zhu H, Fu Y, Meng F, Wu X, Gong Z, Ding Q, Gustafsson M V., Trinh M T, Jin S

and Zhu X-Y 2015 Lead halide perovskite nanowire lasers with low lasing thresholds and high quality factors *Nat. Mater.* **14** 636–42

[23] Cho H, Jeong S-H, Park M-H, Kim Y-H, Wolf C, Lee C-L, Heo J H, Sadhanala A, Myoung N, Yoo S, Im S H, Friend R H and Lee T-W 2015 Overcoming the electroluminescence efficiency limitations of perovskite light-emitting diodes. *Science* **350** 1222–5

[24] Özgür Ü, Alivov Y I, Liu C, Teke A, Reshchikov M A, Doğan S, Avrutin V, Cho S-J and Morkoç H 2005 A comprehensive review of ZnO materials and devices *J. Appl. Phys.* **98** 041301

[25] Kogure T and Bando Y 1998 Formation of ZnO nanocrystallites on ZnS surfaces by electron beam irradiation *J. Electron Microsc. (Tokyo).* **47** 135–41

[26] Bates C H, White W B and Roy R 1962 New High-Pressure Polymorph of Zinc Oxide *Science* **137** 993–4

[27] Iwanaga H, Kunishige A and Takeuchi S 2000 Anisotropic thermal expansion in wurtzite-type crystals *J. Mater. Sci.* **35** 2451–4

[28] Varshni Y P 1967 Temperature dependence of the energy gap in semiconductors *Physica* **34** 149–54

[29] Srikant V and Clarke D R 1998 On the optical band gap of zinc oxide *J. Appl. Phys.* **83** 5447–51

[30] Mang A, Reimann K and Rübenacke S 1995 Band gaps, crystal-field splitting, spin-orbit coupling, and exciton binding energies in ZnO under hydrostatic pressure *Solid State Commun.* **94** 251–4

[31] Look D C, Reynolds D C, Sizelove J R, Jones R L, Litton C W, Cantwell G and

Harsch W C 1998 Electrical properties of bulk ZnO *Solid State Commun.* **105** 399–401

[32] Albrecht J D, Ruden P P, Limpijumnong S, Lambrecht W R L and Brennan K F 1999 High field electron transport properties of bulk ZnO *J. Appl. Phys.* **86** 6864–7

[33] Kohan A F, Ceder G, Morgan D and Van de Walle C G 2000 First-principles study of native point defects in ZnO *Phys. Rev. B* **61** 15019–27

[34] Van de Walle C G 2000 Hydrogen as a Cause of Doping in Zinc Oxide *Phys. Rev. Lett.* **85** 1012–5

[35] Rodnyi P A and Khodyuk I V. Optical and luminescence properties of zinc oxide (Review) *Opt. Spectrosc.* **111** 776–85

[36] Meyer B K, Alves H, Hofmann D M, Kriegseis W, Forster D, Bertram F, Christen J, Hoffmann A, Straßburg M, Dworzak M, Haboeck U and Rodina A V. 2004 Bound exciton and donor–acceptor pair recombinations in ZnO *Phys. status solidi* **241** 231–60

[37] Fonoberov V A, Alim K A, Balandin A A, Xiu F and Liu J 2006 Photoluminescence investigation of the carrier recombination processes in ZnO quantum dots and nanocrystals *Phys. Rev. B* **73** 165317

[38] Kumar N, Kaur R and Mehra R M 2007 Photoluminescence studies in sol–gel derived Zno films *J. Lumin.* **126** 784–8

[39] Børseth T M, Svensson B G, Kuznetsov A Y, Klason P, Zhao Q X and Willander M 2006 Identification of oxygen and zinc vacancy optical signals in ZnO *Appl. Phys. Lett.* **89** 262112

[40] Giles N C, Xu C, Callahan M J, Wang B, Neal J S and Boatner L A 2006 Effects

of phonon coupling and free carriers on band-edge emission at room temperature in n-type ZnO crystals *Appl. Phys. Lett.* **89** 251906

[41] Zhang S G, Wen L, Li J L, Gao F L, Zhang X W, Li L H and Li G Q 2014 Plasmon-enhanced ultraviolet photoluminescence from highly ordered ZnO nanorods/graphene hybrid structure decorated with Au nanospheres *J. Phys. D. Appl. Phys.* **47** 495103

[42] Chen H, Gu S, Tang K, Zhu S, Zhu Z, Ye J, Zhang R and Zheng Y 2011 Origins of green band emission in high-temperature annealed N-doped ZnO *J. Lumin.* **131** 1189–92

[43] Laio R, Vlasenko L S and Vlasenko P M 2008 No Title *J. Appl. Phys.* **103 P** 12379

[44] Leiter F H, Alves H R, Hofstaetter A, Hofmann D M and Meyer B K 2001 The Oxygen Vacancy as the Origin of a Green Emission in Undoped ZnO *Phys. status solidi* **226** R4–5

[45] Cao B, Cai W and Zeng H 2006 Temperature-dependent shifts of three emission bands for ZnO nanoneedle arrays *Appl. Phys. Lett.* **88** 161101

[46] Berhe T A, Su W-N, Chen C-H, Pan C-J, Cheng J-H, Chen H-M, Tsai M-C, Chen L-Y, Dubale A A and Hwang B-J 2016 Organometal halide perovskite solar cells: degradation and stability *Energy Environ. Sci.* **9** 323–56

[47] Kojima A, Teshima K, Shirai Y and Miyasaka T 2009 Organometal Halide Perovskites as Visible-Light Sensitizers for Photovoltaic Cells *J. Am. Chem. Soc.* **131** 6050–1

[48] Etgar L, Gao P, Xue Z, Peng Q, Chandiran A K, Liu B, Nazeeruddin M K and Grätzel M 2012 Mesoscopic $CH_3NH_3PbI_3/TiO_2$ Heterojunction Solar Cells *J.*

Am. Chem. Soc. **134** 17396–9

[49] Kim H-S, Lee C-R, Im J-H, Lee K-B, Moehl T, Marchioro A, Moon S-J, Humphry-Baker R, Yum J-H, Moser J E, Grätzel M and Park N-G 2012 Lead Iodide Perovskite Sensitized All-Solid-State Submicron Thin Film Mesoscopic Solar Cell with Efficiency Exceeding 9% *Sci. Rep.* **2** 591

[50] Lee M M, Teuscher Joël, Miyasaka T, Murakami T N and Snaith H J 2012 Efficient Hybrid Solar Cells Based on Meso-Superstructured Organometal Halide Perovskites *Science (80-.).* **338** 643–7

[51] Heo J H, Im S H, Noh J H, Mandal T N, Lim C-S, Chang J A, Lee Y H, Kim H, Sarkar A, Nazeeruddin M K, Grätzel M and Seok S Il 2013 Efficient inorganic–organic hybrid heterojunction solar cells containing perovskite compound and polymeric hole conductors *Nat. Photonics* **7** 486–91

[52] Mitzi D B, Feild C A, Harrison W T A and Guloy A M 1994 Conducting tin halides with a layered organic-based perovskite structure *Nature* **369** 467–9

[53] Green M A, Ho-Baillie A and Snaith H J 2014 The emergence of perovskite solar cells *Nat. Photonics* **8** 506–14

[54] Burschka J, Pellet N, Moon S-J, Humphry-Baker R, Gao P, Nazeeruddin M K and Grätzel M 2013 Sequential deposition as a route to high-performance perovskite-sensitized solar cells *Nature* **499** 316–9

[55] Green M A, Emery K, Hishikawa Y, Warta W and Dunlop E D 2015 Solar cell efficiency tables (Version 45) *Prog. Photovoltaics Res. Appl.* **23** 1–9

[56] Christians J A, Manser J S and Kamat P V. 2015 Best Practices in Perovskite Solar Cell Efficiency Measurements. Avoiding the Error of *Making Bad Cells Look Good*

J. Phys. Chem. Lett. **6** 852–7

[57] Saliba M, Matsui T, Seo J-Y, Domanski K, Correa-Baena J-P, Nazeeruddin M K, Zakeeruddin S M, Tress W, Abate A, Hagfeldt A and Grätzel M 2016 Cesium-containing triple cation perovskite solar cells: improved stability, reproducibility and high efficiency *Energy Environ. Sci.* **9** 1989–97

[58] You J, Meng L, Song T-B, Guo T-F, Yang Y, Chang W-H, Hong Z, Chen H, Zhou H, Chen Q, Liu Y, De Marco N and Yang Y 2016 Improved air stability of perovskite solar cells via solution-processed metal oxide transport layers *Nat. Nanotechnol.* **11** 75–81

[59] D'Innocenzo V, Grancini G, Alcocer M J P, Kandada A R S, Stranks S D, Lee M M, Lanzani G, Snaith H J and Petrozza A 2014 Excitons versus free charges in organo-lead tri-halide perovskites *Nat. Commun.* **5** 3586

[60] Tanaka K, Takahashi T, Ban T, Kondo T, Uchida K and Miura N 2003 Comparative study on the excitons in lead-halide-based perovskite-type crystals CH3NH3PbBr3 CH3NH3PbI3 *Solid State Commun.* **127** 619–23

[61] Hirasawa M, Ishihara T and Goto T 1994 Exciton Features in 0-, 2-, and 3-Dimensional Networks of $[PbI_6]^{4-}$ Octahedra *J. Phys. Soc. Japan* **63** 3870–9

[62] Yamada, Yasuhiro; Nakamura, Toru; Endo M and Wakamiya, Atsushi; Kanemitsu Y 2015 Photoelectronic Responses in Solution-Processed Perovskite CH[3]NH[3]PbI[3] Solar Cells Studied by Photoluminescence and Photoabsorption Spectroscopy *IEEE J. Photovoltaics* **5** 401–5

[63] Miyata A, Mitioglu A, Plochocka P, Portugall O, Wang J T-W, Stranks S D, Snaith H J and Nicholas R J 2015 Direct measurement of the exciton binding energy and

effective masses for charge carriers in organic–inorganic tri-halide perovskites *Nat. Phys.* **11** 582–7

[64] Elward J M and Chakraborty A 2015 Effect of Heterojunction on Exciton Binding Energy and Electron–Hole Recombination Probability in CdSe/ZnS Quantum Dots *J. Chem. Theory Comput.* **11** 462–71

[65] Degani M H and Farias G A 1990 Exciton binding energy in type-II heterojunctions *Phys. Rev. B* **42** 11701–7

[66] Chen Z, Yu C, Shum K, Wang J J, Pfenninger W, Vockic N, Midgley J and Kenney J T 2011 Photoluminescence study of polycrystalline CsSnI 3 thin films: Determination of exciton binding energy *J. Lumin.* **132** 345–9

[67] Cingolani R, Calcagnile L, Colí G, Rinaldi R, Lomoscolo M, DiDio M, Franciosi A, Vanzetti L, LaRocca G C and Campi D 1996 Radiative recombination processes in wide-band-gap II–VI quantum wells: the interplay between excitons and free carriers *J. Opt. Soc. Am. B* **13** 1268

[68] Zheng K, Zhu Q, Abdellah M, Messing M E, Zhang W, Generalov A, Niu Y, Ribaud L, Canton S E and Pullerits T 2015 Exciton Binding Energy and the Nature of Emissive States in Organometal Halide Perovskites *J. Phys. Chem. Lett.* **6** 2969–75

[69] Sarang S, Ishihara H, Chen Y-C, Lin O, Gopinathan A, Tung V C and Ghosh S 2016 Low temperature excitonic spectroscopy and dynamics as a probe of quality in hybrid perovskite thin films *Phys. Chem. Chem. Phys.* **18** 28428–33

[70] Sun Y, Qian C, Peng K, Bai Z, Tang J, Zhao Y, Wu S, Ali H, Song F, Zhong H and Xu X 2016 Recombination processes in CuInS2/ZnS nanocrystals during steady-

state photoluminescence *Cit. Appl. Phys. Lett.* **108** 41106

[71] Debije M G and Verbunt P P C 2012 Thirty Years of Luminescent Solar Concentrator Research: Solar Energy for the Built Environment *Adv. Energy Mater.* **2** 12–35

[72] Weber W H and Lambe J 1976 Luminescent greenhouse collector for solar radiation *Appl. Opt.* **15** 2299

[73] Goetzberger A and Greube W 1977 Solar energy conversion with fluorescent collectors *Appl. Phys.* **14** 123–39

[74] Shcherbatyuk G V., Inman R H, Wang C, Winston R and Ghosh S 2010 Viability of using near infrared PbS quantum dots as active materials in luminescent solar concentrators *Appl. Phys. Lett.* **96** 191901

[75] Sholin V, Olson J D and Carter S A 2007 Semiconducting polymers and quantum dots in luminescent solar concentrators for solar energy harvesting *J. Appl. Phys.* **101** 123114

[76] Nikolaidou K, Sarang S and Ghosh S 2019 Nanostructured photovoltaics *Nano Futur.* **3** 012002

[77] Sivula K, Le Formal F and Grätzel M 2011 Solar Water Splitting: Progress Using Hematite (α-Fe2O3) Photoelectrodes *ChemSusChem* **4** 432–49

[78] Ling Y, Wang G, Wheeler D A, Zhang J Z and Li Y 2011 Sn-Doped Hematite Nanostructures for Photoelectrochemical Water Splitting *Nano Lett.* **11** 2119–25

[79] Wang L, Zhou X, Nguyen N T and Schmuki P 2015 Plasmon-Enhanced Photoelectrochemical Water Splitting Using Au Nanoparticles Decorated on Hematite Nanoflake Arrays *ChemSusChem* **8** 618–22

[80] Wang L, Hu H, Nguyen N T, Zhang Y, Schmuki P and Bi Y 2017 Plasmon-induced hole-depletion layer on hematite nanoflake photoanodes for highly efficient solar water splitting *Nano Energy* **35** 171–8

[81] Bødker F, Hansen M F, Koch C B, Lefmann K and Mørup S 2000 Magnetic properties of hematite nanoparticles *Phys. Rev. B* **61** 6826–38

[82] Appel E, Hoffmann V and Soffel H C 1990 Magneto-optical Kerr effect in (titano)magnetite, pyrrhotite and hematite *Phys. Earth Planet. Inter.* **65** 36–42

[83] Sivula K, Zboril R, Le Formal F, Robert R, Weidenkaff A, Tucek J, Frydrych J and Grä M Photoelectrochemical Water Splitting with Mesoporous Hematite Prepared by a Solution-Based Colloidal Approach

[84] Cornell R M and Schwertmann U 2003 *The iron oxides : structure, properties, reactions, occurrences, and uses* (Wiley-VCH)

[85] Sanson A, Mathon O and Pascarelli S 2014 Local vibrational dynamics of hematite (α-Fe_2O_3) studied by extended x-ray absorption fine structure and molecular dynamics *J. Chem. Phys.* **140** 224504

[86] Kennedy J H and Frese K W 1978 Photooxidation of Water at α-Fe[sub 2]O[sub 3] Electrodes *J. Electrochem. Soc.* **125** 709

[87] Beermann N, Vayssieres L, Lindquist S-E and Hagfeldt A 2000 Photoelectrochemical Studies of Oriented Nanorod Thin Films of Hematite *J. Electrochem. Soc.* **147** 2456

[88] Kleiman-Shwarsctein A, Hu Y-S, Forman A J, Stucky G D and McFarland E W 2008 Electrodeposition of α-Fe_2O_3 Doped with Mo or Cr as Photoanodes for Photocatalytic Water Splitting *J. Phys. Chem. C* **112** 15900–7

[89] Marusak L A, Messier R and White W B 1980 Optical absorption spectrum of hematite, αFe2O3 near IR to UV *J. Phys. Chem. Solids* **41** 981–4

[90] Debnath N C and Anderson A B 1982 Optical Spectra of Ferrous and Ferric Oxides and the Passive Film: A Molecular Orbital Study *J. Electrochem. Soc.* **129** 2169

[91] Galuza A I, Beznosov A B and Eremenko V V. 1998 Optical absorption edge in α–Fe2O3: The exciton–magnon structure *Low Temp. Phys.* **24** 726–9

[92] Wheeler D A, Wang G, Ling Y, Li Y and Zhang J Z 2012 Nanostructured hematite: synthesis, characterization, charge carrier dynamics, and photoelectrochemical properties *Energy Environ. Sci.* **5** 6682–702

[93] He Y P, Miao Y M, Li C R, Wang S Q, Cao L, Xie S S, Yang G Z, Zou B S and Burda C 2005 Size and structure effect on optical transitions of iron oxide nanocrystals *Phys. Rev. B* **71** 125411

[94] Nerine J. Cherepy †, Dorion B. Liston †, Jennifer A. Lovejoy †, Hongmei Deng ‡ and and Jin Z. Zhang* † 1998 Ultrafast Studies of Photoexcited Electron Dynamics in γ- and α-Fe2O3 Semiconductor Nanoparticles *J. Phys. Chem. B* **102** 770–6

[95] Chatterjee S, Sarkar S and Bhattacharyya S N 1993 Size effect in the photochemical generation of hydrogen from water by colloidal Fe2O3 particles *J. Photochem. Photobiol. A Chem.* **72** 183–7

[96] Fan H M, You G J, Li Y, Zheng Z, Tan H R, Shen Z X, Tang S H and Feng Y P 2009 Shape-Controlled Synthesis of Single-Crystalline Fe_2O_3 Hollow Nanocrystals and Their Tunable Optical Properties *J. Phys. Chem. C* **113** 9928–35

[97] Lu L, Li L, Wang X and Li G 2005 Understanding of the Finite Size Effects on Lattice Vibrations and Electronic Transitions of Nano alpha-Fe2O3 *J. Phys. Chem.*

B **109** 17151–6

[98] Tsuda N (Nobuo) 2000 *Electronic conduction in oxides* (Springer)

[99] Zou B, Huang W, Han M Y, Li S F Y, Xiaochun W, Zhang Y, Zhang J, Pengfei W and Wang R 1997 Anomalous optical properties and electron-phonon coupling enhancement in Fe2O3 nanoparticles coated with a layer of stearates *J. Phys. Chem. Solids* **58** 1315–20

[100] Tolbert S H and Alivisatos A P 1994 Size Dependence of a First Order Solid-Solid Phase Transition: The Wurtzite to Rock Salt Transformation in CdSe Nanocrystals *Science (80-.).* **265** 373–6

[101] Joly A G, Williams J R, Chambers S A, Xiong G, Hess W P and Laman D M 2006 Carrier dynamics in α-Fe2O3 (0001) thin films and single crystals probed by femtosecond transient absorption and reflectivity *J. Appl. Phys.* **99** 053521

[102] Fu L, Wu Z, Ai X, Zhang J, Nie Y, Xie S, Yang G and Zou B 2004 Time-resolved spectroscopic behavior of Fe2O3 and ZnFe2O4 nanocrystals *J. Chem. Phys.* **120** 3406–13

[103] Wang G, Ling Y, Wheeler D A, George K E N, Horsley K, Heske C, Zhang J Z and Li Y 2011 Facile Synthesis of Highly Photoactive α-Fe $_2$ O $_3$ -Based Films for Water Oxidation *Nano Lett.* **11** 3503–9

[104] Kronawitter C X, Vayssieres L, Shen S, Guo L, Wheeler D A, Zhang J Z, Antoun B R and Mao S S 2011 A perspective on solar-driven water splitting with all-oxide hetero-nanostructures *Energy Environ. Sci.* **4** 3889

[105] Kronawitter C X, Bakke J R, Wheeler D A, Wang W-C, Chang C, Antoun B R, Zhang J Z, Guo J, Bent S F, Mao S S and Vayssieres L 2011 Electron Enrichment

in 3d Transition Metal Oxide Hetero-Nanostructures *Nano Lett.* **11** 3855–61

[106] Morin F J 1951 Electrical Properties of α-Fe2O3 and α-Fe2O3 containing Titanium *Phys. Rev.* **83** 1005–10

[107] Morin F J 1954 Electrical Properties of α-Fe2O3 *Phys. Rev.* **93** 1195–9

[108] Bosman A J and van Daal H J 1970 Small-polaron versus band conduction in some transition-metal oxides *Adv. Phys.* **19** 1–117

[109] CHANG R H and WAGNER J B 1972 Direct-Current Conductivity and Iron Tracer Diffusion in Hematite at High Temperatures *J. Am. Ceram. Soc.* **55** 211–3

[110] Goodenough J B 1971 Metallic oxides *Prog. Solid State Chem.* **5** 145–399

[111] Launay J C and Horowitz G 1982 Crystal growth and photoelectrochemical study of Zr-doped α-Fe2O3 single crystal *J. Cryst. Growth* **57** 118–24

[112] Nakau T 1960 Electrical conductivity of α-Fe2O3 *J. Phys. Soc. Jpn.* **15** 727

[113] Benjelloun D, Bonnet J P, Doumerc J P, Launay J C, Onillon M and Hagenmuller P 1984 Anisotropy of electrical properties of iron oxide α-Fe2O3 *Mater. Chem. Phys.* **10** 503–18

[114] Hahn N T and Mullins C B 2010 Photoelectrochemical Performance of Nanostructured Ti- and Sn-Doped α-Fe $_2$ O $_3$ Photoanodes *Chem. Mater.* **22** 6474–82

[115] Julie A. Glasscock *, Piers R. F. Barnes, Ian C. Plumb A and Savvides N 2007 Enhancement of Photoelectrochemical Hydrogen Production from Hematite Thin Films by the Introduction of Ti and Si *J. Phys. Chem. C* **111** 16477–88

[116] Chantal Jorand Sartoretti, Bruce D. Alexander, Renata Solarska, Iwona A. Rutkowska A, Augustynski* J and Cerny R 2005 Photoelectrochemical Oxidation

of Water at Transparent Ferric Oxide Film Electrodes *J. Phys. Chem. B* **109** 13685–92

[117] Iordanova N, Dupuis M and Rosso K M 2005 Charge transport in metal oxides: A theoretical study of hematite α-Fe2O3 *J. Chem. Phys.* **122** 144305

[118] Velev J, Bandyopadhyay A, Butler W H and Sarker S 2005 Electronic and magnetic structure of transition-metal-doped α -hematite *Phys. Rev. B* **71** 205208

[119] Xu Y Y, Rui X F, Fu Y Y and Zhang H 2005 Magnetic properties of α-Fe2O3 nanowires *Chem. Phys. Lett.* **410** 36–8

[120] Zhao Y, Dunnill C W, Zhu Y, Gregory D H, Kockenberger W, Li Y, Hu W, Iftikhar Ahmad A and McCartney D G 2007 Low-Temperature Magnetic Properties of Hematite Nanorods *Chem. Mater.* **19** 916–21

[121] Zboril* R, Mashlan M and Petridis D 2002 Iron(III) Oxides from Thermal ProcessesSynthesis, Structural and Magnetic Properties, Mössbauer Spectroscopy Characterization, and Applications† *Chem. Mater.* **14** 969–82

[122] Xue D S, Gao C X, Liu Q F and Zhang L Y 2003 Preparation and characterization of haematite nanowire arrays *J. Phys. Condens. Matter* **15** 1455–9

[123] Fiorani D, Testa A M, Saber L, Angiolini M, Montone A and Polichetti M 1999 Size and shape effect on the canted antiferromagnetism in α-Fe2O3 particles *Nanostructured Mater.* **12** 939–42

[124] Sorescu M, Brand R A, Mihaila-Tarabasanu D and Diamandescu L 1999 The crucial role of particle morphology in the magnetic properties of haematite *J. Appl. Phys.* **85** 5546–8

[125] Jiao F, Harrison A, Jumas J-C, Chadwick A V., Winfried Kockelmann A and Peter

G. Bruce 2006 Ordered Mesoporous Fe2O3 with Crystalline Walls *J. Am. Chem. Soc.* **128** 5468–74

[126] Liu L, Kou H-Z, Mo W, Huajie Liu A and Wang Y 2006 Surfactant-Assisted Synthesis of α-Fe2O3 Nanotubes and Nanorods with Shape-Dependent Magnetic Properties *J. Phys. Chem. B* **110** 15218–23

[127] Gao Y, Bao Y, Beerman M, Yasuhara A, Shindo D and Krishnan K M 2004 Superstructures of self-assembled cobalt nanocrystals *Appl. Phys. Lett.* **84** 3361–3

[128] Berkowitz A E, Lahut J A, Jacobs I S, Levinson L M and Forester D W 1975 Spin Pinning at Ferrite-Organic Interfaces *Phys. Rev. Lett.* **34** 594–7

[129] Kodama R H, Berkowitz A E, McNiff, Jr. E J and Foner S 1996 Surface Spin Disorder in NiFe2O4 nanoparticles *Phys. Rev. Lett.* **77** 394–7

[130] Morrish A H 1995 *Canted Antiferromagnetism: Hematite* (WORLD SCIENTIFIC)

[131] Kumar A, Fähler S, Schlörb H, Leistner K and Schultz L 2006 Competition between shape anisotropy and magnetoelastic anisotropy in Ni nanowires electrodeposited within alumina templates *Phys. Rev. B* **73** 064421

[132] Sorop T G, Nielsch K, Göring P, Kröll M, Blau W, Wehrspohn R B, Gösele U and de Jongh L J 2004 Study of the magnetic hysteresis in arrays of ferromagnetic Fe nanowires as a function of the template filling fraction *J. Magn. Magn. Mater.* **272**–**276** 1656–7

[133] Dunlop D J 1990 *Developments in rock magnetism* vol 53

[134] Kletetschka G and Wasilewski P J 2002 Grain size limit for SD hematite *Phys. Earth Planet. Inter.* **129** 173–9

[135] Taskeya Haider 2017 A Review of Magneto-Optic Effects and Its Application *Int.*

J. Electromagn. Appl. **7** 17–24

[136] Boardman A and King N 2009 Magneto-optics and the Kerr Effect with Ferromagnetic Materials *Tutorials in Complex Photonic Media* (1000 20th Street, Bellingham, WA 98227-0010 USA: SPIE) pp 57–79

[137] Faraday M 1846 I. Experimental researches in electricity.-Nineteenth series *Philos. Trans. Roy. Soc.* **1** 136

[138] Landau L D and Lifshitz E M 1984 *Electrodynamics of continuous media* (Oxford: Pergamon Press)

[139] Kerr J 1877 XLIII. *On rotation of the plane of polarization by reflection from the pole of a magnet London, Edinburgh, Dublin Philos. Mag. J. Sci.* **3** 321–43

[140] Sugano S and Kojima N 2000 *Magneto-Optics* vol 128 (Berlin, Heidelberg: Springer Berlin Heidelberg)

[141] Qiu Z Q and Bader S D 2000 Surface magneto-optic Kerr effect *Rev. Sci. Instrum.* **71** 1243–55

[142] Armelles G, Cebollada A, García-Martín A and González M U 2013 Magnetoplasmonics: Combining Magnetic and Plasmonic Functionalities *Adv. Opt. Mater.* **1** 10–35

[143] Armelles G, González-Díaz J B, García-Martín A, García-Martín J M, Cebollada A, González M U, Acimovic S, Cesario J, Quidant R and Badenes G 2008 Localized surface plasmon resonance effects on the magneto-optical activity of continuous Au/Co/Au trilayers *Opt. Express* **16** 16104

[144] Williams H J, Sherwood R C and Remeika J P 1958 Magnetic Domains in α−Fe $_2$ O $_3$ *J. Appl. Phys.* **29** 1772–3

[145] Kalfagiannis N, Karagiannidis P G, Pitsalidis C, Panagiotopoulos N T, Gravalidis C, Kassavetis S, Patsalas P and Logothetidis S 2012 Plasmonic silver nanoparticles for improved organic solar cells *Sol. Energy Mater. Sol. Cells* **104** 165–74

[146] Warren S C and Thimsen E 2012 Plasmonic solar water splitting *Energy Environ. Sci.* **5** 5133–46

[147] Thomann I, Pinaud B A, Chen Z, Clemens B M, Jaramillo T F and Brongersma M L 2011 Plasmon Enhanced Solar-to-Fuel Energy Conversion *Nano Lett.* **11** 3440–6

[148] Mayergoyz I D 2012 *Plasmon resonances in nanoparticles* (World Scientific Publishing Company)

[149] Willets K A and Van Duyne R P 2007 Localized Surface Plasmon Resonance Spectroscopy and Sensing *Annu. Rev. Phys. Chem.* **58** 267–97

[150] Schasfoort R B M and Tudos A J 2008 *Handbook of Surface Plasmon Resonance* ed R B M Schasfoort and A J Tudos (Cambridge: Royal Society of Chemistry)

[151] Amendola V, Pilot R, Frasconi M, Marago O M and Iati M A 2017 Surface plasmon resonance in gold nanoparticles: a review *J. Phys. Condens. Matter* **29** 203002

[152] Blaber M G, Arnold M D and Ford M J 2010 A review of the optical properties of alloys and intermetallics for plasmonics *J. Phys. Condens. Matter* **22** 143201

[153] Arnold M D and Blaber M G 2009 Optical performance and metallic absorption in nanoplasmonic systems *Opt. Express* **17** 3835

[154] Brongersma M L, Halas N J and Nordlander P 2015 Plasmon-induced hot carrier science and technology *Nat. Nanotechnol.* **10** 25–34

[155] Ye W, Long R, Huang H and Xiong Y 2017 Plasmonic nanostructures in solar energy conversion *J. Mater. Chem. C* **5** 1008–21

[156] Dreaden E C, Alkilany A M, Huang X, Murphy C J and El-Sayed M A 2012 The golden age: gold nanoparticles for biomedicine *Chem. Soc. Rev.* **41** 2740–79

[157] Amendola V and Meneghetti M 2009 Laser ablation synthesis in solution and size manipulation of noble metal nanoparticles *Phys. Chem. Chem. Phys.* **11** 3805

[158] Daniel M-C and Astruc D 2004 Gold nanoparticles: assembly, supramolecular chemistry, quantum-size-related properties, and applications toward biology, catalysis, and nanotechnology. *Chem. Rev.* **104** 293–346

[159] Maier S A 2007 *Plasmonics: Fundamentals and Applications* (New York, NY: Springer US)

[160] Kreibig U and Vollmer M 1995 *Optical properties of metal clusters* (Springer)

[161] Prashant K. Jain †, Kyeong Seok Lee †, Ivan H. El-Sayed *,‡ and and Mostafa A. El-Sayed* † 2006 Calculated Absorption and Scattering Properties of Gold Nanoparticles of Different Size, Shape, and Composition: Applications in Biological Imaging and Biomedicine

[162] Poletti A, Fracasso G, Conti G, Pilot R and Amendola V 2015 Laser generated gold nanocorals with broadband plasmon absorption for photothermal applications. *Nanoscale* **7** 13702–14

[163] Govorov A O and Richardson H H 2007 Generating heat with metal nanoparticles *Nano Today* **2** 30–8

[164] Govorov A O, Zhang W, Skeini T, Richardson H, Lee J and Kotov N A 2006 Gold nanoparticle ensembles as heaters and actuators: melting and collective plasmon resonances *Nanoscale Res. Lett.* **1** 84–90

[165] Amendola V, Saija R, Maragò O M and Iatì M A 2015 Superior plasmon absorption

in iron-doped gold nanoparticles *Nanoscale* **7** 8782–92

[166] Scholl J A, Koh A L and Dionne J A 2012 Quantum plasmon resonances of individual metallic nanoparticles *Nature* **483** 421–7

[167] Malola S, Lehtovaara L, Enkovaara J and Häkkinen H 2013 Birth of the Localized Surface Plasmon Resonance in Monolayer-Protected Gold Nanoclusters *ACS Nano* **7** 10263–70

[168] Park J, Kang H, Kim Y H, Lee S-W, Lee T G and Wi J-S 2016 Physically-synthesized gold nanoparticles containing multiple nanopores for enhanced photothermal conversion and photoacoustic imaging *Nanoscale* **8** 15514–20

[169] Wi J-S, Tominaka S, Uosaki K and Nagao T 2012 Porous gold nanodisks with multiple internal hot spots *Phys. Chem. Chem. Phys.* **14** 9131

[170] Reichenbach P, Horneber A, Gollmer D A, Hille A, Mihaljevic J, Schäfer C, Kern D P, Meixner A J, Zhang D, Fleischer M and Eng L M 2014 Nonlinear optical point light sources through field enhancement at metallic nanocones *Opt. Express* **22** 15484

[171] Barbosa S, Agrawal A, Rodríguez-Lorenzo L, Pastoriza-Santos I, Alvarez-Puebla R A, Kornowski A, Weller H and Liz-Marzán L M 2010 Tuning Size and Sensing Properties in Colloidal Gold Nanostars *Langmuir* **26** 14943–50

[172] Soares L, Csáki A, Jatschka J, Fritzsche W, Flores O, Franco R and Pereira E 2014 Localized surface plasmon resonance (LSPR) biosensing using gold nanotriangles: detection of DNA hybridization events at room temperature *Analyst* **139** 4964–73

[173] Wu H-L, Kuo C-H and Huang M H 2010 Seed-Mediated Synthesis of Gold Nanocrystals with Systematic Shape Evolution from Cubic to Trisoctahedral and

Rhombic Dodecahedral Structures *Langmuir* **26** 12307–13

[174] Luan J, Liu K-K, Tadepalli S, Jiang Q, Morrissey J J, Kharasch E D and Singamaneni S 2016 PEGylated Artificial Antibodies: Plasmonic Biosensors with Improved Selectivity *ACS Appl. Mater. Interfaces* **8** 23509–16

[175] Haes A J, Haynes C L, McFarland A D, Schatz G C, Van Duyne R P and Zou S 2005 Plasmonic Materials for Surface-Enhanced Sensing and Spectrosopy Size-and Shape-Tunable Localized Surface Plasmon Resonance Spectra *MRS Bull.* **30** 368–75

[176] Xia Y and Halas N J 2005 Shape-Controlled Synthesis and Surface Plasmonic Properties of Metallic Nanostructures *MRS Bull.* **30** 338–48

[177] Harris N, Ford M J, Mulvaney P and Cortie M B 2008 Tunable infrared absorption by metal nanoparticles: The case for gold rods and shells *Gold Bull.* **41** 5–14

[178] Prescott S W and Mulvaney P 2006 Gold nanorod extinction spectra *J. Appl. Phys.* **99** 123504

[179] Jain P K, El-Sayed I H and El-Sayed M A 2007 Au nanoparticles target cancer *Nano Today* **2** 18–29

[180] Amendola V, Scaramuzza S, Agnoli S, Polizzi S and Meneghetti M 2014 Strong dependence of surface plasmon resonance and surface enhanced Raman scattering on the composition of Au–Fe nanoalloys *Nanoscale* **6** 1423–33

[181] Amendola V, Meneghetti M, Bakr O M, Riello P, Polizzi S, Anjum D H, Fiameni S, Arosio P, Orlando T, de Julian Fernandez C, Pineider F, Sangregorio C and Lascialfari A 2013 Coexistence of plasmonic and magnetic properties in Au89Fe11 nanoalloys *Nanoscale* **5** 5611

[182] Amendola V, Scaramuzza S, Agnoli S, Granozzi G, Meneghetti M, Campo G, Bonanni V, Pineider F, Sangregorio C, Ghigna P, Polizzi S, Riello P, Fiameni S and Nodari L 2015 Laser generation of iron-doped silver nanotruffles with magnetic and plasmonic properties *Nano Res.* **8** 4007–23

[183] Rioux D and Meunier M 2015 Seeded Growth Synthesis of Composition and Size-Controlled Gold–Silver Alloy Nanoparticles *J. Phys. Chem. C* **119** 13160–8

[184] Verbruggen S W, Keulemans M, Martens J A and Lenaerts S 2013 Predicting the Surface Plasmon Resonance Wavelength of Gold–Silver Alloy Nanoparticles *J. Phys. Chem. C* **117** 19142–5

[185] S. Link †, Z. L. Wang ‡ and and M. A. El-Sayed* † 1999 Alloy Formation of Gold−Silver Nanoparticles and the Dependence of the Plasmon Absorption on Their Composition *J. Phys. Chem. B* **103** 3529–33

[186] Amendola V, Bakr O M and Stellacci F 2010 A Study of the Surface Plasmon Resonance of Silver Nanoparticles by the Discrete Dipole Approximation Method: Effect of Shape, Size, Structure, and Assembly *Plasmonics* **5** 85–97

[187] Cortie M B and McDonagh A M 2011 Synthesis and Optical Properties of Hybrid and Alloy Plasmonic Nanoparticles *Chem. Rev.* **111** 3713–35

[188] Sarina S, Zhu H, Jaatinen E, Xiao Q, Liu H, Jia J, Chen C and Zhao J 2013 Enhancing Catalytic Performance of Palladium in Gold and Palladium Alloy Nanoparticles for Organic Synthesis Reactions through Visible Light Irradiation at Ambient Temperatures *J. Am. Chem. Soc.* **135** 5793–801

[189] Suntivich J, Xu Z, Carlton C E, Kim J, Han B, Lee S W, Bonnet N, Marzari N, Allard L F, Gasteiger H A, Hamad-Schifferli K and Shao-Horn Y 2013 Surface

Composition Tuning of Au–Pt Bimetallic Nanoparticles for Enhanced Carbon Monoxide and Methanol Electro-oxidation *J. Am. Chem. Soc.* **135** 7985–91

[190] Wang F, Li C, Chen H, Jiang R, Sun L-D, Li Q, Wang J, Yu J C and Yan C-H 2013 Plasmonic Harvesting of Light Energy for Suzuki Coupling Reactions *J. Am. Chem. Soc.* **135** 5588–601

[191] Cable R E and Schaak R E 2007 Solution Synthesis of Nanocrystalline M−Zn (M = Pd, Au, Cu) Intermetallic Compounds via Chemical Conversion of Metal Nanoparticle Precursors *Chem. Mater.* **19** 4098–104

[192] Keast V J, Wallace J W, Wrightson C J, Tai M, Gentle A, Arnold M D and Cortie M B 2015 The effect of vacancies on the optical properties of $AuAl_2$ *J. Phys. Condens. Matter* **27** 505501

[193] Lee Y P, Kudryavtsev Y V., Nemoshkalenko V V., Gontarz R and Rhee J Y 2003 Magneto-optical and optical properties of Fe-rich Au-Fe alloy films near the fcc-bcc structural transformation region *Phys. Rev. B* **67** 104424

[194] Jain P K, Huang X, El-Sayed I H and El-Sayed M A 2008 Noble Metals on the Nanoscale: Optical and Photothermal Properties and Some Applications in Imaging, Sensing, Biology, and Medicine *Acc. Chem. Res.* **41** 1578–86

[195] Abadeer N S and Murphy C J 2016 Recent Progress in Cancer Thermal Therapy Using Gold Nanoparticles *J. Phys. Chem. C* **120** 4691–716

[196] Gomes Silva C, Juárez R, Marino T, Molinari R and García H 2011 Influence of Excitation Wavelength (UV or Visible Light) on the Photocatalytic Activity of Titania Containing Gold Nanoparticles for the Generation of Hydrogen or Oxygen from Water *J. Am. Chem. Soc.* **133** 595–602

[197] Knight M W, King N S, Liu L, Everitt H O, Nordlander P and Halas N J 2014 Aluminum for Plasmonics *ACS Nano* **8** 834–40

[198] Huang X and El-Sayed M A 2010 Gold nanoparticles: Optical properties and implementations in cancer diagnosis and photothermal therapy *J. Adv. Res.* **1** 13–28

[199] Villesen T F, Uhrenfeldt C, Johansen B and Nylandsted Larsen A 2013 Self-assembled Al nanoparticles on Si and fused silica, and their application for Si solar cells *Nanotechnology* **24** 275606

[200] Ono A, Kikawada M, Akimoto R, Inami W and Kawata Y 2013 Fluorescence enhancement with deep-ultraviolet surface plasmon excitation *Opt. Express* **21** 17447

[201] Clark B D, Jacobson C R, Lou M, Yang J, Zhou L, Gottheim S, DeSantis C J, Nordlander P and Halas N J 2018 Aluminum Nanorods *Nano Lett.* **18** 1234–40

[202] Su M-N, Ciccarino C J, Kumar S, Dongare P D, Hosseini Jebeli S A, Renard D, Zhang Y, Ostovar B, Chang W-S, Nordlander P, Halas N J, Sundararaman R, Narang P and Link S 2019 Ultrafast Electron Dynamics in Single Aluminum Nanostructures *Nano Lett.* **19** 3091–7

[203] Sarychev A K, Shvets G and Shalaev V M 2006 Magnetic plasmon resonance *Phys. Rev. E* **73** 036609

[204] Shafiei F, Monticone F, Le K Q, Liu X-X, Hartsfield T, Alù A and Li X 2013 A subwavelength plasmonic metamolecule exhibiting magnetic-based optical Fano resonance *Nat. Nanotechnol.* **8** 95–9

[205] Mühlig S, Cunningham A, Scheeler S, Pacholski C, Bürgi T, Rockstuhl C and Lederer F 2011 Self-Assembled Plasmonic Core–Shell Clusters with an Isotropic

Magnetic Dipole Response in the Visible Range *ACS Nano* **5** 6586–92

[206] Campione S, Guclu C, Ragan R and Capolino F 2014 Enhanced Magnetic and Electric Fields via Fano Resonances in Metasurfaces of Circular Clusters of Plasmonic Nanoparticles *ACS Photonics* **1** 254–60

[207] Pineider F, Campo G, Bonanni V, de Julián Fernández C, Mattei G, Caneschi A, Gatteschi D and Sangregorio C 2013 Circular Magnetoplasmonic Modes in Gold Nanoparticles *Nano Lett.* **13** 4785–9

[208] Chiu K W and Quinn J J 1972 Magnetoplasma Surface Waves in Polar Semiconductors: Retardation Effects *Phys. Rev. Lett.* **29** 600–3

[209] Chiu K W and Quinn J J 1972 Magnetoplasma Surface Waves in Metals *Phys. Rev. B* **5** 4707–9

[210] Brion J J, Wallis R F, Hartstein A and Burstein E 1972 Theory of Surface Magnetoplasmons in Semiconductors *Phys. Rev. Lett.* **28** 1455–8

[211] Lyubchanskii I L, Dadoenkova N N, Lyubchanskii M I, Shapovalov E A and Rasing T 2003 Magnetic photonic crystals *J. Phys. D. Appl. Phys.* **36** R277–87

[212] Inoue M, Fujikawa R, Baryshev A, Khanikaev A, Lim P B, Uchida H, Aktsipetrov O, Fedyanin A, Murzina T and Granovsky A 2006 Magnetophotonic crystals *J. Phys. D. Appl. Phys.* **39** R151–61

[213] Levy M, Jalali A A and Huang X 2009 Magnetophotonic crystals: nonreciprocity, birefringence and confinement *J. Mater. Sci. Mater. Electron.* **20** 43–7

[214] Sepúlveda B, Calle A, Lechuga L M and Armelles G 2006 Highly sensitive detection of biomolecules with the magneto-optic surface-plasmon-resonance sensor *Opt. Lett.* **31** 1085

[215] Temnov V V., Armelles G, Woggon U, Guzatov D, Cebollada A, Garcia-Martin A, Garcia-Martin J-M, Thomay T, Leitenstorfer A and Bratschitsch R 2010 Active magneto-plasmonics in hybrid metal–ferromagnet structures *Nat. Photonics* **4** 107–11

[216] Xia T K, Hui P M and Stroud D 1990 Theory of Faraday rotation in granular magnetic materials *J. Appl. Phys.* **67** 2736–41

[217] Yu Z, Veronis G, Wang Z and Fan S 2008 One-Way Electromagnetic Waveguide Formed at the Interface between a Plasmonic Metal under a Static Magnetic Field and a Photonic Crystal *Phys. Rev. Lett.* **100** 023902

[218] Majorana Q 1944 Il fenomeno Kerr nei metalli non ferromagnetici *Nuovo Cim.* **2** 1–13

[219] Stern E A, McGroddy J C and Harte W E 1964 Polar Reflection Faraday Effect in Metals *Phys. Rev.* **135** A1306–14

[220] Schnatterly S E 1969 Magnetoreflection Measurements on the Noble Metals *Phys. Rev.* **183** 664–7

[221] Haefner P, Luck E and Mohler E 1994 Magnetooptical Properties of Surface Plasma Waves on Copper, Silver, Gold, and Aluminum *Phys. status solidi* **185** 289–99

[222] Ebert H, Ködderitzsch D and Minár J 1996 Magneto-optical effects in transition metal systems *Reports Prog. Phys.* **59** 1665–735

[223] Johnson P and Christy R 1974 Optical constants of transition metals: Ti, V, Cr, Mn, Fe, Co, Ni, and Pd *Phys. Rev. B* **9** 5056–70

[224] Johnson P B and Christy R W 1972 Optical Constants of the Noble Metals *Phys. Rev. B* **6** 4370–9

[225] Armelles G, Cebollada A, García-Martín A, García-Martín J M, González M U, González-Díaz J B, Ferreiro-Vila E and Torrado J F 2009 Magnetoplasmonic nanostructures: systems supporting both plasmonic and magnetic properties *J. Opt. A Pure Appl. Opt.* **11** 114023

[226] Hermann C, Kosobukin V, Lampel G, Peretti J, Safarov V and Bertrand P 2001 Surface-enhanced magneto-optics in metallic multilayer films *Phys. Rev. B* **64** 235422

[227] Bertrand P, Hermann C, Lampel G, Peretti J and Safarov V 2001 General analytical treatment of optics in layered structures: Application to magneto-optics *Phys. Rev. B* **64** 235421

[228] Bonod N, Reinisch R, Popov E and Nevière M 2004 Optimization of surface-plasmon-enhanced magneto-optical effects *J. Opt. Soc. Am. B* **21** 791

[229] Clavero C, Yang K, Skuza J R and Lukaszew R A 2010 Magnetic field modulation of intense surface plasmon polaritons *Opt. Express* **18** 7743

[230] Meneses-Rodríguez D, Ferreiro-Vila E, Prieto P, Anguita J, González M U, García-Martín J M, Cebollada A, García-Martín A and Armelles G 2011 Probing the Electromagnetic Field Distribution within a Metallic Nanodisk *Small* **7** 3317–23

[231] Kravets V ., Petford-Long A . and Kravetz A . 1999 Study of optical and magneto-optical properties of CoFe–HfO2 granular magnetic films *Phys. E Low-dimensional Syst. Nanostructures* **4** 292–9

[232] Kravets V G, Petford-Long A K and Kravets A F 2000 Optical and magneto-optical properties of (CoFe)x(HfO21)1−x magnetic granular films *J. Appl. Phys.* **87** 1762–8

[233] Kravets V G and Poperenko L V. 2008 Magnetooptical properties of Co-SiO2 granular films *Opt. Spectrosc.* **104** 610–4

[234] Melle S, Menéndez J L, Armelles G, Navas D, Vázquez M, Nielsch K, Wehrspohn R B and Gösele U 2003 Magneto-optical properties of nickel nanowire arrays *Appl. Phys. Lett.* **83** 4547–9

[235] González-Díaz J B, García-Martín A, Armelles G, Navas D, Vázquez M, Nielsch K, Wehrspohn R B and Gösele U 2007 Enhanced Magneto-Optics and Size Effects in Ferromagnetic Nanowire Arrays *Adv. Mater.* **19** 2643–7

[236] González-Díaz J B, García-Martín A and Reig G A 2011 Unusual magneto-optical behavior induced by local dielectric variations under localized surface plasmon excitations *Nanoscale Res. Lett.* **6** 408

[237] González-Díaz J B, García-Martín A, García-Martín J M, Cebollada A, Armelles G, Sepúlveda B, Alaverdyan Y and Käll M 2008 Plasmonic Au/Co/Au Nanosandwiches with Enhanced Magneto-optical Activity *Small* **4** 202–5

[238] Jain P K, Xiao Y, Walsworth R and Cohen A E 2009 Surface Plasmon Resonance Enhanced Magneto-Optics (SuPREMO): Faraday Rotation Enhancement in Gold-Coated Iron Oxide Nanocrystals *Nano Lett.* **9** 1644–50

[239] Loughran T H J, Keatley P S, Hendry E, Barnes W L and Hicken R J 2018 Enhancing the magneto-optical Kerr effect through the use of a plasmonic antenna *Opt. Express* **26** 4738

[240] Qin J, Zhang Y, Liang X, Liu C, Wang C, Kang T, Lu H, Zhang L, Zhou P, Wang X, Peng B, Hu J, Deng L and Bi L 2017 Ultrahigh Figure-of-Merit in Metal–Insulator–Metal Magnetoplasmonic Sensors Using Low Loss Magneto-optical

Oxide Thin Films *ACS Photonics* **4** 1403–12

[241] Tomita S, Kato T, Tsunashima S, Iwata S, Fujii M and Hayashi S 2006 Magneto-Optical Kerr Effects of Yttrium-Iron Garnet Thin Films Incorporating Gold Nanoparticles *Phys. Rev. Lett.* **96** 167402

[242] Fujikawa R, Baryshev A V., Kim J, Uchida H and Inoue M 2008 Contribution of the surface plasmon resonance to optical and magneto-optical properties of a Bi:YIG-Au nanostructure *J. Appl. Phys.* **103** 07D301

[243] Uchida H, Masuda Y, Fujikawa R, Baryshev A V and Inoue M 2009 Large enhancement of Faraday rotation by localized surface plasmon resonance in Au nanoparticles embedded in Bi:YIG film *J. Magn. Magn. Mater.* **321** 843–5

[244] Uchida H, Mizutani Y, Nakai Y, Fedyanin A A and Inoue M 2011 Garnet composite films with Au particles fabricated by repetitive formation for enhancement of Faraday effect *J. Phys. D. Appl. Phys.* **44** 064014

[245] Hamidi S M, Tehranchi M M and Sadeghi S 2011 Effect of magnetic annealing on magneto-optical properties of Ce : YIG thin films incorporating gold nanoparticles *J. Phys. D. Appl. Phys.* **44** 305003

[246] Mayergoyz I D, Lang G, Hung L, Tkachuk S, Krafft C and Rabin O 2010 Plasmon resonance enhancement of magneto-optic effects in garnets *J. Appl. Phys.* **107** 09A925

[247] Tkachuk S, Lang G, Krafft C, Rabin O and Mayergoyz I 2011 Plasmon resonance enhancement of Faraday rotation in thin garnet films *J. Appl. Phys* **109** 07B717

[248] Huang D-W, Ma Y-F, Sung M-J and Huang C-P 2010 Approach the angular sensitivity limit in surface plasmon resonance sensors with low index prism and

large resonant angle *Opt. Eng.* **49** 054403

[249] Zeng B, Gao Y and Bartoli F J 2014 Rapid and highly sensitive detection using Fano resonances in ultrathin plasmonic nanogratings *Appl. Phys. Lett.* **105** 161106

[250] Liu Y and Kim J 2010 Numerical investigation of finite thickness metal-insulator-metal structure for waveguide-based surface plasmon resonance biosensing *Sensors Actuators B Chem.* **148** 23–8

[251] Lee K-S, Son J M, Jeong D-Y, Lee T S and Kim W M 2010 Resolution Enhancement in Surface Plasmon Resonance Sensor Based on Waveguide Coupled Mode by Combining a Bimetallic Approach *Sensors* **10** 11390–9

[252] Ignatyeva D O, Knyazev G A, Kapralov P O, Dietler G, Sekatskii S K and Belotelov V I 2016 Magneto-optical plasmonic heterostructure with ultranarrow resonance for sensing applications *Sci. Rep.* **6** 28077

[253] Kataja M, Pourjamal S, Maccaferri N, Vavassori P, Hakala T K, Huttunen M J, Törmä P and Van Dijken S 2016 Hybrid plasmonic lattices with tunable magnetooptical activity *Opt. Express* **24** 3652–62

[254] Liu Y, Flores J F and Lu J Q 2014 Tailoring 1D ZnO Nanostructure Using Engineered Catalyst Enabled by Poly(4-vinylpyridine) *J. Phys. Chem. C* **118** 19387–95

[255] Pauporté T, Jouanno E, Pellé F, Viana B and Aschehoug P 2009 Key Growth Parameters for the Electrodeposition of ZnO Films with an Intense UV-Light Emission at Room Temperature *J. Phys. Chem. C* **113** 10422–31

[256] Ishihara H, Sarang S, Chen Y-C, Lin O, Phummirat P, Thung L, Hernandez J, Ghosh S and Tung V 2016 Nature inspiring processing route toward high throughput

production of perovskite photovoltaics *J. Mater. Chem. A* **4** 6989

[257] Ishihara H, Chen W, Chen Y-C, Sarang S, De Marco N, Lin O, Ghosh S and Tung V 2016 Electrohydrodynamically Assisted Deposition of Efficient Perovskite Photovoltaics *Adv. Mater. Interfaces* **3** 1500762

[258] Nikolaidou K, Sarang S, Hoffman C, Mendewala B, Ishihara H, Lu J Q, Ilan B, Tung V and Ghosh S 2016 Hybrid Perovskite Thin Films as Highly Efficient Luminescent Solar Concentrators *Adv. Opt. Mater.* **4** 2126–32

[259] Perkowitz S 1993 *Optical characterization of semiconductors : infrared, Raman, and photoluminescence spectroscopy* (Academic Press)

[260] Wahl M 2014 *Time-Correlated Single Photon Counting* (Berlin)

[261] Owen T 2000 *Fundamentals of modern UV-visible spectroscopy*

[262] Paddock S W, Fellers T J and Davidson M W Introductory Confocal Concepts | MicroscopyU

[263] Prasad V, Semwogerere D and Weeks E R 2007 Confocal microscopy of colloids *J. Phys. Condens. Matter* **19** 113102

[264] ZEISS ZEISS GeminiSEM - Field Emission Scanning Electron Microscope

[265] PhotoMetrics I Scanning Electron Microscopy (SEM) – PhotoMetrics

[266] AZO materials 2017 Different Types of SEM Imaging – BSE and Secondary Electron Imaging

[267] PhotoMetrics Inc. Field Emission Scanning Electron Microscopy (FESEM) – PhotoMetrics

[268] Cerne J *Magneto-Polarimetry Advanced Lab* (Buffalo)

[269] Debije M G and Rajkumar V A 2015 Direct versus indirect illumination of a

prototype luminescent solar concentrator *Sol. Energy* **122** 334–40

[270] Gutierrez G D, Coropceanu I, Bawendi M G and Swager T M 2016 A Low Reabsorbing Luminescent Solar Concentrator Employing π-Conjugated Polymers *Adv. Mater.* **28** 497–501

[271] Slooff L H, Bende E E, Burgers A R, Budel T, Pravettoni M, Kenny R P, Dunlop E D and Büchtemann A 2008 A luminescent solar concentrator with 7.1% power conversion efficiency *Phys. status solidi - Rapid Res. Lett.* **2** 257–9

[272] Currie M J, Mapel J K, Heidel T D, Goffri S and Baldo M A 2008 High-efficiency organic solar concentrators for photovoltaics. *Science* **321** 226–8

[273] Sark W G J H M van, Barnham K W J, Slooff L H, Chatten A J, Büchtemann A, Meyer A, McCormack S J, Koole R, Farrell D J, Bose R, Bende E E, Burgers A R, Budel T, Quilitz J, Kennedy M, Meyer T, Donegá C D M, Meijerink A and Vanmaekelbergh D 2008 Luminescent Solar Concentrators - A review of recent results *Opt. Express* **16** 21773

[274] Slooff L H, Bakker N J, Sommeling P M, Büchtemann A, Wedel A and van Sark W G J H M 2014 Long-term optical stability of fluorescent solar concentrator plates *Phys. status solidi* **211** 1150–4

[275] Griffini G, Brambilla L, Levi M, Del Zoppo M and Turri S 2013 Photo-degradation of a perylene-based organic luminescent solar concentrator: Molecular aspects and device implications *Sol. Energy Mater. Sol. Cells* **111** 41–8

[276] Seybold G and Wagenblast G 1989 New perylene and violanthrone dyestuffs for fluorescent collectors *Dye. Pigment.* **11** 303–17

[277] Debije M G, Verbunt P P C, Nadkarni P J, Velate S, Bhaumik K, Nedumbamana S,

Rowan B C, Richards B S and Hoeks T L 2011 Promising fluorescent dye for solar energy conversion based on a perylene perinone *Appl. Opt.* **50** 163

[278] Coropceanu I and Bawendi M G 2014 Core/Shell Quantum Dot Based Luminescent Solar Concentrators with Reduced Reabsorption and Enhanced Efficiency *Nano Lett.* **14** 4097–101

[279] Meinardi F, Colombo A, Velizhanin K A, Simonutti R, Lorenzon M, Beverina L, Viswanatha R, Klimov V I and Brovelli S 2014 Large-area luminescent solar concentrators based on 'Stokes-shift-engineered' nanocrystals in a mass-polymerized PMMA matrix *Nat. Photonics* **8** 392–9

[280] Bradshaw L R, Knowles K E, McDowall S and Gamelin D R 2015 Nanocrystals for luminescent solar concentrators *Nano Lett.* **15** 1315–23

[281] Meinardi F, McDaniel H, Carulli F, Colombo A, Velizhanin K A, Makarov N S, Simonutti R, Klimov V I and Brovelli S 2015 Highly efficient large-area colourless luminescent solar concentrators using heavy-metal-free colloidal quantum dots *Nat. Nanotechnol.* **10** 878–85

[282] Li C, Chen W, Wu D, Quan D, Zhou Z, Hao J, Qin J, Li Y, He Z and Wang K 2016 Large Stokes Shift and High Efficiency Luminescent Solar Concentrator Incorporated with CuInS2/ZnS Quantum Dots *Sci. Rep.* **5** 17777

[283] Inman R H, Shcherbatyuk G V., Medvedko D, Gopinathan A and Ghosh S 2011 Cylindrical luminescent solar concentrators with near-infrared quantum dots *Opt. Express* **19** 24308

[284] S. R. Cordero, P. J. Carson, R. A. Estabrook, G. F. Strouse A and Buratto* S K 2000 Photo-Activated Luminescence of CdSe Quantum Dot Monolayers *J. Phys.*

Chem. B **104** 12137–42

[285] Zhou Y, Benetti D, Fan Z, Zhao H, Ma D, Govorov A O, Vomiero A and Rosei F 2016 Near Infrared, Highly Efficient Luminescent Solar Concentrators *Adv. Energy Mater.* **6** 1501913

[286] Nie W, Tsai H, Asadpour R, Blancon J-C, Neukirch A J, Gupta G, Crochet J J, Chhowalla M, Tretiak S, Alam M A, Wang H-L and Mohite A D 2015 Solar cells. High-efficiency solution-processed perovskite solar cells with millimeter-scale grains. *Science* **347** 522–5

[287] Löper P, Stuckelberger M, Niesen B, Werner J, Filipič M, Moon S-J, Yum J-H, Topič M, De Wolf S and Ballif C 2015 Complex Refractive Index Spectra of $CH_3NH_3PbI_3$ Perovskite Thin Films Determined by Spectroscopic Ellipsometry and Spectrophotometry *J. Phys. Chem. Lett.* **6** 66–71

[288] Chen C-W, Hsiao S-Y, Chen C-Y, Kang H-W, Huang Z-Y and Lin H-W 2015 Optical properties of organometal halide perovskite thin films and general device structure design rules for perovskite single and tandem solar cells *J. Mater. Chem. A* **3** 9152–9

[289] Mirershadi S and Ahmadi-Kandjani S 2015 Efficient thin luminescent solar concentrator based on organometal halide perovskite *Dye. Pigment.* **120** 15–21

[290] Yang J, Siempelkamp B D, Liu D and Kelly T L 2015 Investigation of $CH_3NH_3PbI_3$ Degradation Rates and Mechanisms in Controlled Humidity Environments Using *in Situ* Techniques *ACS Nano* **9** 1955–63

[291] Christians J A, Miranda Herrera P A and Kamat P V. 2015 Transformation of the Excited State and Photovoltaic Efficiency of $CH_3NH_3PbI_3$ Perovskite upon

Controlled Exposure to Humidified Air *J. Am. Chem. Soc.* **137** 1530–8

[292] Qiu W, Merckx T, Jaysankar M, Masse de la Huerta C, Rakocevic L, Zhang W, Paetzold U W, Gehlhaar R, Froyen L, Poortmans J, Cheyns D, Snaith H J and Heremans P 2016 Pinhole-free perovskite films for efficient solar modules *Energy Environ. Sci.* **9** 484–9

[293] Wehrenfennig C, Liu M, Snaith H J, Johnston M B and Herz L M 2014 Charge carrier recombination channels in the low-temperature phase of organic-inorganic lead halide perovskite thin films *APL Mater.* **2** 081513

[294] Galisteo-López J F, Anaya M, Calvo M E and Míguez H 2015 Environmental Effects on the Photophysics of Organic–Inorganic Halide Perovskites *J. Phys. Chem. Lett.* **6** 2200–5

[295] Şahin D, Ilan B and Kelley D F 2011 Monte-Carlo simulations of light propagation in luminescent solar concentrators based on semiconductor nanoparticles *J. Appl. Phys.* **110** 033108

[296] Emery K Solar Spectral Irradiance: Air Mass 1.5

[297] Şahin D and Ilan B 2013 Radiative transport theory for light propagation in luminescent media *J. Opt. Soc. Am. A* **30** 813

[298] Field H and Field H 1997 *Solar Cell Spectral Response Measurement Errors Related to Spectral Band Width and Chopped Light Waveform*

[299] Aldibaja F K, Badia L, Mas-Marzá E, Sánchez R S, Barea E M and Mora-Sero I 2015 Effect of different lead precursors on perovskite solar cell performance and stability *J. Mater. Chem. A* **3** 9194–200

[300] Kim S Y 1996 Simultaneous determination of refractive index, extinction

coefficient, and void distribution of titanium dioxide thin film by optical methods *Appl. Opt.* **35** 6703

[301] Kim J Y, Kim S H, Lee H-H, Lee K, Ma W, Gong X and Heeger A J 2006 New Architecture for High-Efficiency Polymer Photovoltaic Cells Using Solution-Based Titanium Oxide as an Optical Spacer *Adv. Mater.* **18** 572–6

[302] Liu D and Kelly T L 2014 Perovskite solar cells with a planar heterojunction structure prepared using room-temperature solution processing techniques *Nat. Photonics* **8** 133–8

[303] Jeon N J, Noh J H, Yang W S, Kim Y C, Ryu S, Seo J and Seok S Il 2015 Compositional engineering of perovskite materials for high-performance solar cells *Nature* **517** 476–80

[304] Anon Best Research-Cell Efficiency Chart | Photovoltaic Research | NREL

[305] Chen Q, De Marco N, Yang Y (Michael), Song T-B, Chen C-C, Zhao H, Hong Z, Zhou H and Yang Y 2015 Under the spotlight: The organic–inorganic hybrid halide perovskite for optoelectronic applications *Nano Today* **10** 355–96

[306] Stranks S D, Eperon G E, Grancini G, Menelaou C, Alcocer M J P, Leijtens T, Herz L M, Petrozza A and Snaith H J 2013 Electron-hole diffusion lengths exceeding 1 micrometer in an organometal trihalide perovskite absorber. *Science* **342** 341–4

[307] Susrutha B, Giribabu L and Singh S P 2015 Recent advances in flexible perovskite solar cells *Chem. Commun.* **51** 14696–707

[308] Tan Z-K, Moghaddam R S, Lai M L, Docampo P, Higler R, Deschler F, Price M, Sadhanala A, Pazos L M, Credgington D, Hanusch F, Bein T, Snaith H J and Friend R H 2014 Bright light-emitting diodes based on organometal halide perovskite *Nat.*

Nanotechnol. **9** 687–92

[309] Liu M, Johnston M B and Snaith H J 2013 Efficient planar heterojunction perovskite solar cells by vapour deposition *Nature* **501** 395–8

[310] Yin X, Chen P, Que M, Xing Y, Que W, Niu C and Shao J 2016 Highly Efficient Flexible Perovskite Solar Cells Using Solution-Derived NiO_x Hole Contacts *ACS Nano* **10** 3630–6

[311] Li D, Dong G, Li W and Wang L 2015 High performance organic-inorganic perovskite-optocoupler based on low-voltage and fast response perovskite compound photodetector *Sci. Rep.* **5** 7902

[312] Yang G, Tao H, Qin P, Ke W and Fang G 2016 Recent progress in electron transport layers for efficient perovskite solar cells *J. Mater. Chem. A* **4** 3970–90

[313] Qin P, Domanski A L, Chandiran A K, Berger R, Butt H-J, Dar M I, Moehl T, Tetreault N, Gao P, Ahmad S, Nazeeruddin M K and Grätzel M 2014 Yttrium-substituted nanocrystalline TiO_2 photoanodes for perovskite based heterojunction solar cells. *Nanoscale* **6** 1508–14

[314] Zhao Y and Zhu K 2013 Charge Transport and Recombination in Perovskite (CH_3NH_3)PbI_3 Sensitized TiO_2 Solar Cells *J. Phys. Chem. Lett.* **4** 2880–4

[315] Kim S S, Bae S and Jo W H 2015 Performance enhancement of planar heterojunction perovskite solar cells by n-doping of the electron transporting layer *Chem. Commun.* **51** 17413–6

[316] Son D-Y, Im J-H, Kim H-S and Park N-G 2014 11% Efficient Perovskite Solar Cell Based on ZnO Nanorods: An Effective Charge Collection System *J. Phys. Chem. C* **118** 16567–73

[317] Zhou H, Chen Q, Li G, Luo S, Song T -b., Duan H-S, Hong Z, You J, Liu Y and Yang Y 2014 Interface engineering of highly efficient perovskite solar cells *Science (80-.).* **345** 542–6

[318] Mahmood K, Swain B S, Kirmani A R and Amassian A 2015 Highly efficient perovskite solar cells based on a nanostructured WO_3 –TiO_2 core–shell electron transporting material *J. Mater. Chem. A* **3** 9051–7

[319] Docampo P, Ball J M, Darwich M, Eperon G E and Snaith H J 2013 Efficient organometal trihalide perovskite planar-heterojunction solar cells on flexible polymer substrates *Nat. Commun.* **4** 2761

[320] Yang P, Yan H, Mao S, Russo R, Johnson J, Saykally R, Morris N, Pham J, He R and Choi H-J 2002 Controlled Growth of ZnO Nanowires and Their Optical Properties *Adv. Funct. Mater.* **12** 323

[321] Li H, Liang C, Zhong K, Liu M, Hope G A, Tong Y and Liu P 2009 The Modulation of Optical Property and its Correlation with Microstructures of ZnO Nanowires *Nanoscale Res. Lett.* **4** 1183–90

[322] Elilarassi R and Chandrasekaran G 2010 Effect of annealing on structural and optical properties of zinc oxide films *Mater. Chem. Phys.* **121** 378–84

[323] Dhara S and Giri P 2011 Enhanced UV photosensitivity from rapid thermal annealed vertically aligned ZnO nanowires *Nanoscale Res. Lett.* **6** 504

[324] Liu C, Wang K, Du P, Yi C, Meng T and Gong X 2015 Efficient Solution-Processed Bulk Heterojunction Perovskite Hybrid Solar Cells *Adv. Energy Mater.* **5** 1402024

[325] Im J-H, Luo J, Franckevičius M, Pellet N, Gao P, Moehl T, Zakeeruddin S M, Nazeeruddin M K, Grätzel M and Park N-G 2015 Nanowire Perovskite Solar Cell

Nano Lett. **15** 2120–6

[326] Suscavage M, Harris M, Bliss D, Yip P, Wang S-Q, Schwall D, Bouthillette L, Bailey J, Callahan M, Look D C, Reynolds D C, Jones R L and Litton C W 1998 High Quality Hydrothermal ZnO Crystals *MRS Proc.* **537** G3.40

[327] Juárez-Diaz G, Martínez J, García-Cruz M L, Peña-Sierra R, García J A and Pacio M 2010 Hall effect and conductivity in zinc oxide (ZnO) doped by thermal diffusion of indium and copper *Phys. status solidi* **7** 957–9

[328] Mora-Seró I, Fabregat-Santiago F, Denier B, Bisquert J, Tena-Zaera R, Elias J and Lévy-Clément C 2006 Determination of carrier density of ZnO nanowires by electrochemical techniques *Appl. Phys. Lett.* **89** 203117

[329] Yang X, Wolcott A, Wang G, Sobo A, Fitzmorris R C, Qian F, Zhang J Z and Li Y 2009 Nitrogen-Doped ZnO Nanowire Arrays for Photoelectrochemical Water Splitting *Nano Lett.* **9** 2331–6

[330] Eperon G E, Burlakov V M, Docampo P, Goriely A and Snaith H J 2014 Morphological Control for High Performance, Solution-Processed Planar Heterojunction Perovskite Solar Cells *Adv. Funct. Mater.* **24** 151–7

[331] Dualeh A, Moehl T, Tétreault N, Teuscher J, Gao P, Nazeeruddin M K and Grätzel M 2014 Impedance Spectroscopic Analysis of Lead Iodide Perovskite-Sensitized Solid-State Solar Cells *ACS Nano* **8** 362–73

[332] Xie F X, Zhang D, Su H, Ren X, Wong K S, Grätzel M and Choy W C H 2015 Vacuum-Assisted Thermal Annealing of $CH_3NH_3PbI_3$ for Highly Stable and Efficient Perovskite Solar Cells *ACS Nano* **9** 639–46

[333] Voznyy O, Sutherland B R, Ip A H, Zhitomirsky D and Sargent E H 2017

Engineering charge transport by heterostructuring solution-processed semiconductors *Nat. Rev. Mater.* **2** 17026

[334] Zhang W, Saliba M, Stranks S D, Sun Y, Shi X, Wiesner U and Snaith H J 2013 Enhancement of Perovskite-Based Solar Cells Employing Core–Shell Metal Nanoparticles *Nano Lett.* **13** 4505–10

[335] Raja A, Chaves A, Yu J, Arefe G, Hill H M, Rigosi A F, Berkelbach T C, Nagler P, Schüller C, Korn T, Nuckolls C, Hone J, Brus L E, Heinz T F, Reichman D R and Chernikov A 2017 Coulomb engineering of the bandgap and excitons in two-dimensional materials *Nat. Commun.* **8** 15251

[336] Kerr J 1878 XXIV. On reflection of polarized light from the equatorial surface of a magnet. *London, Edinburgh, Dublin Philos. Mag. J. Sci.* **5** 161–77

[337] Scott G and Lacklison D 1976 Magnetooptic properties and applications of bismuth substituted iron garnets *IEEE Trans. Magn.* **12** 292–311

[338] Diwekar M, Kamaev V, Shi J and Vardeny Z V. 2004 Optical and magneto-optical studies of two-dimensional metallodielectric photonic crystals on cobalt films *Appl. Phys. Lett.* **84** 3112–4

[339] Kahl S and Grishin A M 2004 Enhanced Faraday rotation in all-garnet magneto-optical photonic crystal *Appl. Phys. Lett.* **84** 1438–40

[340] Inoue M, Arai K, Fujii T and Abe M 1998 Magneto-optical properties of one-dimensional photonic crystals composed of magnetic and dielectric layers *J. Appl. Phys.* **83** 6768–70

[341] Inoue M, Arai K, Fujii T and Abe M 1999 One-dimensional magnetophotonic crystals *J. Appl. Phys.* **85** 5768–70

[342] Yang H C, Fujita J, Levy M and Steel M J 2001 Flat-Top Response in One-Dimensional Magnetic Photonic Bandgap Structures With Faraday Rotation Enhancement *J. Light. Technol. Vol. 19, Issue 12, pp. 1964-* **19** 1964

[343] Abe M and Suwa T 2004 Surface plasma resonance and magneto-optical enhancement in composites containing multicore-shell structured nanoparticles *Phys. Rev. B* **70** 235103

[344] Cai Z, Leong E S P, Wang Z, Niu W, Zhang W, Ravaine S, Yakovlev N L, Liu Y J, Teng J and Lu X 2015 Sandwich-structured Fe_2O_3@SiO_2@Au nanoparticles with magnetoplasmonic responses *J. Mater. Chem. C* **3** 11645–52

[345] Smolensky E D, Neary M C, Zhou Y, Berquo T S and Pierre V C 2011 Fe_3O_4@organic@Au: core–shell nanocomposites with high saturation magnetisation as magnetoplasmonic MRI contrast agents *Chem. Commun.* **47** 2149–51

[346] Banthí J C, Meneses-Rodríguez D, García F, González M U, García-Martín A, Cebollada A and Armelles G 2012 High Magneto-Optical Activity and Low Optical Losses in Metal-Dielectric Au/Co/Au-SiO2 Magnetoplasmonic Nanodisks *Adv. Mater.* **24** OP36–41

[347] Toal B, McMillen M, Murphy A, Hendren W, Arredondo M and Pollard R 2014 Optical and magneto-optical properties of gold core cobalt shell magnetoplasmonic nanowire arrays *Nanoscale* **6** 12905–11

[348] Appel E, Hoffmann V and Soffel H C 1990 Magneto-optical Kerr effect in (titano)magnetite, pyrrhotite and hematite *Phys. Earth Planet. Inter.* **65** 36–42

[349] Li J, Cushing S K, Zheng P, Meng F, Chu D and Wu N 2013 Plasmon-induced photonic and energy-transfer enhancement of solar water splitting by a hematite

nanorod array *Nat. Commun.* **4** 2651

[350] Onbasli M C, Beran L, Zahradník M, Kučera M, Antoš R, Mistrík J, Dionne G F, Veis M and Ross C A 2016 Optical and magneto-optical behavior of Cerium Yttrium Iron Garnet thin films at wavelengths of 200–1770 nm *Sci. Rep.* **6** 23640

[351] Hansen P and Krumme J-P 1984 Magnetic and magneto-optical properties of garnet films *Thin Solid Films* **114** 69–107

[352] Naik G V., Schroeder J L, Ni X, Kildishev A V., Sands T D and Boltasseva A 2012 Titanium nitride as a plasmonic material for visible and near-infrared wavelengths *Opt. Mater. Express* **2** 478

[353] Ferreiro-Vila E, García-Martín J M, Cebollada A, Armelles G and González M U 2013 Magnetic modulation of surface plasmon modes in magnetoplasmonic metal-insulator-metal cavities *Opt. Express* **21** 4917

[354] Ferreiro-Vila E, González-Díaz J B, Fermento R, González M U, García-Martín A, García-Martín J M, Cebollada A, Armelles G, Meneses-Rodríguez D and Sandoval E M 2009 Intertwined magneto-optical and plasmonic effects in Ag/Co/Ag layered structures *Phys. Rev. B* **80** 125132

[355] Bi L, Hu J, Jiang P, Kim D H, Dionne G F, Kimerling L C and Ross C A 2011 On-chip optical isolation in monolithically integrated non-reciprocal optical resonators *Nat. Photonics* **5** 758–62

[356] Henry Y, Ounadjela K, Piraux L, Dubois S, George J-M and Duvail J-L 2001 Magnetic anisotropy and domain patterns in electrodeposited cobalt nanowires *Eur. Phys. J. B* **20** 35–54

[357] Watanabe K, Takemura Y, Shimazu Y and Shirakashi J 2004 Magnetic

nanostructures fabricated by the atomic force microscopy nano-lithography technique *Nanotechnology* **15** S566–9

[358] Thiaville A, García J M and Miltat J 2002 Domain wall dynamics in nanowires *J. Magn. Magn. Mater.* **242**–**245** 1061–3

[359] Zysler R D, Fiorani D, Testa A M, Godinho M, Agostinelli E and Suber L 2004 Size effects in the spin-flop transition of hematite nanoparticles *J. Magn. Magn. Mater.* **272**–**276** 1575–6

[360] Yang Y, Forster M, Ling Y, Wang G, Zhai T, Tong Y, Cowan A J and Li Y 2016 Acid Treatment Enables Suppression of Electron-Hole Recombination in Hematite for Photoelectrochemical Water Splitting *Angew. Chemie* **128** 3464–8

[361] Li M, Yang Y, Ling Y, Qiu W, Wang F, Liu T, Song Y, Liu X, Fang P, Tong Y and Li Y 2017 Morphology and Doping Engineering of Sn-Doped Hematite Nanowire Photoanodes *Nano Lett.* **17** 2490–5

[362] Pu Y-C, Wang G, Chang K-D, Ling Y, Lin Y-K, Fitzmorris B C, Liu C-M, Lu X, Tong Y, Zhang J Z, Hsu Y-J and Li Y 2013 Au Nanostructure-Decorated TiO_2 Nanowires Exhibiting Photoactivity Across Entire UV-visible Region for Photoelectrochemical Water Splitting *Nano Lett.* **13** 3817–23

[363] Amaral J J, Wan J, Rodarte A L, Ferri C, Quint M T, Pandolfi R J, Scheibner M, Hirst L S and Ghosh S 2015 Magnetic field induced quantum dot brightening in liquid crystal synergized magnetic and semiconducting nanoparticle composite assemblies *Soft Matter* **11** 255–60

[364] Sato K 1981 Measurement of Magneto-Optical Kerr Effect Using Piezo-Birefringent Modulator *Jpn. J. Appl. Phys.* **20** 2403–9